

ISSN: 2687 - 4539

CHAOS

THEORY AND APPLICATIONS

IN APPLIED SCIENCES AND ENGINEERING



VOLUME 3, ISSUE 2, NOVEMBER 2021

AN INTERDISCIPLINARY JOURNAL OF NONLINEAR SCIENCE

CHAOS

THEORY AND APPLICATIONS

IN APPLIED SCIENCES AND ENGINEERING

Chaos Theory and Applications (CHTA)

Volume: 3 – Issue No: 2 (November 2021)

<https://dergipark.org.tr/en/pub/chaos/issue/58077>

Honorary Editorial Board

Otto E. ROSSLER, University of Tuebingen, GERMANY, oeros00@yahoo.com

Julien C. SPOTT, University of Wisconsin–Madison, USA, csprott@wisc.edu

Guanrong CHEN, City University of Hong Kong, HONG KONG, eegchen@cityu.edu.hk

José A. Tenreiro MACHADO, Polytechnic Institute of Porto, PORTUGAL, jtm@isep.ipp.pt

Editor-in-Chief

Akif AKGUL, Hitit University, TURKEY, akifakgul@hitit.edu.tr

Associate Editors

Miguel A. F. SANJUAN, Universidad Rey Juan Carlos, SPAIN, miguel.sanjuan@urjc.es

Chunbiao LI, Nanjing University of Information Science & Technology, CHINA, goontry@126.com

J. M. MUÑOZ PACHECO, Benemérita Universidad Autónoma de Puebla, MEXICO, jesusm.pacheco@correo.buap.mx

Karthiekeyan RAJAGOPAL, Defence University, ETHIOPIA, rkarthiekeyan@gmail.com

Nikolay V. KUZNETSOV, Saint Petersburg State University, RUSSIA, n.v.kuznetsov@spbu.ru

Sifeu T. KINGNI, University of Maroua, CAMEROON, stkingni@gmail.com

Fahrettin HORASAN, Kirikkale University, TURKEY, fhorasan@kku.edu.tr

Editorial Board Members

Jun MA, Lanzhou University of Technology, CHINA, hyperchaos@lut.edu.cn

Herbert Ho-Ching LU, The University of Western Australia, AUSTRALIA, herbert.iu@uwa.edu.au

Alexander PCHELINTSEV, Tambov State Technical University, RUSSIA, pchelintsev.an@yandex.ru

Wesley Joo - Chen THIO, The Ohio State University, USA, wesley.thio@gmail.com

Mustafa Zahid YILDIZ, Sakarya University of Applied Sciences, TURKEY, mustafayildiz@sakarya.edu.tr

Anastasios (Tassos) BOUNTIS, University of Patras, GREECE, anastasios.bountis@nu.edu.kz

Marcelo MESSIAS, São Paulo State University, BRAZIL, marcelo.messias1@unesp.br

Sajad JAFARI, Ton Duc Thang University, VIETNAM, sajadjafari83@gmail.com

Jesús M. SEOANE, Universidad Rey Juan Carlos, SPAIN, jesus.seoane@urjc.es

G. Cigdem YALCIN, Istanbul University, TURKEY, gycalcin@istanbul.edu.tr

Marcelo A. SAVI, Universidade Federal do Rio de Janeiro, BRAZIL, savi@mecanica.coppe.ufrj.br

Christos K. VOLOS, Aristotle University of Thessaloniki, GREECE, volos@physics.auth.gr

Charalampos (Haris) SKOKOS, University of Cape Town, SOUTH AFRICA, haris.skokos@uct.ac.za

Ihsan PEHLIVAN, Sakarya University of Applied Sciences, TURKEY, ipehlivan@sakarya.edu.tr

Olfa BOUBAKER, University of Carthage, TUNUSIA, olfa_insat@yahoo.com
Binoy Krishna ROY, National Institute of Technology Silchar, INDIA, bkr_nits@yahoo.co.in
Jacques KENGNE, Université de Dschang, CAMEROON, kengnemozart@yahoo.fr
Fatih KURUGOLLU, University of Derby, UK, F.Kurugollu@derby.ac.uk
Denis BUTUSOV, Petersburg State Electrotechnical University, RUSSIA, butusovdn@mail.ru
Iqtadar HUSSAIN, Qatar University, QATAR, iqtadarqau@qu.edu.qa
Irene M. MOROZ, University of Oxford, UK, Irene.Moroz@maths.ox.ac.uk
Serdar CICEK, Nevsehir Hacı Bektas Veli University, TURKEY, serdarcicek@gmail.com
Zhouchao WEI, China University of Geosciences, CHINA, weizhouchao@163.com
Qiang LAI, East China Jiaotong University, CHINA, laiqiang87@126.com
Viet-thanh PHAM, Phenikaa University, VIETNAM, pvt3010@gmail.com
Jay Prakash SINGH, Rewa Engineering College, INDIA, jp4ssm@gmail.com
Yılmaz UYAROĞLU, Sakarya University, TURKEY, uyaroglu@sakarya.edu.tr
Shaobo HE, Central South University, CHINA, hshaobo_123@163.com
Esteban Tlelo CUAUTLE, Instituto Nacional de Astrofísica, MEXICO, etlelo@inaoep.mx
Dangheorghie DIMITRIU, Alexandru Ioan Cuza University of Iasi, ROMANIA, dimitriu@uaic.ro
Jawad AHMAD, Edinburgh Napier University, UK, jawad.saj@gmail.com
Engin CAN, Sakarya University of Applied Sciences, TURKEY, ecan@subu.edu.tr
Metin VARAN, Sakarya University of Applied Sciences, TURKEY, mvaran@sakarya.edu.tr
Sadaqat Ur REHMAN, Namal Institute, PAKISTAN, engr.sidkhan@gmail.com
Murat TUNA, Kirklareli University, TURKEY, murat.tuna@klu.edu.tr

Editorial Advisory Board Members

Ayhan ISTANBULLU, Balıkesir University, TURKEY, ayhanistan@yahoo.com
Ismail KOYUNCU, Afyon Kocatepe University, TURKEY, ismailkoyuncu@aku.edu.tr
Fatih OZKAYNAK, Firat University, TURKEY, ozkaynak@firat.edu.tr
Sezgin KACAR, Sakarya University of Applied Sciences, TURKEY, skacar@subu.edu.tr
Ugur Erkin KOCAMAZ, Bursa Uudag University, TURKEY, ugurkocamaz@gmail.com
Erdinc AVAROGLU, Mersin University, TURKEY, eavaroglu@mersin.edu.tr
Ali DURDU, Social Sciences University of Ankara, TURKEY, ali.durdu@asbu.edu.tr
Hakan KOR, Hitit University, TURKEY, hakankor@hitit.edu.tr

Language Editors

Muhammed Maruf OZTURK, Suleyman Demirel University, TURKEY, muhammedozturk@sdu.edu.tr
Mustafa KUTLU, Sakarya University of Applied Sciences, TURKEY, mkutlu@subu.edu.tr

Technical Coordinator

Muhammed Ali PALA, Sakarya University of Applied Sciences, TURKEY, pala@subu.edu.tr
Murat Erhan CIMEN, Sakarya University of Applied Sciences, TURKEY, muratcimen@sakarya.edu.tr
Harun Emre KIRAN, Hitit University, TURKEY, harunemrekiran@hitit.edu.tr

CHAOS

THEORY AND APPLICATIONS


IN APPLIED SCIENCES AND ENGINEERING

Chaos Theory and Applications (CHTA)
 Volume: 3 – Issue No: 2 (November 2021)
<https://dergipark.org.tr/tr/pub/chaos/issue/58077>

Contents

Author(s), Paper Title	Pages
Miguel A. F. SANJUAN. "Unpredictability, Uncertainty and Fractal Structures in Physics" (Editorial)	43-46
Chunbiao LI, Yicheng JIANG, Xu MA. "On Offset Boosting in Chaotic System." (Research Article)	47-54
Tokoue Ngatcha DIANORRÉ, Abba Oum ALHADJI, Alex Stéphane KEMNANG TSAFACK, Sifeu T. KINGNI. "Dynamical Analysis and Microcontroller Implementation of Linear Resistor-Capacitor Shunted Josephson Junction Model." (Research Article)	55-58
Nimet KORKMAZ, Ibrahim Ethem SACU. "An Efficient Design Procedure to Implement the Fractional-Order Chaotic Jerk Systems with the Programmable Analog Platform." (Research Article)	59-66
Hakan OZTURK. "An Analysis of Power System Stability against Hyperchaotic Noises and Blackouts." (Research Article)	67-76
Ahoudou NDOUKOUO, Jules METSEBO, J.M NJANKOUO. "Vibrational Analysis of a Metallic Column Submitted to Mechanical Axial Load and Fire Exposure." (Research Article)	77-86
Zeki CALISKAN. "Discussions on Special and General Relativity Model." (Research Article)	87-94

Unpredictability, Uncertainty and Fractal Structures in Physics

Miguel A. F. Sanjuán ^{*,1}

*Department of Physics Universidad Rey Juan Carlos 28933 Móstoles, Madrid, Spain.

ABSTRACT In Physics, we have laws that determine the time evolution of a given physical system, depending on its parameters and its initial conditions. When we have multi-stable systems, many attractors coexist so that their basins of attraction might possess fractal or even Wada boundaries in such a way that the prediction becomes more complicated depending on the initial conditions. Chaotic systems typically present fractal basins in phase space. A small uncertainty in the initial conditions gives rise to a certain unpredictability of the final state behavior. The new notion of basin entropy provides a new quantitative way to measure the unpredictability of the final states in basins of attraction. Simple methods from chaos theory can contribute to a better understanding of fundamental questions in physics as well as other scientific disciplines.

KEYWORDS

Chaos
Chaotic systems
Fractal structures
Unpredictability
Uncertainty

The idea of uncertainty has pervaded physics. Among the sources of uncertainty in dynamical systems, we can mention the notion of sensitivity to initial conditions, and the existence of fractal structures in phase space as another one, for a mere simplification.

In this regard, it is interesting to bring up a famous rhyme traditionally associated with Benjamin Franklin (1706-1790), although antecedents of the same idea date back to the 15th century, which is known as For Want of a Nail offering an intuitive and poetic image of the idea of sensitive dependence on initial conditions, which is one of the hallmarks of chaos:

*For want of a nail the shoe was lost,
for want of a shoe the horse was lost,
for want of a horse the knight was lost,
for want of a knight the battle was lost,
for want of a battle the kingdom was lost.
So a kingdom was lost—all for want of a nail.*

Due to the enormous consequences on determinism in physics that quantum mechanics has brought about through

Heisenberg uncertainty principle, the idea of indeterminism has been directly related to quantum mechanics. This has led somehow to consider classical mechanics as completely deterministic and predictable, which is not entirely true [Bera et al. \(2017\)](#).

It is fascinating to corroborate that the idea of sensitive dependence on initial conditions was considered in detail by the German physicist Max Born (1882-1970), Nobel Prize in Physics in 1954, in an article entitled Is Classical Mechanics in fact deterministic? [Born \(1969\)](#). In it he presented a study of a two-dimensional Lorentz gas initially proposed by the Dutch physicist Hendrik A. Lorentz (1853-1928) in 1905 as a model for the study of electrical conductivity in metals. In this model, a particle moves in a plane that is full of hard spheres and collides with them so that a small change in the initial conditions will significantly alter the trajectory of the particle. This fact led Born to conclude that determinism traditionally related to classical mechanics is not real, since it is not possible to know with infinite precision the initial conditions of a physical experiment.

Furthermore, in the lecture [Ballentine \(1970\)](#) that he gave in 1954 when he received the Nobel Prize we can read the following words:

Manuscript received: 12 December 2020,

Accepted: 27 December 2020.

¹ miguel.sanjuan@urjc.es (Corresponding author)

“Newtonian mechanics is deterministic in the following sense: If the initial state (positions and velocities of all particles) of a system is accurately given, then the state at any other time (earlier or later) can be calculated from the laws of mechanics. All the other branches of classical physics have been built up according to this model. Mechanical determinism gradually became a kind of article of faith: the world as a machine, an automaton. As far as I can see, this idea has no forerunners in ancient and medieval philosophy. The idea is a product of the immense success of Newtonian mechanics, particularly in astronomy. In the 19th century it became a basic philosophical principle for the whole of exact science. I asked myself whether this was really justified. Can absolute predictions really be made for all time on the basis of the classical equations of motion? It can easily be seen, by simple examples, that this is only the case when the possibility of absolutely exact measurement (of position, velocity, or other quantities) is assumed. Let us think of a particle moving without friction on a straight line between two end-points (walls), at which it experiences completely elastic recoil. It moves with constant speed equal to its initial speed v_0 backwards and forwards, and it can be stated exactly where it will be at a given time provided that v_0 is accurately known. But if a small inaccuracy Δv_0 is allowed, then the inaccuracy of prediction of the position at time t is $t\Delta v_0$ which increases with t . If one waits long enough until time $t_c = l/\Delta v_0$ where l is the distance between the elastic walls, the inaccuracy Δx will have become equal to the whole space l . Thus, it is impossible to forecast anything about the position at a time which is later than t_c . Thus, determinism lapses completely into indeterminism as soon as the slightest inaccuracy in the data on velocity is permitted.”

Likewise, the American physicist Richard Feynman (1918-1988), who won the Nobel Prize for Physics in 1965, makes similar reflections in his well-known book *Lectures in Physics* [Feynman et al. \(1963\)](#), where he explains that indeterminism is a basic property of many physical systems, and consequently it does not belong exclusively to quantum mechanics.

In the section 38-6 of the first volume of his *Lectures in Physics*, entitled "Philosophical Implications", a masterful description of indeterminism in classical mechanics is made. The fundamental idea is the uncertainty in accurately setting initial conditions to predict the final state of a physical system. Finally affirming: "Because in classical mechanics there was already indeterminism from a practical point of view".

Precisely another important source of uncertainty in dynamical systems is provided by the fractal structures present in phase space. The natural analogy comes from hydrology, thinking on the basin of a river. A drop of water falling to a river basin goes to the river. We can see geographical maps of river basins dividing a territory of any country in a geographic atlas.

In Nonlinear Dynamics a basin of attraction is defined as the set of initial conditions whose trajectories go to a specific attractor. Furthermore, when we have several attractors in a given region of phase space, we have several basins that are separated by the corresponding boundaries. These bound-

aries can be classified as smooth basins and fractal basins, depending on the geometrical nature of the boundaries.

In general, we can affirm that when the boundaries are fractal, so that we can also say that the basins are fractal, the fractality implies unpredictability and uncertainty in the future events of trajectories corresponding to the dynamical system associated to these basins.

An interesting fundamental problem arises when we try to compare a couple of basins, either basins of attraction for dissipative dynamical systems or exit basins for open Hamiltonian systems, since they do not have attractors and as a consequence they cannot have basins of attraction. The fundamental question is to ascertain which basin is more unpredictable. This is the question we may raise by observing the exit basins plotted in Fig.1.

Traditionally the unpredictability associated to fractal boundaries has been measured by using the uncertainty dimension. However, there are many examples where we can see that the uncertainty dimension does not help to accurately discriminate among fractal basins with a different degree of unpredictability.

Further for another type of more complicated basins such as riddled basins, where we can say that a basin A is riddled by B, if for every point of A is possible to find arbitrarily close points of B, the uncertainty dimension $a \approx 0$. What basically implies randomness of a deterministic system, and actually two different riddled basins with different structure might not be able to be discerned its degree of unpredictability by using the uncertainty dimension.

Another type of basins are the Wada basins [Kennedy and Yorke \(1991\)](#), which are fractal basins possessing the Wada property. This property implies that there is a single boundary separating three or more basins, and as a consequence the degree of unpredictability is stronger. For a long period of time there was only one method available to ascertain when a given basin had the Wada property due to Nusse and Yorke [Nusse and Yorke \(1996\)](#). In the past few years, we have developed new methods for testing Wada basins: The Grid Method, the Merging Method and the Saddlestraddle method [Wagemakers et al. \(2020\)](#); [Daza et al. \(2018c, 2015\)](#). A general overview of how to detect Wada basins is offered in [Wagemakers et al. \(2021\)](#).

However, until the appearance of the novel concept of basin entropy [Daza et al. \(2016\)](#) there was not a quantitative way to identify when a given basin, either Wada or not, was more unpredictable than another one. This is precisely what the basin entropy offers, a quantitative tool to measure the unpredictability of basins. Typically, the algorithm to compute the basin entropy depends on three key ingredients that are related to the size of the boundary, the uncertainty dimension of the basin boundaries and the total number of attractors in the specific region in phase space.

Since the appearance of the concept, it has been applied to numerous problems in physics [Daza et al. \(2018b\)](#), such as chaotic scattering associated to experiments of cold-atoms [Daza et al. \(2017a\)](#), chaotic dynamics in relativistic chaotic scattering [Bernal et al. \(2020, 2018\)](#), dynamical systems with

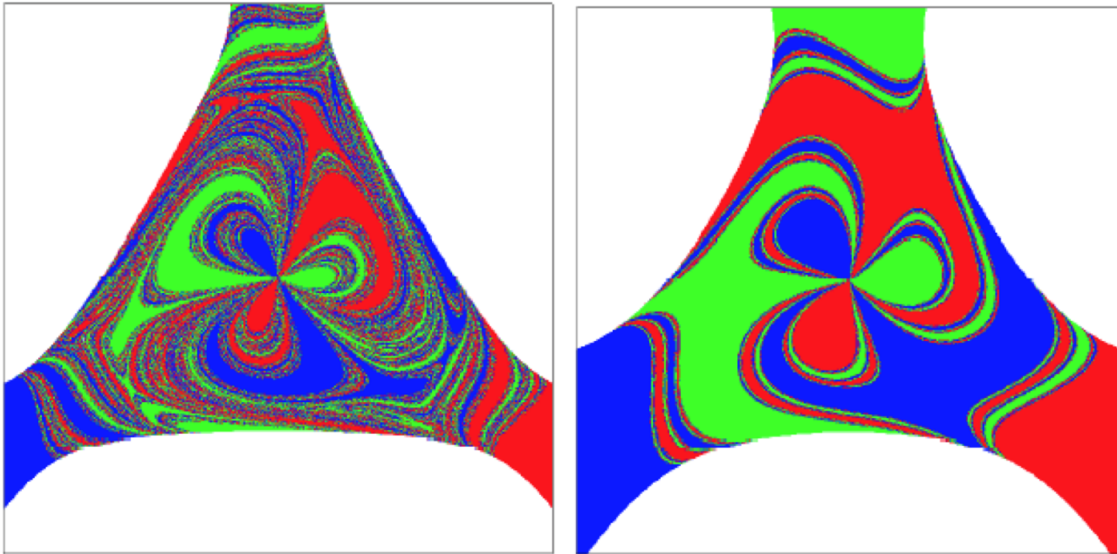


Figure 1 These figures represent the exit basins corresponding to the Hénon-Heiles Hamiltonian for values of the conserved energy above the critical energy in the physical space, so that the Hamiltonian becomes an open system and three different asymptotic states are possible for orbits whose initial conditions are located in the central region.

delay [Daza et al. \(2017b\)](#), in astrophysics to measure the transition between nonhyperbolic and hyperbolic regimes in open Hamiltonian systems [Nieto et al. \(2020\)](#), and indirectly through research on Wada structures associated to the dynamics of photons in binary black hole shadows [Daza et al. \(2018a\)](#) constituting a problem of chaos in general relativity, to cite just a few of them.

The basin entropy quantifies the final state unpredictability of dynamical systems by analyzing the fractal nature of their basins. As such, it constitutes a new tool for the exploration of the uncertainty and unpredictability in nonlinear dynamics. We have applied these methods to different domains in Physics, such as cold atoms, shadows of binary black holes, and classical and relativistic chaotic scattering in astrophysics. We believe that the concept of basin entropy will become an important tool in complex systems studies with applications in multiple scientific fields especially those with multi-stability and other scientific areas as well. Methods derived from nonlinear dynamics have had so far, an enormous influence in many disciplines in science and engineering, though it is important to highlight that tools from the field of chaos theory can be used to understand the rich dynamics of many fundamental problems in physics that are worth to keep exploring through fruitful scientific interactions.

LITERATURE CITED

- Ballentine, L. E., 1970 The statistical interpretation of quantum mechanics. *Reviews of Modern Physics* **42**: 358.
- Bera, M. N., A. Acín, M. Kuś, M. W. Mitchell, and M. Lewenstein, 2017 Randomness in quantum mechanics: philosophy, physics and technology. *Reports on Progress in Physics* **80**: 124001.
- Bernal, J. D., J. M. Seoane, and M. A. F. Sanjuán, 2018 Uncertainty dimension and basin entropy in relativistic chaotic scattering. *Physical Review E* **97**: 042214.
- Bernal, J. D., J. M. Seoane, J. C. Vallejo, L. Huang, and M. A. F. Sanjuán, 2020 Influence of the gravitational radius on asymptotic behavior of the relativistic sitnikov problem. *Physical Review E* **102**: 042204.
- Born, M., 1969 Is classical mechanics in fact deterministic? In *Physics in my Generation*, pp. 78–83, Springer.
- Daza, A., B. Georgeot, D. Guéry-Odelin, A. Wagemakers, and M. A. F. Sanjuán, 2017a Chaotic dynamics and fractal structures in experiments with cold atoms. *Physical Review A* **95**: 013629.
- Daza, A., J. O. Shipley, S. R. Dolan, and M. A. F. Sanjuán, 2018a Wada structures in a binary black hole system. *Physical Review D* **98**: 084050.
- Daza, A., A. Wagemakers, B. Georgeot, D. Guéry-Odelin, and M. A. F. Sanjuán, 2016 Basin entropy: a new tool to analyze uncertainty in dynamical systems. *Scientific Reports* **6**: 1–10.
- Daza, A., A. Wagemakers, B. Georgeot, D. Guéry-Odelin, and M. A. F. Sanjuán, 2018b Basin entropy, a measure of final state unpredictability and its application to the chaotic scattering of cold atoms. In *Chaotic, Fractional, and Complex Dynamics: New Insights and Perspectives*, pp. 9–34, Springer.

- Daza, A., A. Wagemakers, and M. A. F. Sanjuán, 2017b Wada property in systems with delay. *Communications in Nonlinear Science and Numerical Simulation* **43**: 220–226.
- Daza, A., A. Wagemakers, and M. A. F. Sanjuán, 2018c Ascertaining when a basin is Wada: the merging method. *Scientific Reports* **8**: 1–8.
- Daza, A., A. Wagemakers, M. A. F. Sanjuán, and J. A. Yorke, 2015 Testing for basins of Wada. *Scientific Reports* **5**: 1–7.
- Feynman, R. P., R. B. Leighton, and M. L. Sands, 1963 *The Feynman Lectures on Physics. Vol. I Mainly Mechanics, Radiation and Heat*, volume 1. Addison-Wesley, Reading, Massachusetts.
- Kennedy, J. and J. A. Yorke, 1991 Basins of Wada. *Physica D: Nonlinear Phenomena* **51**: 213–225.
- Nieto, A. R., E. E. Zotos, J. M. Seoane, and M. A. F. Sanjuán, 2020 Measuring the transition between nonhyperbolic and hyperbolic regimes in open hamiltonian systems. *Nonlinear Dynamics* **99**: 3029–3039.
- Nusse, H. E. and J. A. Yorke, 1996 Wada basin boundaries and basin cells. *Physica D: Nonlinear Phenomena* **90**: 242–261.
- Wagemakers, A., A. Daza, and M. A. F. Sanjuan, 2021 How to detect Wada basins. *Discrete and Continuous Dynamical Systems B* **26(1)**: 717–739.
- Wagemakers, A., A. Daza, and M. A. F. Sanjuán, 2020 The saddle-straddle method to test for Wada basins. *Communications in Nonlinear Science and Numerical Simulation* **84**: 105167.

How to cite this article: Sanjuán, M. A. F. *Unpredictability, Uncertainty and Fractal Structures in Physics*. *Chaos Theory and Applications*, 3(2), 43-46, 2021.

On Offset Boosting in Chaotic System

Chunbiao Li ¹, Yicheng Jiang ² and Xu Ma ³

^{*}School of Artificial Intelligence, Nanjing University of Information Science and Technology, Nanjing 210044, China, [†]Jiangsu Collaborative Innovation Center of Atmospheric Environment and Equipment Technology (CICAET), Nanjing University of Information Science and Technology, Nanjing 210044, China.

ABSTRACT Offset boosting is an important issue for chaos control due to its broadband property and polarity control. There are two main approaches to realize offset boosting. One is resort to parameter introducing where an offset booster realizes attractor boosting. The other one is by the means of periodic function or absolute value function where any self-reproduced or doubled attractors with diverse offset are extracted out by a specific initial condition. The former also provides a unique window for observing multistability and the latter gives the direction for constructing desired multistability.

KEYWORDS

Offset boosting
Chaos control
Multistability

INTRODUCTION

Chaotic signal is wide used in chaos-based information engineering including chaotic secure communication, image encryption and neural signal processing. Any chaotic signal has its inherent features namely identified as scale (C. Sprott and Xiong 2015; C. Sprott 2010; Gu *et al.* 2021; Lu *et al.* 2019; Liu *et al.* 2020; Wang *et al.* 2020; Zhao *et al.* 2020; Akgul *et al.* 2016, 2019; Falco *et al.* 2012) and offset (Li *et al.* 2019, 2017a; Liu *et al.* 2020; Li and Sprott 2017; Li *et al.* 2021, 2017b; Kingni *et al.* 2020; Ma *et al.* 2021; Zhang *et al.* 2018; Mezatio *et al.* 2019; Bao *et al.* 2020; Chen *et al.* 2020; Zhang *et al.* 2020; Wu *et al.* 2019a; Ding *et al.* 2020). For rescaling a chaotic signal, people usually design dynamical systems with amplitude control from the very beginning. In fact, for an attractor in phase space, amplitude control typically gets involved with offset boosting. Offset boosting means that the attractor is moved in phase space in any direction, which indicates that the average value of corresponding variable is rescaled accordingly. In a differential equation, a simple substitution of $x_i \rightarrow x_i + c$ revises the average value of x_i without revising the left hand of its master system. Therefore it looks very simple in the mathematic view. However, offset boosting is such an important issue in chaotic system since that it gives a direct way for an engineer to transform a bipolar chaotic signal to a unipolar one. And besides this, it seems that offset boosting shows more varieties than our imagination such as attractor boosting, attractor self-reproducing (Li *et al.* 2017a), attractor doubling (Li *et al.* 2019), conditional symmetry (Li *et al.* 2020c),

time-reversible symmetry (Li and Sprott 2017) or even repeller construction (Li *et al.* 2021). For this reason, offset boosting has attracted great interests recently both in continuous system and in discrete maps. Researchers pays great effort to learn how to get those attractors controlled by parameters (Li *et al.* 2017b; Kingni *et al.* 2020; Ma *et al.* 2021; Zhang *et al.* 2018; Mezatio *et al.* 2019) or by initial conditions (Bao *et al.* 2020; Chen *et al.* 2020; Zhang *et al.* 2020; Wu *et al.* 2019a; Ding *et al.* 2020). Even in those memristive systems (Chen *et al.* 2019; Kengne *et al.* 2018; Lu *et al.* 2020; Wu *et al.* 2019b; Yuan *et al.* 2019) offset boosting is still a hot spot for discussion.

As shown in Fig. 1, offset booster can be attached in a chaotic system for attractor boosting, which means that the newly derived attractor stays at different positions controlled by the offset constant. Typically, to realize offset boosting a unified constant is necessary to insert into multiple terms if the corresponding variable appears many times. Specific variable-boostable chaotic systems (Li and Sprott 2016) give the simple possibility for offset boosting since in the right hand there is a variable appearing only once. However, for attractor self-reproducing, periodic functions including multiple similar linear segments are needed where any specific initial condition can visit its most closed attractor obeying the distribution of basin of attraction. In this work, parameter-oriented offset boosting and initial-condition-oriented are systematically discussed based on system VB14 (Li and Sprott 2016), as indicated in Table.1. The case of absolute value function introducing is not listed in the table for easy discussion in the following text where more parameters are embedded and correspondingly the original system is changed more dramatically. In section 2, we discuss how to insert a constant to realize offset boosting in some dimensions of a system. In section 3, periodic functions specifically trigonometric functions are addressed for initial condition-triggered offset boosting. In section 4, absolute value functions are introduced for

Manuscript received: 1 July 2021,

Revised: 28 July 2021,

Accepted: 2 August 2021.

¹ chunbiaolee@nuist.edu.cn, goontry@126.com (Corresponding Author)

² ycjnuist@163.com

³ xumanuist@163.com

■ **Table 1 Two regimes of offset boosting**

Cases	Constant or function introducing for offset boosting	Research focus
A	$F(x)=x + d, G(y)=y$	Attractor Boosting
B	$F(x)=x, G(y)=y + h$	
C	$F(x)=3\sin(x), G(y)=y$	Attractor Self-reproducing and Attractor Growing
D	$F(x)=1.8\sin(1.3x), G(y)=y$	
E	$F(x)=x, G(y)=2\cos(y)$	
F	$F(x)=3\tan(0.5x), G(y)=\sin(y)$	
G	$F(x)=x + d, G(y)=\sin(y)$	

attractor doubling. In section 6, absolute value function is applied for polarity reverse for the observation of conditional symmetry and repeller construction. Conclusions are wrapped in the last section.

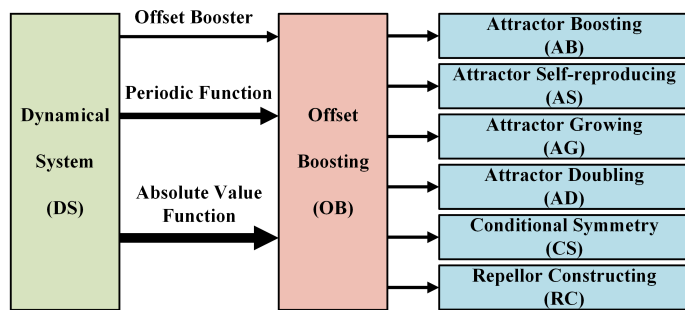


Figure 1 Offset boosting in a dynamical system.

OFFSET BOOSTING BY INTRODUCING CONSTANT TERMS

As mentioned above, to realize offset boosting in a dynamical system, a direct method of introducing a constant in any of the dimension can be applied for this target. For example, we introduce a constant in the variable x in VB14, correspondingly system (1) turns to be system (2) where only an extra single constant appear in the right hand,

$$\begin{cases} \dot{x} = 1 - ayz \\ \dot{y} = z^2 - z \\ \dot{z} = x - bz \end{cases} \quad (1)$$

$$\begin{cases} \dot{x} = 1 - ayz \\ \dot{y} = z^2 - z \\ \dot{z} = x + d - bz \end{cases} \quad (2)$$

Correspondingly, the original attractor, shown in Fig. 2, will be shifted in the x dimension, shown in Fig. 3, without shaking the Lyapunov exponents but spitting out the chaotic signal x in a smoothly revised average, shown in Fig. 4.

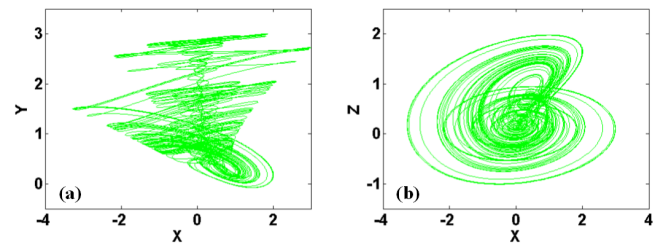


Figure 2 Chaotic attractor of system (1) with $a = 3.55, b = 0.5$ under initial condition $(1, 0, 1)$: (a) x - y , (b) x - z .

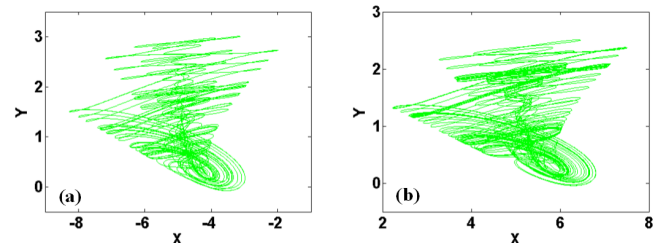


Figure 3 Shifted chaotic attractors in system (2) with $a = 3.55, b = 0.5$ under initial condition $(1 - d, 0, 1)$ (Case A in Table 1): (a) $d = 5$, (b) $d = -5$.

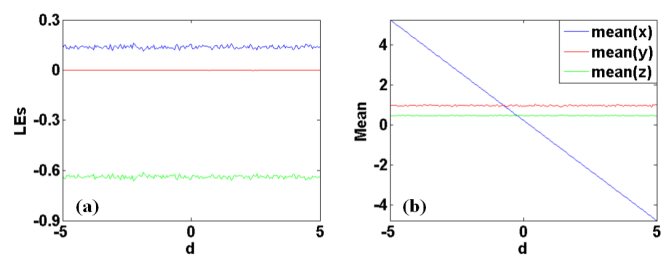


Figure 4 Offset boosting of x in system (2) with $a = 3.55, b = 0.5$ under initial condition $(1 - d, 0, 1)$: (a) Lyapunov exponents, (b) average values.

The operation for offset boosting can be repeated in other dimensions. But this does not mean that all this kind of operations share the same complexity for a dynamical system and correspondingly does not benefit circuit realization equally. For example, it is shown that even an exactly similar operation of $y \rightarrow y + h$ needs much more effort for circuit realization as indicated in system (3). For system (2), a newly introduced direct current source revise the average value of x , while for system (3) (Case B in Table. 1), a new feedback of $-ahz$ should be attached in the x dimension. The offset of y is based on the adjustable resistance in the branch of x -dimension, which is not getting worse. In fact, the constant h still returns the average-value-revised y with unified Lyapunov exponents, as shown in Fig. 5. In some circumstances, it will be much more catastrophic even a single constant is needed for a variable but multiple existence of this variable brings much more complexity.

$$\begin{cases} \dot{x} = 1 - a(y + h)z \\ \dot{y} = z^2 - z \\ \dot{z} = x - bz \end{cases} \quad (3)$$

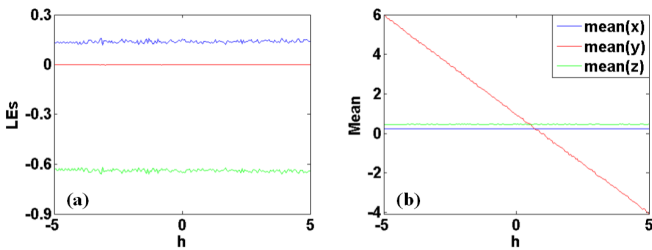


Figure 5 Offset boosting of y in system (3) with $a = 3.55$, $b = 0.5$ under initial condition $(1, -h, 1)$ (Case B in Table 1): (a) Lyapunov exponents, (b) average values.

OFFSET BOOSTING BY INTRODUCING PERIODIC FUNCTIONS

Offset boosting can be realized in a hidden mode where a periodic function is applied for attractor boosting. In this direction, as pointed in (Li et al. 2017a), periodic trigonometric function is introduced for hidden offset boosting by initial condition. In this example, a sinusoidal is equipped as,

$$\begin{cases} \dot{x} = 1 - aG(y)z \\ \dot{y} = z^2 - z \\ \dot{z} = F(x) - bz \end{cases} \quad (4)$$

where $G(y) = y$, $F(x) = 3\sin(x)$. Thus, system (4) (Case C in Table 1) is a self-reproducing system giving infinitely many coexisting attractors, which can be extracted by various initial conditions, as shown in Fig. 6, eight coexisting attractors are given, each of which is of the same shape with same Lyapunov exponents $(0.23401, 0, -0.73402)$ as shown in Fig. 7. The stout structure of attractor in Fig.6 is flattened for the increasing scale in the x -axis. In fact, system (4) reproduces infinitely many attractors standing on different positions in the x -axis but with unified Lyapunov exponents, as shown in Fig. 8. Note that the step-growing average value shows the offset boosting triggered by initial conditions. Each step represents a corresponding attractor and the whole sinusoidal-like evolution reveals the trigonometric nonlinearity.

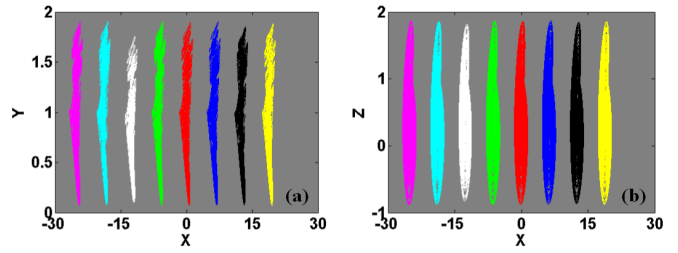


Figure 6 Coexisting attractors in system (4) with $G(y) = y$, $F(x) = 3\sin(x)$, $a = 3.55$, $b = 0.5$ (Case C in Table. 1): (a) x - y , (b) x - z . Each attractor is under different initial conditions (IC). Here cyan is for IC = $(-5, 0, 1)$, pink is for IC = $(-4, 0, 1)$, yellow is for IC = $(-3, 0, 1)$, red is for $(-2, 0, 1)$, green for IC = $(1, 0, 1)$, blue is for IC = $(5, 0, 1)$, white is for IC = $(8, 0, 1)$, black is for $(11, 0, 1)$.

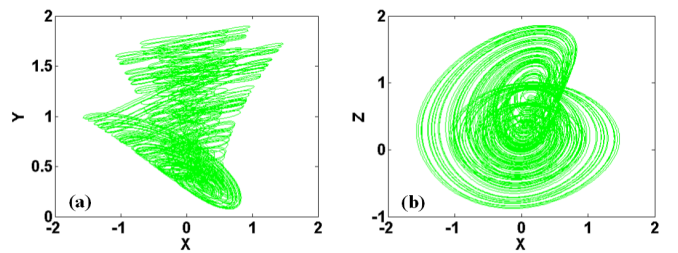


Figure 7 Chaotic attractor of system (4) with $G(y) = y$, $F(x) = 3\sin(x)$, $a = 3.55$, $b = 0.5$ in principal interval when initial condition IC = $(-2, 0, 1)$: (a) x - y , (b) x - z .

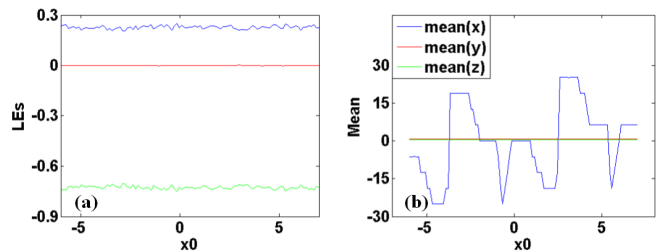


Figure 8 Offset boosting of system (4) with $G(y) = y$, $F(x) = 3\sin(x)$, $a = 3.55$, $b = 0.5$, and IC = $(x_0, 0, 1)$, x_0 varies in $[-6, 7]$: (a) Lyapunov exponents, (b) average values.

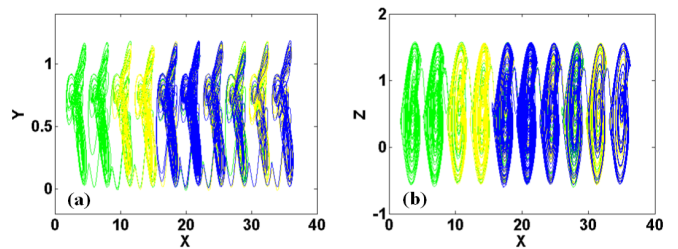


Figure 9 Attractor growing in system (4) with $G(y) = y$, $F(x) = 1.2\sin(1.8x)$, $a = 3.6$, $b = 0.5$ and time duration $T = 1000$. Here green is for IC = $(1, 0, 1)$, yellow is for IC = $(5, 0, 1)$, blue is for IC = $(10, 0, 1)$: (a) x - y , (b) x - z .

Meanwhile revising the feedback of sinusoidal function, attractor growing appears as predicted. In this case the introduced functions in system (4) are: $G(y) = y$, $F(x) = 1.2\sin(1.8x)$ (Case D in Table. 1). Different initial values select the start point for attractor growing indicated in green, yellow and blue in Fig. 9. This is the typical phenomenon of homogenous multistability. Unified Lyapunov exponents are proved along with randomly increasing of the average value of x as shown in Fig.10.

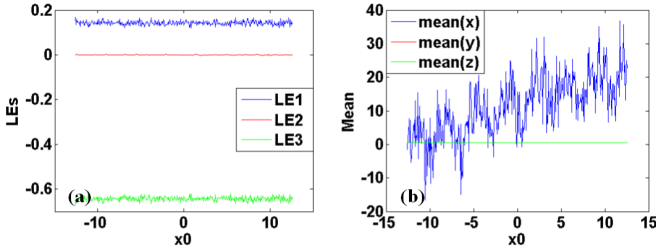


Figure 10 Feature of the growing attractor in system (4) with $G(y) = y$, $F(x) = 1.2\sin(1.8x)$, $a = 3.6$, $b = 0.5$ and time duration of $T = 1000$ under the initial condition $[x_0, 0, 1]$, where x_0 varies in $[-4\pi, 4\pi]$: (a) Lyapunov exponents, (b) average variables.

The initial-condition-oriented offset boosting can extend to other dimension with the same approach. Here a cosine function is introduced in the y dimension in system (4) by $G(y) = 2\cos(y)$, $F(x) = x$ (Case E in Table. 1),

$$\begin{cases} \dot{x} = 1 - 2a \cos(y)z \\ \dot{y} = z^2 - z \\ \dot{z} = x - bz \end{cases} \quad (5)$$

As shown in Fig. 11, when $a = 2.2$, $b = 0.7$ and initial condition $IC = (1, 0, 1)$, system (5) exhibits a chaotic attractor with Lyapunov exponents $(0.13415, 0, -0.83416)$. For the same reason of periodicity, system (5) is a self-reproducing system giving infinitely many coexisting attractors with different average values in the y -dimension, as shown in Fig. 12. Almost unchanged Lyapunov exponents can be seen in Fig. 13, where linearly modulated offset in the y -dimension shows up. There is no conflict in Fig. 8 and Fig. 13. In Fig. 8, the initial condition of x_0 varies in a continuous way in region of $[-6, 7]$, the sinusoidal-like evolution reveals the trigonometric nonlinearity combined with the fractal structure of basin of attraction. Meanwhile in Fig. 13, the initial condition of y_0 varies in a discrete way in the period of cosine function $2n\pi$, the linearly rescaled offset also betrays that the basins for each attractor stand apart from each other in general.

All the operations can be mixed together for flexible offset boosting in any dimension. And furthermore, the attractor self-reproducing can be achieved by other periodic functions. For example, periodic functions are introduced into system (4) in both x and y dimension. Here $G(y)$ and $F(x)$ are selected from other trigonometric functions. When $a = 3.57$, $b = 0.7$, $F(x) = 3 \tan(0.5x)$, $G(y) = \sin(y)$ (Case F in Table. 1), infinitely many attractors scatter in the x -dimension and y -dimension with corresponding attractor space under unified Lyapunov exponents $(0.22152, 0, -0.93029)$. In x -dimension, the attractor distance is defined by the period of tangent function while in y -dimension the attractor distance is defined by the period of sinusoidal function. The attractor distances in x -dimension and y -dimension are equal this time, which

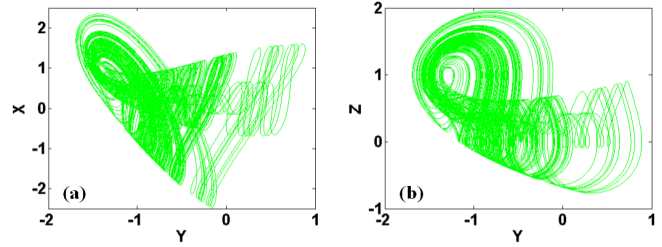


Figure 11 Chaotic attractor of system (5) (case E in Table. 1) with $a = 2.2$, $b = 0.7$ under initial condition $(1, 0, 1)$: (a) y - x , (b) y - z .

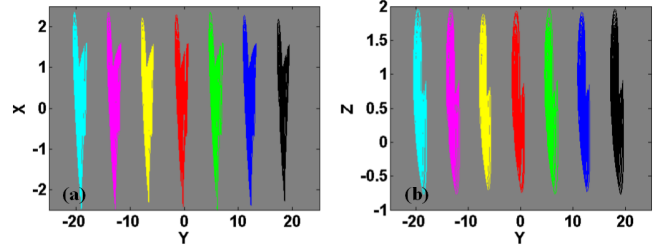


Figure 12 Coexisting attractors in system (5) with $a = 2.2$, $b = 0.7$, and $IC = (1, y_0, 1)$: (a) y - x , (b) y - z . Here cyan is for $y_0 = -6\pi$, pink is for $y_0 = -4\pi$, yellow is for $y_0 = -2\pi$, red is for $y_0 = 0$, green is for $y_0 = 2\pi$, blue is for $y_0 = 4\pi$, black is for $y_0 = 6\pi$.

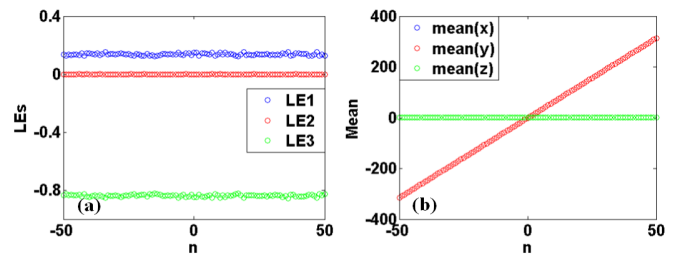


Figure 13 Offset boosting of system (5) with $a = 2.2$, $b = 0.7$, and $IC = (1, y_0, 1)$, $y_0 = 2n\pi$: (a) Lyapunov exponents, (b) average values.

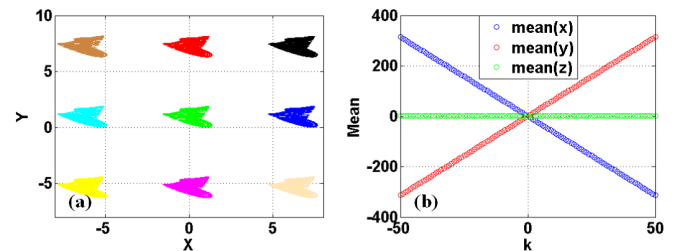


Figure 14 Lattice of strange attractors in system (4) with $a = 3.57$, $b = 0.7$, $F(x) = 3 \tan(0.5x)$, $G(y) = \sin(y)$ (Case F in Table. 1): (a) Coexisting strange attractors when initial conditions are $(1 + 2k\pi, 0 + 2l\pi, 1)$ ($-1 \leq k, l \in \mathbb{Z} \leq 1$), (b) regulated offset when initial conditions are $(1 - 2k\pi, 0 + 2k\pi, 1)$ ($-50 \leq k \in \mathbb{Z} \leq 50$).

is because both functions of $\tan(0.5x)$ and $\sin(y)$ have same period of 2π , as shown in Fig. 14.

Combined regime of offset boosting can be realized in the following system,

$$\begin{cases} \dot{x} = 1 - aG(y)z \\ \dot{y} = z^2 - z \\ \dot{z} = x + d - bz \end{cases} \quad (6)$$

where the offset boosting in the x dimension is controlled by the constant d , while the offset boosting in the y dimension is oriented by the initial condition of y (Case G in Table. 1). When $a = 4.5$, $b = 0.7$, $F(x) = x + d$, $G(y) = \sin(y)$, infinitely many attractors scatter in the y -dimension. Meanwhile the location in x -axis is set by the constant d , as shown in Fig. 15. All these coexisting attractors and constant-controlled attractors share a unified set of Lyapunov exponents $(0.12917, 0, -0.82917)$.

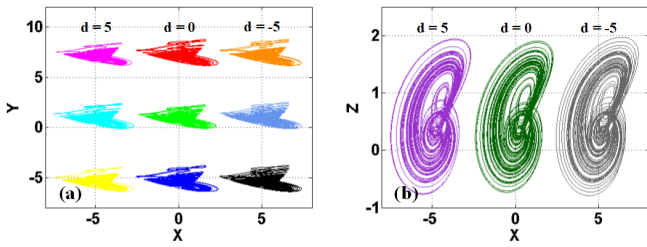


Figure 15 Infinitely many attractors shifted by d in system (6) with $a = 4.5, b = 0.7, G(y) = \sin(y)$ (Case G in Table. 1): (a) x - y , (b) x - z .

ATTRACTOR DOUBLING BY INTRODUCING ABSOLUTE VALUE FUNCTIONS

Offset boosting from a substitution of absolute value function can bring doubled coexisting attractors (Li et al. 2019). For example, take $y \rightarrow |y| - c$ like,

$$\begin{cases} \dot{x} = 1 - a(|y| - c)z \\ \dot{y} = \text{sgn}(y)(z^2 - z) \\ \dot{z} = x + d - bz \end{cases} \quad (7)$$

The original attractor obtained its reproducing in the dimension of y , pseudo-double-scroll attractor with Lyapunov exponents $(0.1477, 0, -0.64335)$ is as shown in Fig. 16. Combined regime of offset boosting can be realized when the offset booster d is not zero. As shown in Fig. 17, the pseudo-double-scroll attractor is controlled locating at various positions in the dimension of x according to the offset booster d . Furthermore, the distance between any two doubled coexisting attractors can be controlled by selecting a propitiate value of c in the absolute value function. As plotted in Fig. 18, when $c = 1$, doubled coexisting attractors stand separately at both sides in the dimension of y . If we hide the obvious independent constant d as the period in the x -dimension trigonometric function as,

$$\begin{cases} \dot{x} = 1 - a(|y| - c)z \\ \dot{y} = \text{sgn}(y)(z^2 - z) \\ \dot{z} = 3 \sin(x) - bz \end{cases} \quad (8)$$

Infinitely many attractors in the dimension of x will also get doubled according to the dimension of y , as shown in Fig. 19. As proved, any of those reproduced coexisting attractors share the unified set of Lyapunov exponents $[0.2328, 0, -0.7328]$. As collected in Table. 2, in fact, all those reproduced coexisting attractors have almost the same sets of Lyapunov exponents.

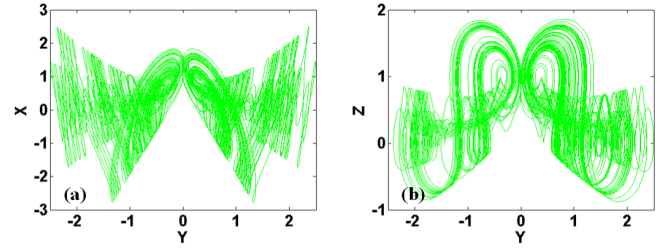


Figure 16 Pseudo-double-scroll attractor in system (7) with $a = 3.55, b = 0.5, c = d = 0$ under initial condition $(1, 2, 1)$: (a) y - x , (b) y - z .

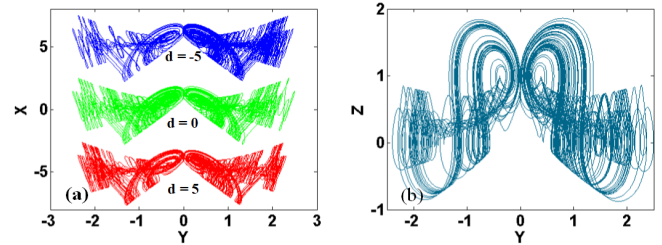


Figure 17 Chaotic attractors in system (7) with $a = 3.55, b = 0.5, c = 0$: (a) y - x , (b) y - z . Here in the left plot, red is for $d = 5$ and $IC = (-4, 2, 1)$, green is for $d = 0$ and $IC = (1, 2, 1)$ and blue is for $d = -5$ and $IC = (6, 2, 1)$; because of the same plot in y - z plane, here a third color is applied for representing each coexisting attractor.

POLARITY CONTROL BASED ON OFFSET BOOSTING

Moreover, the offset boosting can introduce polarity reversal leading to other regimes of systems with coexisting attractors if the polarity balance is maintained typically conditional symmetry is expectable (Li et al. 2020c). Revising the original system to be,

$$\begin{cases} \dot{x} = 1 - ayz \\ \dot{y} = z^2 - |z| \\ \dot{z} = x - bz \end{cases} \quad (9)$$

The offset in the dimension of x and y win the polarity return in the right hand of the equation breeding conditional symmetry,

$$\begin{cases} \dot{x} = 1 - a(|y| - e)z \\ \dot{y} = z^2 - |z| \\ \dot{z} = (|x| - f) - bz \end{cases} \quad (10)$$

It is clear that the offset boosting in the dimension x and y does not change the polarity of the left hand of Eq. (10) but gives birth to polarity reversal by the absolute value function, which is

■ **Table 2** Chaotic systems with flexible offset boosting and their basic properties

System	Parameters	LE_S	D_{KY}
(1)	$a = 3.55, b = 0.5$	0.1510, 0, -0.6510	2.2319
(2)(Case A)	$a = 3.55, b = 0.5$	0.1510, 0, -0.6510	2.2319
(3)(Case B)	$a = 3.55, b = 0.5$	0.1510, 0, -0.6510	2.2319
(4)(Case C)	$a = 3.55, b = 0.5$	0.23401, 0, -0.73402	2.3188
(4)(Case D)	$a = 3.55, b = 0.5$	0.14275, 0, -0.64275	2.2221
(5)(Case E)	$a = 2.2, b = 0.7$	0.13415, 0, -0.83416	2.1608
(4)(Case F)	$a = 3.57, b = 0.7$	0.22152, 0, -0.93029	2.2381
(6)(Case F)	$a = 4.5, b = 0.7$	0.12917, 0, -0.82917	2.1558
(7)	$a = 3.55, b = 0.5$	0.1477, 0, -0.64335	2.2228

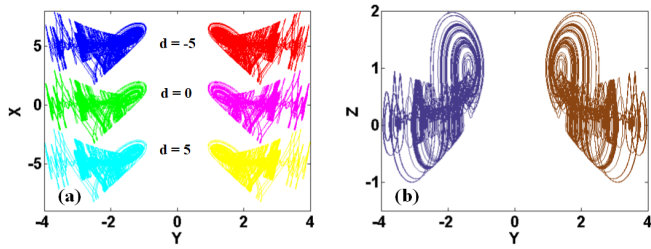


Figure 18 Chaotic attractors in system (7) with $a = 3.55, b = 0.5, c = 1$: (a) $y-x$, (b) $y-z$. Here in the left plot, red is for $d = -5$ and IC = (6, 1, 1), blue is for $d = -5$ and IC = (6, -1, 1), green is for $d = 0$ and IC = (1, -1, 1), magenta is for $d = 0$ and IC = (1, 1, 1), yellow is for $d = 5$ and IC = (-4, 1, 1) and cyan is for $d = 5$ and IC = (-4, -1, 1); because of the same plot in $y-z$ plane, here a third color is applied for representing each coexisting attractor.

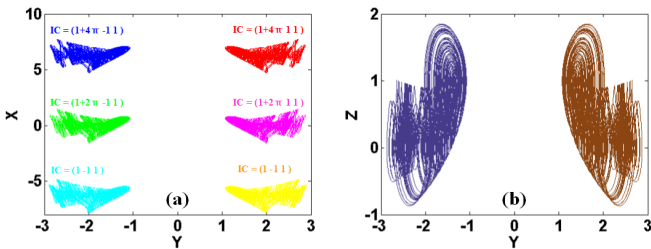


Figure 19 Chaotic attractors in system (8) with $a = 3.55, b = 0.5, c = 1$: (a) $y-x$, (b) $y-z$. Here because of the same plot in $y-z$ plane, a third color is applied for representing each coexisting attractor.

counteracted by the polarity reversal of z leading to conditional reflectal symmetry. As depicted in Fig. 20, coexisting chaotic attractors are produced by 2-D offset boosting in x and y dimensions where the polarity balance is retained by the inverse of z .

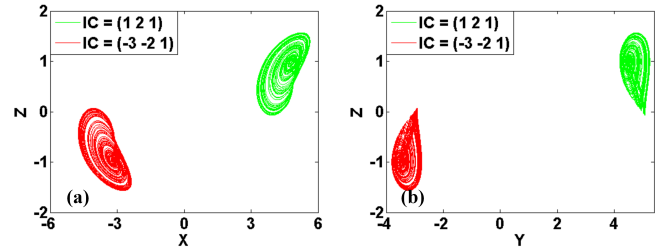


Figure 20 Coexisting attractors in conditional symmetrical system (10) with $a = 2, b = 0.8, e = f = 4$ induced by 2-D offset boosting in x and y dimensions: (a) $x-z$, (b) $y-z$.

As pointed in (Li and Sprott 2017; Li et al. 2021), offset boosting may create flexibly-selected repeller if it exists in a function for equilibria controlling. With the transformation like,

$$\begin{cases} \dot{x} = (1 - a(|y| - e)z)p \\ \dot{y} = (z^2 - |z|)p \\ \dot{z} = ((|x| - f) - bz)p \end{cases} \quad (11)$$

one of the coexisting attractors turns to be a repeller when the function p is introduced as $p = y$ or $p = y - 1$, as shown in Fig. 21. Since the coexisting attractors scatter in the y dimension with relatively larger distance, here the offset in the equilibria plane $y = 1$ creates desired repeller. Moreover, system (9) can be revised to be a time-reversible chaotic system (Li et al. 2021),

$$\begin{cases} \dot{x} = 1 - ay(|z| - g) \\ \dot{y} = (|z| - g)^2 - ||z| - g| \\ \dot{z} = x - b(|z| - g) \end{cases} \quad (12)$$

The time reversible property can be proved by the invariance of system (12) under the transformation of $t \rightarrow -t, x \rightarrow -x, y \rightarrow -y, z \rightarrow z + d$. Polarity balance is maintained by the offset boosting in the dimension of z giving coexisting attractor and repeller as shown in Fig. 22.

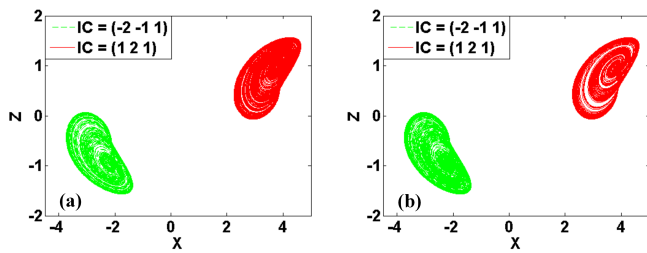


Figure 21 Coexisting chaotic attractor (red) and repeller (green) of system (11) with $a = 2, b = 0.8, e = f = 3$: (a) $p = y$, (b) $p = y - 1$.

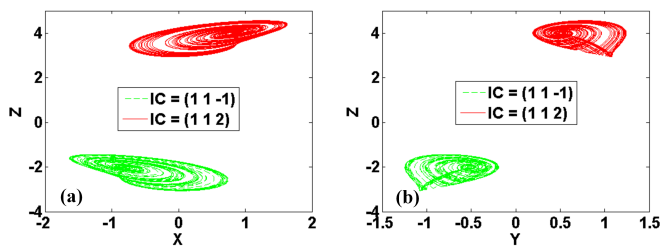


Figure 22 Coexisting chaotic attractor (red) and repeller (green) of system (12) with $a = 2, b = 0.8, g = 3$: (a) $x-z$, (b) $y-z$.

RESULTS AND DISCUSSION

Offset boosting of a chaotic signal or attractor represents corresponding attractor boosting. Extra introduced constant and initial condition can both trigger this process giving attractor boosting with any desired offset and producing chaotic signals with designed averaged values in a continuous or a discrete way. From the above demonstration, we can select proper approach to realize offset boosting according to our restriction. For obtaining a chaotic waveform with desired average, the offset booster is reliable since any DC power supply is easily available and selectable. For polarity control from the bipolar signal to monopolar signal or vice versa, direct constant control with a DC source can also accomplish this task effectively and output any desired stable signals.

For free access to the attractor with various offset, periodic function or absolute value function can also be introduced for attractor reproducing or doubling, where initial condition is applied to visit any included attractor. For this purpose, periodic functions may be introduced for free attractor reproducing. Attractor growing may happen in this case. Absolute value function can be pulled in a dynamical system for attractor doubling. For some specific systems, the insert of absolute value function may bring a polarity reversal giving conditional symmetry or time-reversible conditional symmetry.

Parameter-oriented and initial-condition-oriented offset boosting can be combined together for engineering application according to the engineering restriction. Furthermore, some other piecewise linear functions (Li et al. 2020a,b) can be designed for attractor

selecting and reproducing, where all the selected attractors can be arranged in any dimension or in any order if the offset is controlled harmoniously for all the attractors. Dynamic editing is heading to this direction for further exploration.

Acknowledgments

This work was supported financially by the National Natural Science Foundation of China (Grant No.: 61871230), the Natural Science Foundation of Jiangsu Province (Grant No.: BK20181410), and a project funded by the Priority Academic Program Development of Jiangsu Higher Education Institutions.

Conflicts of interest

The authors declare that there is no conflict of interest regarding the publication of this paper.

LITERATURE CITED

- Akgul, A., C. Arslan, and B. Aricioglu, 2019 Image authentication using chaotic mixing systems. *Chaos theory and applications* 1: 1–18.
- Akgul, A., H. Calgan, I. Koyuncu, I. Pehlivan, and A. Istanbulu, 2016 Chaos-based engineering applications with a 3D chaotic system without equilibrium points. *Nonlinear Dynamics* 84: 481–495.
- Bao, H., W. Liu, J. Ma, and H. Wu, 2020 Memristor initial-offset boosting in memristive neuron model with hidden firing patterns. *International Journal of Bifurcation and Chaos* 30: 2030029.
- C. Sprott, J., 2010 *Elegant chaos: algebraically simple chaotic flows*. World Scientific p. 304.
- C. Sprott, J. and A. Xiong, 2015 Classifying and quantifying basins of attraction. *Chaos* 25: 2230.
- Chen, M., X. Ren, H. Wu, Q. Xu, and B. Bao, 2019 Periodically varied initial offset boosting behaviors in a memristive system with cosine memductance. *Frontiers of Information Technology and Electronic Engineering* 20: 1706–1716.
- Chen, M., X. Ren, H. Wu, Q. Xu, and B. Bao, 2020 Interpreting initial offset boosting via reconstitution in integral domain. *Chaos, Solitons and Fractals* 131: 109544.
- Ding, D., X. Shan, J. Luo, Y. Hu, and L. Ding, 2020 Initial boosting phenomenon of a fractional-order hyperchaotic system based on dual memristors. *Modern Physics Letters B* 34: 2050191.
- Falco, A. D., T. F. Krauss, and A. Fratalocchi, 2012 Lifetime statistics of quantum chaos studied by a multiscale analysis. *Applied Physics Letters* 100: 1914–1917.
- Gu, S., S. He, H. Wang, and B. Du, 2021 Analysis of three types of initial offset-boosting behavior for a new fractional-order dynamical system. *Chaos Solitons and Fractals* 143: 110613.
- Kengne, J., G. Leutcho, and A. Telem, 2018 Reversals of period doubling, coexisting multiple attractors, and offset boosting in a novel memristive diode bridge-based hyperjerk circuit. *Analog Integrated Circuits and Signal Processing* 101: 379–399.
- Kingni, S. T., K. Rajagopal, S. Cicek, A. Srinivasan, and Karthikeyan, 2020 Dynamic analysis, FPGA implementation, and cryptographic application of an autonomous 5d chaotic system with offset boosting. *Frontiers of Information Technology and Electronic Engineering* 21: 950–961.
- Li, C., G. Chen, J. Kurths, T. Lei, and Z. Liu, 2020a Dynamic transport: from bifurcation to multistability. *Communications in Nonlinear Science and Numerical Simulation* 95: 105600.
- Li, C., Z. Gu, Z. Liu, S. Jafari, and T. Kapitaniak, 2021 Constructing chaotic repellers. *Chaos Solitons and Fractals* 142: 110544.

- Li, C., T. Lei, X. Wang, and G. Chen, 2020b Dynamics editing based on offset boosting. *Chaos* **30**: 063124.
- Li, C., T. Lu, G. Chen, and H. Xing, 2019 Doubling the coexisting attractors. *Chaos* **29**: 051102.
- Li, C. and J. C. Sprott, 2016 Variable-boostable chaotic flows. *International Journal for Light and Electron Optics* **127**: 10389–10398.
- Li, C. and J. C. Sprott, 2017 How to bridge attractors and repellers. *International Journal of Bifurcation and Chaos* **27**: 1750149.
- Li, C., J. C. Sprott, W. Hu, and Y. Xu, 2017a Infinite multistability in a self-reproducing chaotic system. *International Journal of Bifurcation and Chaos* **27**: 1750160.
- Li, C., J. Sun, J. C. Sprott, and T. Lei, 2020c Hidden attractors with conditional symmetry. *International Journal of Bifurcation and Chaos* **30**: 2030042.
- Li, C., W. Xiong, and G. Chen, 2017b Diagnosing multistability by offset boosting. *Nonlinear Dynamics* **90**: 1335–1341.
- Liu, J., G. Chen, and X. Zhao, 2020 Generalized synchronization and parameters identification of different-dimensional chaotic systems in the complex field. *Fractals* **29**: 2150081–1–13.
- Lu, T., C. Li, S. Jafari, and F. Min, 2019 Controlling coexisting attractors of conditional symmetry. *International Journal of Bifurcation and Chaos* **29**: 1950207.
- Lu, T., C. Li, X. Wang, C. Tao, and Z. Liu, 2020 A memristive chaotic system with offset-boostable conditional symmetry. *The European Physical Journal Special Topics* **229**: 1059–1069.
- Ma, C., J. Mou, L. Xiong, S. Banerjee, and X. Han, 2021 Dynamical analysis of a new chaotic system: asymmetric multistability, offset boosting control and circuit realization. *Nonlinear Dynamics* **103**: 1–14.
- Mezatio, B. A., M. T. Motchongom, B. W. Tekam, R. Kengne, R. Tchitnga, *et al.*, 2019 A novel memristive 6d hyperchaotic autonomous system with hidden extreme multistability. *Chaos Solitons and Fractals* **120**: 100–115.
- Wang, S., C. Wang, and C. Xu, 2020 An image encryption algorithm based on a hidden attractor chaos system and the knuth–durstenfeld algorithm. *Optics and Lasers in Engineering* **128**: 105995.
- Wu, H., Y. Ye, B. Bao, M. Chen, and Q. Xu, 2019a Memristor initial boosting behaviors in a two-memristor-based hyperchaotic system. *Chaos Solitons and Fractals* **121**: 178–185.
- Wu, H., Y. Ye, M. Chen, Q. Xu, and B. Bao, 2019b Periodically switched memristor initial boosting behaviors in memristive hypogenetic jerk system. *IEEE Access* **7**: 1–1.
- Yuan, F., Y. Deng, Y. Li, and G. Wang, 2019 The amplitude, frequency and parameter space boosting in a memristor–meminductor-based circuit. *Nonlinear Dynamics* **96**: 389–405.
- Zhang, S., Y. Zeng, Z. Li, and C. Zhou, 2018 Hidden extreme multistability, antimonotonicity and offset boosting control in a novel fractional-order hyperchaotic system without equilibrium. *International Journal of Bifurcation and Chaos* **28**: 1850167.
- Zhang, S., J. Zheng, X. Wang, Z. Zeng, and S. He, 2020 Initial offset boosting coexisting attractors in memristive multi-double-scroll hopfield neural network. *Nonlinear Dynamics* **102**: 2821–2841.
- Zhao, X., J. Liu, J. Mou, C. Ma, and F. Yang, 2020 Characteristics of a laser system in complex field and its complex self-synchronization. *The European Physical Journal Plus* **135**: 1–17.

How to cite this article: Li, C., Jiang, Y., and Ma, X. On offset boosting in chaotic system. *Chaos Theory and Applications*, 3(2), 47-54, 2021.

Dynamical Analysis and Microcontroller Implementation of Linear Resistor-Capacitor Shunted Josephson Junction Model

Dianorré Tokoue Ngatcha^{ID}*,1, Alhadji Abba Oumate^{ID}β,2, Alex Stephane Kemnang Tsafack^{ID}γ,3 and Sifeu Takougang Kingni^{ID}δ,4

*Department of Automotive and Mechatronics Engineering, National Higher Polytechnic School of Douala, University of Douala, Box 24, 2701 Douala, Cameroon, ^βDepartment of Physics, Faculty of Science, University of Maroua, P.O. Box 814, Maroua, Cameroon, ^γResearch unit of Condensed Matter of Electronics and Signal Processing, Department of Physics, Faculty of Sciences, University of Dschang, P. O. Box 67, Dschang, Cameroon, ^δDepartment of Mechanical, Petroleum and Gas Engineering, Faculty of Mines and Petroleum Industries, University of Maroua, P.O. Box 46, Maroua, Cameroon.

ABSTRACT Theoretical analysis and microcontroller implementation of linear resistor-capacitor shunted Josephson junction (LRCSJJ) model are studied in this paper. The rate-equations describing the LRCSJJ model has no or two equilibrium points. One of the equilibrium points is a saddle node and the other one is a stable node. The hysteresis loop of current-voltage curves increases with the rising of the capacitance of Josephson junction (JJ). Excitable mode, limit cycle, periodic and chaotic behaviors are found in LRCSJJ model with external alternative current (AC) source thanks to the two modulation parameters largest Lyapunov exponents (LLE) diagram. LRCSJJ model exhibits two different shapes of chaotic attractors by varying the modulation amplitude. Finally, the existence of chaotic behaviors is confirmed by microcontroller results obtained from the microcontroller implementation of LRCSJJ model.

KEYWORDS

Chaos
Josephson junction
Hysteresis loop
Excitable mode
Microcontroller implementation.

INTRODUCTION

Josephson junction devices have been studied by many researchers because they are very good candidates commonly exploited for the construction of complex systems for specific applications (Levi *et al.* 1978; Kautz and Monaco 1985; McCumber 1968; Zhang *et al.* 2011; Malishevskii and Uryupin 2020). In the literature, there is two main electrical rate-equations of JJ: Resistor and capacitor shunted JJ (RCSJJ) mode (Cawthorne *et al.* 1998) and resistor, capacitor and inductive shunted JJ (RCISJJ) model (Dana *et al.* 2006; Whan *et al.* 1995). Typically by using RCSJJ model to describe JJ, resulted in a fairly good agreement with experiment. Nonetheless, it was not able to generate significant features of experimental current-voltage characteristics. Better agreement with experiment is found when the RCSJJ model is adopted by inserting an inductor in series with the shunt resistor in order to obtain the RCLSJJ model

(Cawthorne *et al.* 1998; Dana *et al.* 2006; Whan *et al.* 1995; Stewart 1968; Neumann and Pikovsky 2003; Takougang Kingni *et al.* 2017).

In fact, there is four models of JJ namely: Nonlinear RCSJJ model (Levi *et al.* 1978; Likharev 1986), LRCSJJ model (Salam and Sastry 1985; Bartuccelli *et al.* 1986), nonlinear RCLSJJ model (Cawthorne *et al.* 1998; Dana *et al.* 2006; Whan *et al.* 1995; Stewart 1968), and linear RCISJJ model (Neumann and Pikovsky 2003; Takougang Kingni *et al.* 2017) have been reviewed to check if a JJ device can be used as a transmitter and receiver in chaos based communications. The two RCSJJ models show chaotic behaviors when driven by external sinusoidal current source (Levi *et al.* 1978; Likharev 1986; Salam and Sastry 1985; Bartuccelli *et al.* 1986) whereas the two RCISJJ models generated chaotic behaviors with external DC (Cawthorne *et al.* 1998; Dana *et al.* 2006; Whan *et al.* 1995; Stewart 1968; Neumann and Pikovsky 2003; Takougang Kingni *et al.* 2017; Dana *et al.* 2001). The RCISJ models have been revealed more appropriate in high-frequency applications (Cawthorne *et al.* 1998; Dana *et al.* 2006; Whan *et al.* 1995; Stewart 1968; Neumann and Pikovsky 2003; Takougang Kingni *et al.* 2017). In (Dana *et al.* 2006), Dana *et al.* have been studied how the chaos found in nonlinear RCLSJJ model could be applied as a chaos generator for communications.

The authors of (Takougang Kingni *et al.* 2017) have been studied

Manuscript received: 8 June 2021,

Revised: 14 July 2021,

Accepted: 21 July 2021.

¹ tokouengatcha1@gmail.com

² oumatealhadji.ao@gmail.com

³ alexstephanekemnang@gmail.com (Corresponding Author)

⁴ stkingni@gmail.com

the dynamical analysis of linear RCISJJ model and its fractional-order form as well as its application to digital cryptography. Synchronization of two coupled linear RCISJJ models via cyclic coupling and its microcontroller-based implementation was reported by Ojo and al (Ojo *et al.* 2019). Few research works have been reported on RCSJJ models (Levi *et al.* 1978; Likharev 1986; Salam and Sastry 1985; Bartuccelli *et al.* 1986; Kautz and Monaco 1985). Salam and Shastry have been studied the dynamical behaviors of LRCSJJ model actuated both by direct current (DC) and AC with emphasis on the AC case (Salam and Sastry 1985). In (Bartuccelli *et al.* 1986), Chaos in LRCSJJ model driven AC have been investigated by using the Melnikov method. Chaotic behavior in LRCSJJ model driven by an AC have been studied through digital simulations by Kantz and Monaco (Kautz and Monaco 1985). McCumber have been investigated on the alternative current impedance and he saw the influence both in the response time and the DC voltage-current characteristics (McCumber 1968).

This paper studies the dynamical behavior and the microcontroller implementation of the LRCSJJ model. The paper is organized as follows: Theoretical analysis of LRCSJJ model is studied in Section 2. Microcontroller implementation of the LRCSJJ model is investigated in Section 3. Section 4 presents the conclusion.

DYNAMICAL ANALYSIS OF LRCSJJ MODEL

LRCSJJ model (Kautz and Monaco 1985) is represented in Fig. 1.

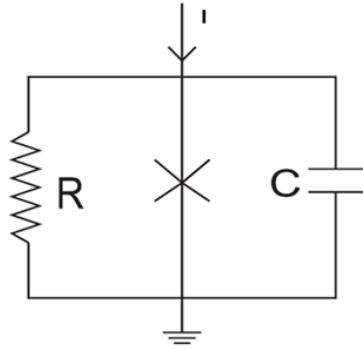


Figure 1 Schematic view of LRCSJJ model.

The circuit of Fig. 1 consists of the external current source I , capacitor C , linear resistor R and JJ element connected in parallel. A voltage V is developed across the JJ due to the application of by applying the Kirchhoff law, the following equations are obtained:

$$v = \frac{h}{2\pi e} \frac{d\phi}{dt'} \quad (1)$$

$$C \frac{dv}{dt'} + \frac{v}{R} + I_J = I \quad (2)$$

where v is the voltage, h is the Planck constant, t' is the time, e is the electron charge, $I_J = I_{JC} \sin \phi$ is the JJ current and $\phi = \phi_2 - \phi_1$ is the phase difference. By introducing the following parameters $t = \omega_0 t'$, $i(t) = I/I_{CJ}$, $\omega_0 = (2\pi e I_{JC}/hC)^{1/2}$, $V = v\sqrt{2\pi e C/hI_{CJ}}$ and $\beta_C = 2\pi e R^2 C I_{CJ}/h > 0$, the set of Eqs. (1, 2) can be normalized as:

$$\frac{d\phi}{dt} = V \quad (3)$$

$$\frac{dV}{dt} = i(t) - V/\sqrt{\beta_C} - \sin(\phi) \quad (4)$$

where β_C is the capacitance of JJ

Analytical and numerical analysis of LRCSJJ model driven by external DC source

The external current source is considered as a DC: $i(t) = i_{dc}$, LRCSJJ model displays two equilibrium points $E_1 = (\arcsin(i_{dc}), 0)$ and $E_2 = (\pi - \arcsin(i_{dc}), 0)$ for $i_{dc} \leq 1$ whereas it has no-equilibrium point for $i_{dc} > 1$. The characteristic equation associated to the equilibrium point $E_1 = (\arcsin(i_{dc}), 0)$ is

$$\lambda^2 + \frac{1}{\sqrt{\beta_C}}\lambda + \sqrt{1-i^2} = 0 \quad (5)$$

and the eigenvalues are

$$\lambda_1 = \frac{1}{2\sqrt{\beta_C}} \left(-1 + \sqrt{1 - 4\beta_C \sqrt{1 - i_{dc}^2}} \right) \quad (6)$$

and

$$\lambda_2 = \frac{1}{2\sqrt{\beta_C}} \left(-1 - \sqrt{1 - 4\beta_C \sqrt{1 - i_{dc}^2}} \right). \quad (7)$$

Since $\lambda_1 < 0$ and $\lambda_2 < 0$, the equilibrium point $E_1 = (\arcsin(i_{dc}), 0)$ is a stable node. The characteristic equation at the equilibrium point $E_2 = (\pi - \arcsin(i_{dc}), 0)$ is

$$\lambda^2 + \frac{1}{\sqrt{\beta_C}}\lambda - \sqrt{1-i_{dc}^2} = 0 \quad (8)$$

and the eigenvalues are

$$\lambda_1 = \frac{1}{2\sqrt{\beta_C}} \left(-1 + \sqrt{1 + 4\beta_C \sqrt{1 - i_{dc}^2}} \right) \quad (9)$$

and

$$\lambda_2 = \frac{1}{2\sqrt{\beta_C}} \left(-1 - \sqrt{1 + 4\beta_C \sqrt{1 - i_{dc}^2}} \right). \quad (10)$$

Since $\lambda_1 > 0$ and $\lambda_2 < 0$, the equilibrium point $E_2 = (\pi - \arcsin(i_{dc}), 0)$ is a saddle node.

Figure 2 presents the current-voltage curve for given values of the capacitance of JJ.

When the DC $i(t) = i_{dc}$ increases (black line in Fig. 2), the trajectories of voltage exhibits excitable mode for $i(t) = i_{dc} \leq 1.0$. The voltage exhibits period-1-oscillations for $i(t) = i_{dc} > 1.0$. By decreasing DC $i(t) = i_{dc}$ (see red line in Fig. 2), the voltage depicts the similar dynamical behaviors as in Fig. 2 (black line). By comparing the two sets of data [for increasing (black line) and decreasing (red line)] used to plot Fig. 2, there is a region of the DC called hysteresis loop where the voltage V exhibits the similar dynamical behaviors as seen in Fig. 2 (black line) but the amplitudes of the voltage V are different. So, LRCSJJ model shows bistability phenomenon in the hysteresis loop. By increasing the capacitance of JJ β_C , the hysteresis loop increases.

Numerical analysis of LRCSJJ model driven by external AC source

In this subsection, we consider the external current source is to be an AC: $i(t) = i_{dc} + i_m \sin(\omega_m t)$ where the parameters i_{dc} , i_m and ω_m are DC, modulation current and modulation pulsation, respectively. The two modulation parameters LLE diagram of the LRCSJJ model is illustrated in Fig. 3.

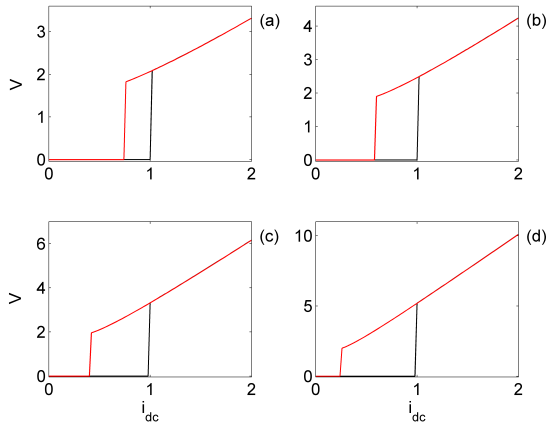


Figure 2 Current-voltage curve for given values of β_C : (a) $\beta_C = 2.25$, (b) $\beta_C = 4$, (c) $\beta_C = 9$ and (d) $\beta_C = 25$. The current-voltage curves are found by increasing (black line) and decreasing (red line) the DC $i = i_{dc}$.

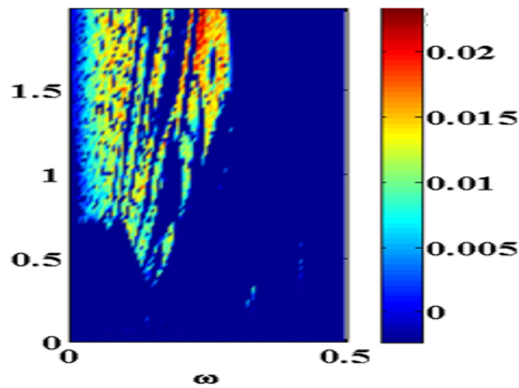


Figure 3 Two parameters LLE diagram of the LRCSJJ model in (ω, i_m) space for $i_{dc} = 0.3$ and $\beta_C = 25$.

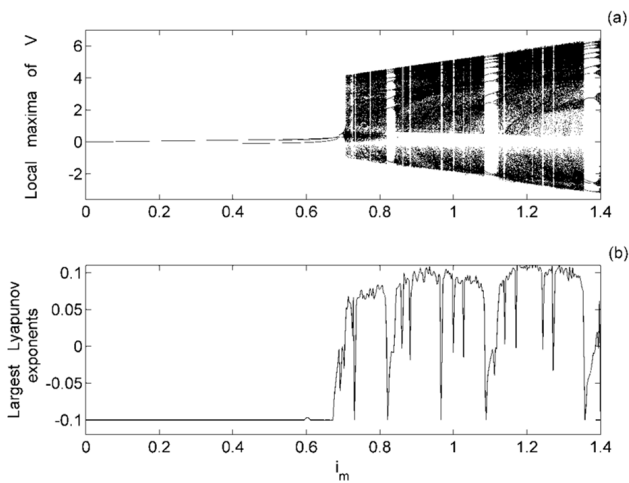


Figure 4 Bifurcation diagrams of $V(t)$ (a) and LLE (b) versus the parameter i_m for $i_{dc} = 0.3$, $\omega_m = 0.25$ and $\beta_C = 25$.

Excitable mode, periodic behaviors and chaotic behaviors regions are illustrated in Fig. 3. The bifurcation diagram versus the parameter i_m and LLE are depicted in Fig. 4 for $\omega_m = 0.25$.

By increasing the amplitude of modulation i_m from 0.0001 to 1.4, the voltage $V(t)$ in Fig. 4(a) displays limit cycle, period-2-oscillation, period-3-oscillation, period-2-oscillations then period-doubling bifurcation to chaos encrusted with periodic windows. The LLE of Fig. 4(b) confirms the results of Fig. 4(a). Figure 5 depicts the chaos obtained in Fig. 4 for given values of parameter i_m .

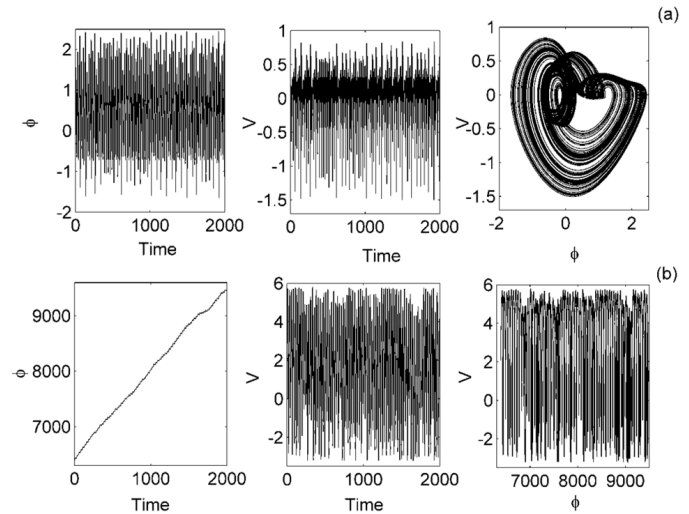


Figure 5 Time histories of ϕ , V , and phase planes for given values of parameter i_m : $i_m = 0.705$ and $i_m = 1.2$, are $i_{dc} = 0.3$, $\omega_m = 0.25$ and $\beta_C = 25$. The initial conditions are $(\phi(0) = 0, V(0) = 0)$.

For $i_m = 0.705$, the phase difference and the voltage exhibit chaotic attractors as seen in Fig. 5(a). While in Fig. 5(b) for $i_m = 1.2$, the phase difference does not depict chaotic oscillations and the voltage displays chaotic oscillations. The phase portraits in Fig. 5 shows two different shapes of chaotic attractors for two given values of amplitude of modulation i_m .

MICROCONTROLLER IMPLEMENTATION OF LRCSJJ MODEL

The microcontroller implementation of LRCSJJ model is presented in Fig. 6.

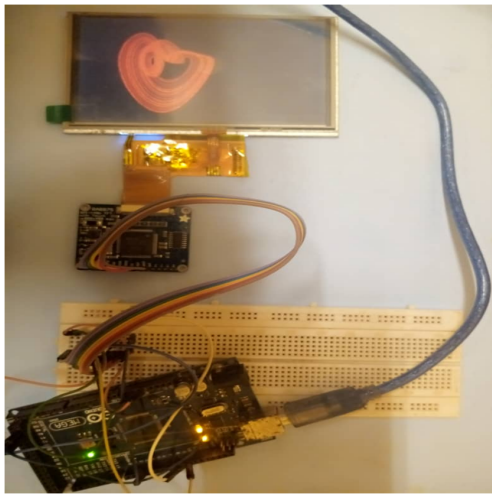


Figure 6 Microcontroller design circuit of the LRCSJJ model.

The microcontroller implementation of RCSJJ model shown in Fig. 6 is based on the Arduino. Fig. 7 presents the time series and phase portraits obtained from the microcontroller implementation of the LRCSJJ model.

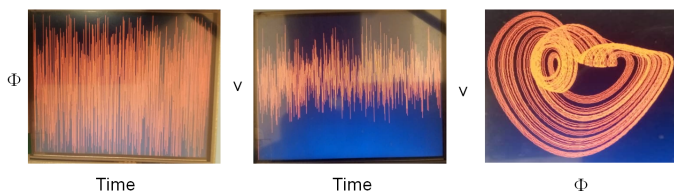


Figure 7 Time series and phase portrait obtained from the microcontroller implementation of LRCSJJ model.

The microcontroller results of Fig. 7 are qualitatively matched with the results of Fig. 5(a). Thus, the existence of chaotic behaviors found in LRCSJJ model is confirmed.

CONCLUSION

This paper deals with the theoretical analysis and microcontroller implementation of linear resistor-capacitor shunted Josephson junction model. The rate-equations describing the linear resistive-capacitive shunted Josephson junction model has two or no equilibrium points relying on the external direct current source. The stability analysis of the two equilibrium points of linear resistor-capacitor shunted Josephson junction model was investigated. The increasing of the capacitance of Josephson junction led to an increase in the hysteresis loop of current-voltage curves. For given modulation parameters of external current source, linear resistor-capacitor shunted Josephson junction model displayed two different shapes of chaotic attractors, periodic attractors, limit cycle and excitable mode. The existence of chaotic behaviors was confirmed by microcontroller results obtained from the microcontroller implementation of linear resistor-capacitor shunted Josephson junction model.

Conflicts of interest

The authors declare that there is no conflict of interest regarding the publication of this paper.

LITERATURE CITED

- Bartuccelli, M., P. L. Christiansen, N. F. Pedersen, and M. P. Sørensen, 1986 Prediction of chaos in a Josephson junction by the Melnikov-function technique. *Physical Review B* **33**: 4686.
- Cawthorne, A., C. Whan, and C. Lobb, 1998 Complex dynamics of resistively and inductively shunted Josephson junctions. *Journal of Applied Physics* **84**: 1126–1132.
- Dana, S. K., D. C. Sengupta, and K. D. Etoh, 2001 Chaotic dynamics in Josephson junction. *IEEE Transactions on Circuits and Systems I: Fundamental Theory and Applications* **48**: 990–996.
- Dana, S. K., D. C. Sengupta, and C.-K. Hu, 2006 Spiking and bursting in Josephson junction. *IEEE Transactions on Circuits and Systems II: Express Briefs* **53**: 1031–1034.
- Kautz, R. L. and R. Monaco, 1985 Survey of chaos in the rf-biased Josephson junction. *Journal of Applied Physics* **57**: 875–889.
- Levi, M., F. C. Hoppensteadt, and W. Miranker, 1978 Dynamics of the Josephson junction. *Quarterly of Applied Mathematics* **36**: 167–198.
- Likharev, K., 1986 Dynamics of Josephson junctions and circuits. *Gordon and Breach*. New York p. 92.
- Malishevskii, A. and S. Uryupin, 2020 Current-voltage characteristics of radiating Josephson sandwich. *Physics Letters A* **384**: 126515.
- McCumber, D., 1968 Effect of ac impedance on dc voltage-current characteristics of superconductor weak-link junctions. *Journal of Applied Physics* **39**: 3113–3118.
- Neumann, E. and A. Pikovsky, 2003 Slow-fast dynamics in Josephson junctions. *The European Physical Journal B-Condensed Matter and Complex Systems* **34**: 293–303.
- Ojo, K., A. Adelakun, and A. Oluyinka, 2019 Synchronisation of cyclic coupled Josephson junctions and its microcontroller-based implementation. *Pramana* **92**: 1–7.
- Salam, F. and S. Sastry, 1985 Dynamics of the forced Josephson junction circuit: the regions of chaos. *IEEE Transactions on Circuits and Systems* **32**: 784–796.
- Stewart, W., 1968 Current-voltage characteristics of Josephson junctions. *Applied Physics Letters* **12**: 277–280.
- Takougang Kingni, S., G. Fautso Kuate, R. Kengne, R. Tchitanga, and P. Wofo, 2017 Analysis of a non-equilibrium linear resistive-capacitive-inductance shunted junction model, dynamics, synchronization, and application to digital cryptography in its fractional-order form. *Complexity* **2017**.
- Whan, C., C. Lobb, and M. Forrester, 1995 Effect of inductance in externally shunted Josephson tunnel junctions. *Journal of Applied Physics* **77**: 382–389.
- Zhang, Z., K. Chau, Z. Wang, F. Li, and J. Li, 2011 Analysis of chaos in Josephson junctions with external magnetic field for high-precision voltage measurement in electric vehicles. *IEEE Transactions on Applied Superconductivity* **22**: 4904704–4904704.

How to cite this article: Ngatcha, D. T., Oumate, A. A., Kemnang Tsafack A. S., and Kingni, S. T. Dynamical analysis and microcontroller implementation of linear resistor-capacitor shunted Josephson junction model. *Chaos Theory and Applications*, 3(2), 55–58, 2021.

An Efficient Design Procedure to Implement the Fractional-Order Chaotic Jerk Systems with the Programmable Analog Platform

Nimet Korkmaz ^{*,1} and Ibrahim Ethem SACU ^{id α,2}

*Department of Electrical and Electronics Engineering, Kayseri University, Kayseri 38280, Turkey, ^αDepartment of Clinical Engineering Research Center, Erciyes University, Kayseri 38039, Turkey.

ABSTRACT An effective design procedure has been introduced for implementing the fractional order integrator structures with a modified low pass filters (LPFs) and its functionality is verified by realizing a fractional-order chaotic system. In these applications, the state variables of the fractional-order Sprott's Jerk system are emulated by these first order LPFs. Since the discrete device based designs have the hard adjustment features and the circuit complexities; the realizations of these LPFs are carried out with the Field Programmable Analog Arrays (FPAAs), sensitively. Hence, the introduced LPF based method has been applied to the fractional order Sprott's Jerk systems and these fractional-order systems, which are built by the several nonlinear functions, have been implemented with a programmable analog device. In this context, the minimum fractional-orders of the Sprott's Jerk systems are calculated by considering the stability of the fractional-order nonlinear systems. After that, these systems are simulated by employing the Grünwald-Letnikov (G-L) fractional derivative method by using a common fractional-order. Thus, the stability analyses of the fractional-order Sprott's Jerk system are supported by the numerical simulation results. After the numerical simulation stage, the design procedures of the FPAA based implementations of the Sprott's Jerk systems have been dealt with in detail. Finally, thanks to the introduced first-order LPF method, the hardware realizations of the Sprott's Jerk systems have been achieved successfully with a single FPAA device.

KEYWORDS

Fractional-order nonlinear system
Sprott's Jerk System
Low pass filter
FPAAs

INTRODUCTION

After the discovery of the Lorenz's chaotic system, the chaos concepts, the chaotic stability and the circuit implementations of the chaotic structures are well documented in the literature. Simulations of the chaotic attractors by solving two- or higher dimensional ordinary differential equations with numerical analysis tools or generations of these structures by emulating their mathematical descriptions with the several electronic hardware have become more interesting in the last few decades (Kiliç 2010). However, expressing a nonlinear system with simple definitions is very important in terms of both adaptation of the system to different

research fields and applicability to the problems in real life. Thus, these systems have been studied easily; also they have found an extensive application field in scientific engineering problems such as quantum chaos (Stöckmann 1999), chaos-based secure communications (Chen and Ueta 2002), to truly random number generator (Öztürk and Kiliç 2019) and the fractional-order definitions of the chaotic systems (Tlelo-Cuautle *et al.* 2020). Among these scientific accretions about the chaotic systems, Sprott's chaotic models have taken a considerable attention in the literature thanks to their simplicities and rich contents (Sprott 1994). This simple chaotic system is based on "Jerk systems" and the source of its rich contents is to include the different nonlinear functions in the system definition (Sprott 1997, 2000b,a; Ahmad and Sprott 2003).

The simplicities of the nonlinear systems provide an extra advantage for the fractional-order definition, because the fractional order models have the extra degrees and these methods enrich the analysis with more details in new dimensions. Thus, the real time

Manuscript received: 14 July 2021,

Revised: 9 August 2021,

Accepted: 11 August 2021.

¹ nimetkorkmaz@kayseri.edu.tr (Corresponding Author)

² iesacu@erciyes.edu.tr

problems and systems are able to be modeled by the fractional equations more accurately than the integer ones. Fractional calculus has found various applications in areas such as control system theory, biochemistry and medicine, circuit theory and design (Elwakil 2010). While the fractional-order PID controllers provide an extra freedom for tuning of time and frequency responses in the control system theory (Deniz et al. 2019); the fractional calculus is used for modeling the measured impedance versus the frequency of the investigated material in the biochemistry (Azar et al. 2018). Besides, the fractional capacitor (-fractance) or fractional inductance concepts are brought in the literature and these structures are adapted to the canonical theories of the integer order RC-RL-RLC circuits in the circuit theory (Krishna and Reddy 2008; Atangana and Alkahtani 2015). The main circuit applications such as oscillators, filters, differentiators and integrators etc. are also built by utilizing their fractional-order definitions (Radwan et al. 2008; Sacu and Alci 2019; Chen and Moore 2002; Charef 2006). The most important advantages of the fractional-order systems are able to be listed as follows: i) The high frequency real-time signals are generated with the fractional-order oscillators (Ahmad et al. 2001), ii) Both the frequency and the phase shifts among these generated signals are controlled by tuning the fractional-orders of the oscillators (Maundy et al. 2012), iii) The fractional-order differentiators and integrators provide adjustable phase shifts depending on the fractional order (Krishna 2011), iv) The slope of the filter response, the cutoff frequency (-center frequency) and the quality factor in the fractional filters are changed by adjusting the fractional-orders (Radwan et al. 2009), and v) the fractional-order controllers can provide robust performance (Caponetto 2010). Considering the advantages listed above, the fractional-order chaotic oscillators have become the one of the most important research fields of the nonlinear circuits and systems in the recent years.

The usage of the numerical simulation results is an often referred approach to demonstrate the effectiveness of the obtained results in the scientific studies, which are about the fractional-order chaotic oscillators. Two alternative numerical analyses methods are commonly used to simulate the fractional-order chaotic oscillators (Arena 2000; Chen et al. 2016). First of them is based on Grünwald-Letnikov (G-L) fractional derivative that is used for calculation of the time domain responses of the studied systems and this method demands more memory size. In the second method, the fractional integral operator $1/s^q$ ($0 < q < 1$ is fractional order) is approximated by the high order integer transfer functions within a limited frequency band. These high order integer transfer functions are generally implemented by the R-C networks, but there is a tradeoff between simplicity of the implementation and frequency band in this method. On the other hand, although the circuit implementations of the fractional-order chaotic systems have impressive advantages, the number of their hardware implementations is limited. A large part of these studies are usually realized with discrete devices by using the coupled R-C circuits (Radwan and Salama 2012; Gómez et al. 2013; Gómez-Aguilar et al. 2017). Also, since the programmable and reconfigurable analog/digital devices have several effective specialties such as the flexible designing, the low time and equipment costs and the rapid prototyping, a few the programmable analog/digital devices based hardware validation studies about the fractional-order chaotic systems are also available in the literature (Petráš 2011; Singh et al. 2020). However, the followed processes in these available studies do not offer a common design procedure in order to implement programmable analog device based implementations of the fractional-order chaotic systems.

In this context, an effective alternative design process will be suggested for realizing of the fractional-order chaotic systems with the electronic hardware in this study. In this introduced procedure, the state variables of the fractional-order chaotic systems are emulated by the modified first order low-pass filters (LPFs), so the hardware usage cost and the circuit complexities have been decreased at the beginning of the hardware design process. The analog filter designs and their realizations are carried out with the Field Programmable Analog Arrays (FPAAs), logically. Thus, the introduced method has been applied to the fractional order Sprott's Jerk systems and the best of our knowledge, the fractional order Sprott's Jerk systems, which are built by the several nonlinear functions, have been implemented with a programmable analog device. To this end, the minimum fractional-orders of the state variables of the Sprott's Jerk systems are derived by taking into stability of the nonlinear systems consideration at the equilibrium points. After the determination of the fractional orders, the Sprott's Jerk systems, which include several nonlinear functions, are simulated by employing the G-L fractional derivative method. Then, the details of the introduced alternative design process have been handled. Finally, by means of this method, the hardware realizations of the Sprott's Jerk systems have been achieved successfully with a single FPAA device.

This paper is organized as follows: The general background about the Sprott's Jerk systems and their fractional-order counterparts are given in Section 2. The main definition of the G-L fractional derivative method and the numerical simulation results of the fractional-order Sprott's Jerk systems are also presented in Section 2. The alternative design procedure is introduced in Section 3 and the FPAA based implementation results of the fractional-order Sprott's Jerk systems are also given in this section. The discussions about the performance evaluations of the introduced methods and the concluding remarks are given in the last section.

THE GENERAL BACKGROUND ABOUT THE FRACTIONAL-ORDER SPROTT'S JERK SYSTEMS

In 1994, Sprott offered several simple chaotic systems (Sprott 1994). After the response of the Gottlieb's question about the Jerk function (Gottlieb 1996), these simple chaotic systems have been adapted to an explicit third order form as $\ddot{x} = J(x, \dot{x}, \ddot{x})$. These redefined systems have been called Sprott's Jerk systems and defined by to following equations (Sprott 1997, 2000b,a; Ahmad and Sprott 2003):

$$\begin{aligned} \frac{dx}{dt} &= \dot{x} = y \\ \frac{d^2x}{dt^2} &= \ddot{x} = \dot{y} = z \\ \frac{d^3x}{dt^3} &= \ddot{\ddot{x}} = \dot{z} = F(x) - pz - y \end{aligned} \quad (1)$$

where, 'x', 'y' and 'z' are the state variables of this system. 'F(x)' is a nonlinear function and plays an important role in the chaos mechanism of the system. Several chaotic structures with different characteristics have been obtained by using these piecewise linear functions (PWLs), which have different nonlinear definitions as seen in Table 1 (Sprott 1997, 2000b,a; Ahmad and Sprott 2003). 'p' is a control parameter, the chaotic dynamics of this system change by depending on the values of 'p'.

Table 1 The nonlinear functions of the Sprott's Jerk system and the values of the nonlinear function's parameters

The Nonlinear Functions-' $F(x)$ '	Eq. No	Function Parameters	The minimum fractional orders
$F_1(x) = x - r$	(2)	$r = 2, p = 0.35$	$q_{\min} > 0.885$
$F_2(x) = -Bx + C\text{sgn}(x)$	(3)	$B = 1.2, C = 2, p = 0.6$	$q_{\min} > 0.904$
$F_3(x) = B(x^2/C - C)$	(4)	$B = 0.58, C = 1, p = 0.42$	$q_{\min} > 0.831$
$F_4(x) = Bx(x^2/C - 1)$	(5)	$B = 1.6, C = 5, p = 0.4$	$q_{\min} > 0.848$
$F_5(x) = -Bx(x^2/C - 1)$	(6)	$B = 0.9, C = 0.47, p = 0.4$	$q_{\min} > 0.837$
$F_6(x) = -B[x - 2 \tanh(Cx)/C]$	(7)	$B = 2.15, C = 1, p = 0.58$	$q_{\min} > 0.864$

In the literature, several chaotic oscillators such as Chua, Rössler, Duffing etc. have been redefined by using the fractional-order integrators (Petráš 2011). The Sprott's Jerk system has been also transported a fractional order system in Ref (Ahmad and Sprott 2003). In Ref (Ahmad and Sprott 2003), only one state variable (' x ') is given as a fractional-order integrator. In our study, all state variables are dealt with as the fractional-order integrators and their fractional-orders are set to equal values. The values of the fractional-order are calculated by considering the stability of these nonlinear systems.

The stabilities of the fractional order nonlinear systems are as important as in the integer-order nonlinear systems. Although the Lyapunov criterion is commonly employed for the stability of the integer nonlinear systems, this criterion is not valid for the fractional-order nonlinear systems. There are two methods in order to check the stabilities of the fractional-order nonlinear systems: In the case of the commensurate order fractional system, namely $q_1 = q_2 = \dots = q_n = q$, Tavazoei and Haeri (Tavazoei and Haeri 2007) have proposed a method. According to this method, if the arguments of all the eigenvalues $[\lambda_i (i = 1, 2, \dots, n)]$ of the system satisfy the $|\arg(\lambda_i)| > \frac{q\pi}{2}$ condition, the equilibrium points of this system are asymptotically stable. On the other hand, in the case of the incommensurate order fractional system, namely $q_1 \neq q_2 \neq \dots \neq q_n \neq q$, the stability of the system is determined as following (Tavazoei and Haeri 2008): If the arguments of all the roots λ of the Eq.8 satisfy the $|\arg(\lambda_i)| > \frac{\pi}{2m}$ condition, this system is the asymptotically stable, where m is the least common factor of the denominators of fractional orders and ' J ' is the Jacobian matrix.

$$\det(\text{diag}([\lambda^{mq} \quad \lambda^{mq} \quad \dots \quad \lambda^{mq}]) - J) = 0 \quad (8)$$

As mentioned before, all fractional-orders of the Sprott's Jerk systems are set to equal values in order to get a simple stability analysis and the fractional-order Sprott's Jerk system is given as in Eq. 9.

$$\begin{aligned} \frac{dx^q}{dt^q} &= y \\ \frac{dy^q}{dt^q} &= z \\ \frac{dz^q}{dt^q} &= F(x) - pz - y \end{aligned} \quad (9)$$

The fractional-order of the Sprott's Jerk systems including a PWL function in Eq.3 has been calculated as in the following part in terms of being an example of the stability analysis of the

fractional-order nonlinear systems. Firstly, the equilibrium points of the system are derived by equaling the right hand side of the equations in Eq.9 to zero. Then, three of equilibrium points of Eq. (9) are calculated for $p = 0.6$ and the values of the equilibrium points are reported as $E_1(-2/1.2, 0, 0)$, $E_2(0, 0, 0)$ and $E_1(2/1.2, 0, 0)$. The eigenvalues of this system are calculated as (' $0.1619 + i1.1282i$ ', ' $0.1619 - i1.1282i$ ', ' -0.9237 ') by utilizing the values of the equilibrium points with the $\det(\lambda I - J) = 0$ formula. After the determinations of the eigenvalues, the minimum fractional order is identified by using the method proposed by Tavazoei and Haeri (Tavazoei and Haeri 2007). The minimum fractional orders for the Sprott's Jerk system including the nonlinear functions in Eqs.2-7 are calculated by following these procedures and their values are also reported to Table 1.

After these calculations, the fractional-orders of the Sprott's Jerk systems are identified as $q = 0.95$ in order to provide a robust stability for all applications in this study. Then, the nonlinear functions in Table 1 have been adapted to the Eq.9 and the employability of the fractional-order has been verified by observing the results of the numerical analyses. Several effective methods such as the Riemann-Liouville, Caputo and Grünwald-Letnikov are improved for calculating the fractional derivatives in the literature (Arena 2000; Oldham and Spanier 1974; 199 1999). Here, the G-L method has been preferred due to its prevalent usage in the numerical analysis of the chaotic systems. This method is used for the numerical analyses of the Sprott's Jerk systems and this method is defined as in Eq. 10.

$${}_a D_t^q f(t) = \lim_{h \rightarrow 0} \frac{1}{h^q} \sum_{j=0}^{\lfloor \frac{t-a}{h} \rfloor} (-1)^j \binom{q}{j} f(t-jh) \quad (10)$$

Where ' a ' and ' t ' are bounds of derivative operation, ' h ' is the time step, ' $\lfloor \frac{t-a}{h} \rfloor$ ' means the integer part of the function and the binomial coefficients are expressed in terms of Gamma ' $\Gamma(*)$ ' function as in Eq.11.

$$\binom{q}{j} = \frac{\Gamma(q+1)}{\Gamma(j+1)\Gamma(q-j+1)} \quad (11)$$

Here, the G-L numerical analyses method has been applied to the fractional-order Sprott's Jerk systems, successfully. The obtained numerical simulation results of these systems are given in Figs.1a-f for the nonlinear functions in Eqs.2-7, respectively.

The value of the 'j' parameter is set to 5000 and 'h' is equal to 0.1. The initial conditions of the state variables are adjusted as $[(x(0) = 0.1, y(0) = 0, z(0) = 0)]$ in all numerical simulations.

As seen from the numerical simulation results given in Fig.1, the fractional-order Sprott's Jerk systems exhibit the chaotic behaviors for the $q = 0.95$ value. Additionally, these results support the results of the stability analyses in the previous part. Therefore, the all fractional orders of the Sprott's Jerk systems are taken as 0.95 in the following parts.

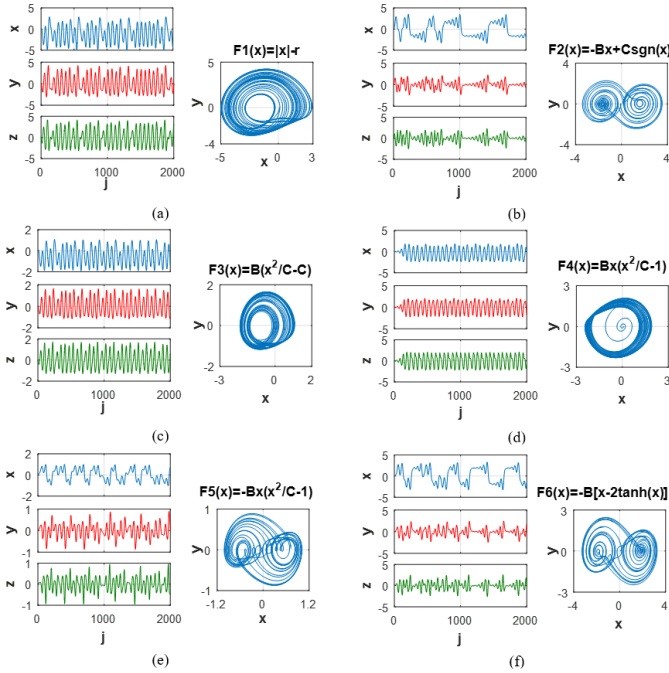


Figure 1 The numerical simulation results of the fractional-order Sprott's Jerk systems including the a) $F_1(x)$ function in Eq.2, b) $F_2(x)$ function in Eq.3, c) $F_3(x)$ function in Eq.4, d) $F_4(x)$ function in Eq.5, e) $F_5(x)$ function in Eq.6, and f) $F_6(x)$ function in Eq.7

THE APPLICATION OF THE PROPOSED METHOD TO THE SPROTT'S JERK SYSTEMS BY UTILIZING THE FPAF DEVICE

Although the time domain responses of the fractional-order nonlinear systems are observed with the G-L method in the numerical simulation studies, it is very hard to realize this method with the electronic hardware because of the requirement to storage of the previous calculations. Thus, the high order transfer function approximations of the fractional integration operator $1/s^q$ are able to be qualified as an alternative analyzing method for the hardware realizations of the fractional-order nonlinear systems. In the literature, these high order transfer functions are widely derived from the systematic methods such as the continued fraction expansion (CFE), Carlson, Oustaloup, Matsuda and Valsa (Khovanskii 1963; Carlson and Halijak 1964; Oustaloup *et al.* 2000; Matsuda and Fujii 1993; Valsa *et al.* 2011). These high order approximation transfer functions are framed in a limited frequency band and they are implemented with the combinations of the R-C, R-L or R-L-C pairs. However, it is preferred to use of the R-C networks for their implementation easiness, and there is also a tradeoff between simplicity of the implementation and frequency band in this method.

Additionally, as the order of the approximation function increases, the count of the employed passive components increases also, so an alternative method is introduced to overcome these problems in this study. In this proposed method, the fractional integrator operator is considered as a single parallel connected R-C pair in a limited frequency band with an acceptable error. This connection corresponds to a first order low pass filter (LPF) and the transfer function of this LPF is defined by the following equation:

$$H(s) = \frac{V_{out}(s)}{V_{in}(s)} = \frac{k_1}{s + k_2} \quad (12)$$

In Eq12, while ' k_1 ' is the zero of the LPF and its value is calculated by using the formula in Eq.13, ' k_2 ' is the pole of this LPF and its value is identified by the formula in Eq.14.

$$k_1 = w_{max}^{1-q} / \sin\left(\frac{q\pi}{2}\right) \quad (13)$$

$$k_2 = w_{max} / \tan\left(\frac{q\pi}{2}\right) \quad (14)$$

where while ' q ' is the fractional order of the nonlinear system, ' w_{max} ' is the radial frequency of the nonlinear system. The frequency response of a fractional-order integrator is shown in the bode diagram in Fig.2. In this figure, the black line represents an ideal fractional-order integrator for $q = 0.95$, the blue dotted line is plotted for the proposed LPF in Eq.12. The ' q ' and ' w_{max} ' parameters of this LPF are set to 0.95 and 100 rad/s, respectively. The value of the radial frequency is adjusted to this value arbitrarily similar to Ref (Ahmad and Sprott 2003). However, the proposed LPF closes to the ideal frequency response at this value.

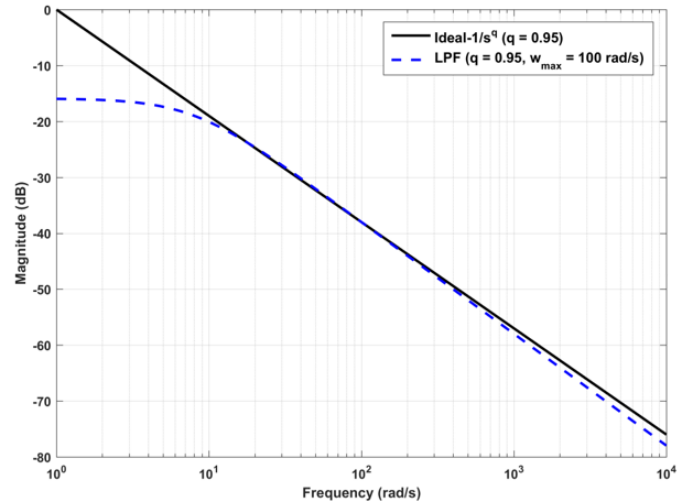


Figure 2 The bode diagram of an ideal fractional order system for $q = 0.95$ and the proposed LPF ($q = 0.95$ and $w_{max} = 100$ rad/s)

As mentioned in the introduction part, the circuit implementations of the fractional-order chaotic systems have impressive advantages, but the number of their hardware implementations is limited. Thus, here, an effective alternative design process has been suggested for realizing of the fractional-order chaotic systems with the electronic hardware in an easy way. In this introduced procedure, the LPF's characteristic in Eq.12 is adapted to the fractional-order nonlinear systems properly and this modified LPF structure can be used successfully instead of the fractional-order integrators in the in Eq.9. Thus, the hardware usage cost and

the circuit complexities have been decreased at the beginning of the hardware design process. To this end, after the Sprott's Jerk system is transported to the s-domain (the initial conditions are accepted as zero), its definition can be rewritten as in the following for adapting to the proposed LPF's characteristic:

$$\begin{aligned} X(s) &= [(Y(s) + k_2 X(s))(1/k_1)] \left[\frac{k_1}{(s+k_2)} \right] \\ Y(s) &= [(Z(s) + k_2 Y(s))(1/k_1)] \left[\frac{k_1}{(s+k_2)} \right] \\ Z(s) &= [(F(s) - pZ(s) - Y(s)) + k_2 Z(s)] \left[\frac{k_1}{(s+k_2)} \right] \end{aligned} \quad (15)$$

After these arrangements, a representative illustration of the obtained configuration is given in Fig. 3. In this figure, the LPFs should provide the characteristic in Eq. 12. Although the implementation issue of the fractional-order nonlinear system is solved with this design, the adjustment of the R-C pairs' values is hard to get the characteristic in Eq.12. Thus, the analog low pass filter designs and their realizations are carried out with the Field Programmable Analog Arrays (FPAAs) very sensitively by using the "BILINEAR FILTER" block in this device.

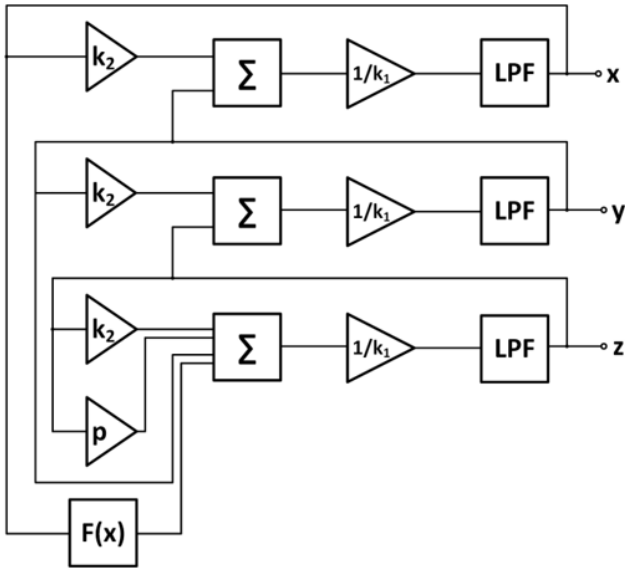



Figure 3 A representative illustration of the LPF in Eq. 12 based design of the fractional-order Sprott's Jerk system


The FPAAs device offers the flexible designing, the low time and equipment costs, programmability and reconfigurability properties and the rapid prototyping features by programming a matrix of the elements. These programmable elements are called Configurable Analog Blocks (CABs). The Configurable Analog Modules (CAMs) in the FPAAs device are built by using the switched-capacitor technology, so the predefined CAM block in the FPAAs can be programmed easily in order to get the desired configurations. The list of these CAM blocks and their functions are available in the ANADIGM DESIGNER™ tool. According to this tool the "BILIN-

EAR FILTER" CAM block () has the characteristic as in Eq. 16:

$$LPF(s) = \frac{V_{out}(s)}{V_{in}(s)} = \pm \frac{2\pi f_0 G}{s + 2\pi f_0} \quad (16)$$

where, 'G' is the adjustable gain value and 'f₀' is the corner frequency of this LPF. The characteristic of the "BILINEAR FILTER" CAM block in Eq.16 is very similar to the LPF in Eq.12 that is proposed to realize the fractional-order integrators. Therefore, the "BILINEAR FILTER" block can be used to implement the desired LPF in the FPAAs based realizations of the Sprott's Jerk systems. The remained mathematical descriptions in Eq.15 are also real-

ized by using the "SUM DIFF" () and the "TRANSFER

FUNCTION" () blocks. An example of the FPAAs based design scheme of the Sprott's Jerk system is given in Fig.4. In this figure, while the "SUM DIFF" block creates a half cycle summing/subtraction stage with up to four inputs, the "TRANSFER FUNCTION" block implements a user specified voltage transfer function with 256 quantization steps. The nonlinear functions in Table 1 have been embedded to the "TRANSFER FUNCTION" blocks in all designs. On the other hand, the FPAAs device has a saturation level (±2 V), so the studied model must be rescaled according to this saturation level. After these modifications, the coefficients of the Sprott's Jerk systems in Eq.15 have been rearranged and their final values are given in Table 2. The gain inputs of the "SUM DIFF" blocks have been set to these values. Additionally, the 'k₁' and 'k₂' parameters of the LPF are calculated as 1.2628 and 7.8702 respectively for q = 0.95 and ω_{max} = 100 rad/s.

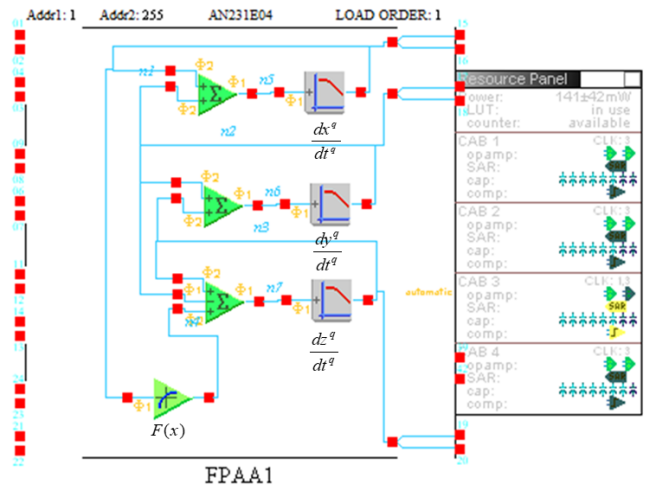


Figure 4 An example FPAAs design scheme of the fractional-order Sprott's Jerk system

After the similar configurations are completed in ANADIGM DESIGNER™ tool for all nonlinear functions in Table 1, the designed models are downloaded to the AN231E04 FPAAs board one by one via a serial interface by utilizing the FPAAs board's programmability and reconfigurability properties. The less power consumptions and the CAB usages are also seen in Fig. 4 and they are common in all realizations for the different nonlinear function based Sprott's Jerk system. Additionally, only a single FPAAs device has been used in these realizations in contrast to the available FPAAs based applications of the fractional-order chaotic systems in the literature (Petráš 2011). A photograph of the experimental setup is seen in Fig.5 and the obtained experimental realization results of the fractional-order Sprott's Jerk system are presented in Fig. 6. The time domain and the phase portraits' illustrations of

■ **Table 2** The ultimate definitions of the rearranged Sprott's Jerk systems and the nonlinear functions including in these systems for the FPAAs based implementations

The Nonlinear Functions-' $F(X(s))$ '	The rearranged Sprott's Jerk systems
$F_1(X(s)) = 1.25X(s) - 1$	$\begin{aligned} X(s) &= [0.1019Y(s) + 1.02X(s)]\left[\frac{1.2628}{(s+7.8702)}\right] \\ Y(s) &= [0.128Z(s) + 1.01Y(s)]\left[\frac{1.2628}{(s+7.8702)}\right] \\ Z(s) &= [0.118F_1(X(s)) + 0.891Z(s) - 0.128Y(s)]\left[\frac{1.2628}{(s+7.8702)}\right] \end{aligned} \quad (17)$
$F_2(X(s)) = -1.2X(s) + \text{sgn}(2X(s))$	$\begin{aligned} X(s) &= [0.128Y(s) + 1.01X(s)]\left[\frac{1.2628}{(s+7.8702)}\right] \\ Y(s) &= [0.128Z(s) + Y(s)]\left[\frac{1.2628}{(s+7.8702)}\right] \\ Z(s) &= [0.112F_2(X(s)) + 0.908Z(s) - 0.132Y(s)]\left[\frac{1.2628}{(s+7.8702)}\right] \end{aligned} \quad (18)$
$F_3(X(s)) = 0.58(X(s)^2 - 1)$	$\begin{aligned} X(s) &= [0.128Y(s) + X(s)]\left[\frac{1.2628}{(s+7.8702)}\right] \\ Y(s) &= [0.128Z(s) + Y(s)]\left[\frac{1.2628}{(s+7.8702)}\right] \\ Z(s) &= [0.256F_3(X(s)) + 0.921Z(s) - 0.128Y(s)]\left[\frac{1.2628}{(s+7.8702)}\right] \end{aligned} \quad (19)$
$F_4(X(s)) = 1.6X(s)(0.2X(s)^2 - 1)$	$\begin{aligned} X(s) &= [0.128Y(s) + X(s)]\left[\frac{1.2628}{(s+7.8702)}\right] \\ Y(s) &= [0.128Z(s) + Y(s)]\left[\frac{1.2628}{(s+7.8702)}\right] \\ Z(s) &= [0.268F_4(X(s)) + 0.924Z(s) - 0.128Y(s)]\left[\frac{1.2628}{(s+7.8702)}\right] \end{aligned} \quad (20)$
$F_5(X(s)) = -0.9X(s)(2.128X(s)^2 - 1)$	$\begin{aligned} X(s) &= [0.128Y(s) + 1.01X(s)]\left[\frac{1.2628}{(s+7.8702)}\right] \\ Y(s) &= [0.128Z(s) + 0.99Y(s)]\left[\frac{1.2628}{(s+7.8702)}\right] \\ Z(s) &= [3.19F_5(X(s)) + 0.89Z(s) - 0.128Y(s)]\left[\frac{1.2628}{(s+7.8702)}\right] \end{aligned} \quad (21)$
$F_6(X(s)) = -2.15[X(s) - \tanh(2X(s))]$	$\begin{aligned} X(s) &= [0.128Y(s) + X(s)]\left[\frac{1.2628}{(s+7.8702)}\right] \\ Y(s) &= [0.128Z(s) + Y(s)]\left[\frac{1.2628}{(s+7.8702)}\right] \\ Z(s) &= [0.256F_6(X(s)) + 0.924Z(s) - 0.128Y(s)]\left[\frac{1.2628}{(s+7.8702)}\right] \end{aligned} \quad (22)$

the fractional-order Sprott's Jerk system including the nonlinear functions in Eqs.2-7 have been given separately in Figs.6a-f, respectively. As seen from these figures, these experimental results agree well with the numerical simulation results in Fig.1. Therefore, the proposed LPF based implementations of the fractional-order systems are achieved with the FPAA based designs, successfully.

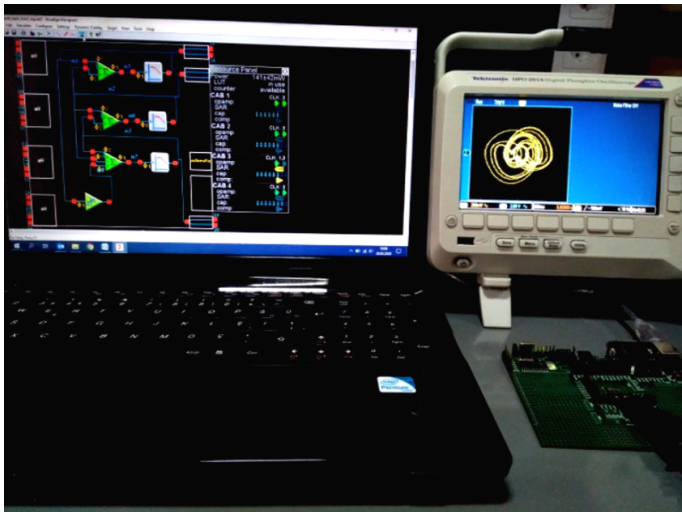


Figure 5 A photograph for the experimental setup of the FPAA based implementation of the fractional-order Sprott's Jerk system

DISCUSSION AND CONCLUSION

In this study, an effective and alternative design process has been introduced to implement the fractional-order chaotic systems with the electronic hardware. According to this procedure, the state variables of the fractional-order chaotic systems have been emulated by the modified first order low-pass filters (LPF), so the hardware usage costs and the circuit complexities have been decreased at the beginning of the hardware design process. Thus, the introduced method has been tested on the fractional-order Sprott's Jerk systems and these systems have been implemented with a programmable analog device.

In this context, firstly, the minimum fractional-orders of the state variables of the Sprott's Jerk systems have been calculated by considering the stability of the fractional-order nonlinear systems and the calculation of the minimum fractional-order has been exemplified in detail for a nonlinear function. After a common fractional order was identified for all nonlinear functions of the Sprott's Jerk system, these fractional-order systems have been simulated for $q = 0.95$ by employing the G-L fractional derivative method. Thus, both the fractional derivative concepts have been handled and the results of the stability analyses have been verified by the G-L fractional derivative method. After the identification of the fractional order for the Sprott's Jerk system, the modified first order low-pass filters (LPFs), which emulate the state variables of the fractional-order chaotic systems, have been dealt with in detail. The most important arguments about this LPF structure are listed as following: i) the modified LPF structure has been characterized by depending on the changes of the fractional order and the radial frequency, ii) the desired fractional-order integrator has been built by using this LPF, iii) the adjustment of the discrete devices' values is hard to get the characteristic of the proposed LPF. On the other hand, since the identification of the "BILINEAR FILTER"

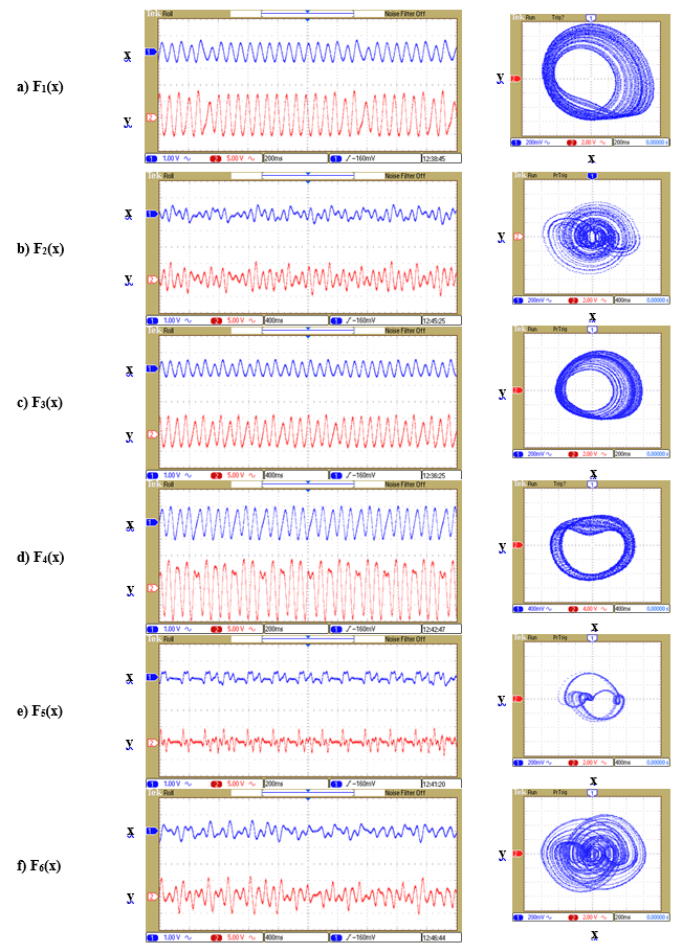


Figure 6 The time domain and the phase portraits illustrations of the fractional-order Sprott's Jerk system including the a) $F_1(x)$ function in Eq.2, b) $F_2(x)$ function in Eq.3, c) $F_3(x)$ function in Eq.4, d) $F_4(x)$ function in Eq.5, e) $F_5(x)$ function in Eq.6, and f) $F_6(x)$ function in Eq.7

CAM block in the FPAA device is very similar to the proposed LPF structure's one, this CAM block has been used as a fractional-order integrator emulator in this study, successfully. Therefore, the fractional-order Sprott's Jerk system has been implemented by using the FPAA devices in order to prove the effectiveness of the LPF-based approximation for the fractional-order integrators. Additionally, the fractional-order Sprott's Jerk systems including the different nonlinear functions have been realized with a programmable analog device, namely FPAA. Moreover, the proposed LPF characteristic can be employed as a fractional-order integrator in the various research fields, where the desired frequency band is limited.

Conflicts of interest

The authors declare that there is no conflict of interest regarding the publication of this paper.

Availability of data and material

Not applicable.

LITERATURE CITED

- 1999 Chapter 7 - numerical evaluation of fractional derivatives. In *Fractional Differential Equations*, edited by I. Podlubny, volume 198 of *Mathematics in Science and Engineering*, pp. 199–221, Elsevier.
- Ahmad, W., R. El-Khazali, and A. Elwakil, 2001 Fractional-order Wien-bridge oscillator. *Electronics Letters* **37**: 1110–1112.
- Ahmad, W. M. and J. C. Sprott, 2003 Chaos in fractional-order autonomous nonlinear systems. *Chaos, Solitons & Fractals* **16**: 339–351.
- Arena, P., 2000 *Nonlinear noninteger order circuits and systems: an introduction*, volume 38. World Scientific.
- Atangana, A. and B. S. T. Alkahtani, 2015 Extension of the resistance, inductance, capacitance electrical circuit to fractional derivative without singular kernel. *Advances in Mechanical Engineering* **7**: 1687814015591937.
- Azar, A. T., A. G. Radwan, and S. Vaidyanathan, 2018 *Mathematical Techniques of Fractional Order Systems*. Elsevier.
- Caponetto, R., 2010 *Fractional order systems: modeling and control applications*, volume 72. World Scientific.
- Carlson, G. and C. Halijak, 1964 Approximation of fractional capacitors $(1/s)^{\alpha}$ by a regular Newton process. *IEEE Transactions on Circuit Theory* **11**: 210–213.
- Charef, A., 2006 Analogue realisation of fractional-order integrator, differentiator and fractional π - λ - μ controller. *IEE Proceedings-Control Theory and Applications* **153**: 714–720.
- Chen, G. and T. Ueta, 2002 *Chaos in circuits and systems* world scientific.
- Chen, L., W. Pan, R. Wu, K. Wang, and Y. He, 2016 Generation and circuit implementation of fractional-order multi-scroll attractors. *Chaos, Solitons & Fractals* **85**: 22–31.
- Chen, Y. Q. and K. L. Moore, 2002 Discretization schemes for fractional-order differentiators and integrators. *IEEE Transactions on Circuits and Systems I: Fundamental Theory and Applications* **49**: 363–367.
- Deniz, F. N., A. Yüce, and N. Tan, 2019 Tuning of PI-PD controller based on standard forms for fractional order systems. *Journal of Applied Nonlinear Dynamics* **8**: 5–21.
- Elwakil, A. S., 2010 Fractional-order circuits and systems: An emerging interdisciplinary research area. *IEEE Circuits and Systems Magazine* **10**: 40–50.
- Gómez, F., J. Rosales, and M. Guía, 2013 RLC electrical circuit of non-integer order. *Open Physics* **11**: 1361–1365.
- Gómez-Aguilar, J. F., A. Atangana, and V. F. Morales-Delgado, 2017 Electrical circuits RC, LC, and RL described by Atangana-Baleanu fractional derivatives. *International Journal of Circuit Theory and Applications* **45**: 1514–1533.
- Gottlieb, H., 1996 Question #38. What is the simplest jerk function that gives chaos? *American Journal of Physics* **64**: 525–525.
- Khovanskii, A. N., 1963 *The application of continued fractions and their generalizations to problems in approximation theory*. Noordhoff Groningen.
- Kılıç, R., 2010 *A practical guide for studying Chua's circuits*, volume 71. World Scientific.
- Krishna, B. and K. Reddy, 2008 Active and passive realization of fractance device of order 1/2. *Active and passive electronic components* **2008**.
- Krishna, B. T., 2011 Studies on fractional order differentiators and integrators: A survey. *Signal processing* **91**: 386–426.
- Matsuda, K. and H. Fujii, 1993 H (infinity) optimized wave-absorbing control-analytical and experimental results. *Journal of Guidance, Control, and Dynamics* **16**: 1146–1153.
- Maundy, B., A. Elwakil, and S. Gift, 2012 On the realization of multiphase oscillators using fractional-order allpass filters. *Circuits, Systems, and Signal Processing* **31**: 3–17.
- Oldham, K. and J. Spanier, 1974 *The fractional calculus theory and applications of differentiation and integration to arbitrary order*. Elsevier.
- Oustaloup, A., F. Levron, B. Mathieu, and F. M. Nanot, 2000 Frequency-band complex noninteger differentiator: characterization and synthesis. *IEEE Transactions on Circuits and Systems I: Fundamental Theory and Applications* **47**: 25–39.
- Öztürk, I. and R. Kılıç, 2019 Higher dimensional baker map and its digital implementation with LSB-extension method. *IEEE Transactions on Circuits and Systems I: Regular Papers* **66**: 4780–4792.
- Petráš, I., 2011 *Fractional-order nonlinear systems: modeling, analysis and simulation*. Springer Science & Business Media.
- Radwan, A. G., A. S. Elwakil, and A. M. Soliman, 2008 Fractional-order sinusoidal oscillators: design procedure and practical examples. *IEEE Transactions on Circuits and Systems I: Regular Papers* **55**: 2051–2063.
- Radwan, A. G., A. S. Elwakil, and A. M. Soliman, 2009 On the generalization of second-order filters to the fractional-order domain. *Journal of Circuits, Systems, and Computers* **18**: 361–386.
- Radwan, A. G. and K. N. Salama, 2012 Fractional-order RC and RL circuits. *Circuits, Systems, and Signal Processing* **31**: 1901–1915.
- Sacu, I. E. and M. Alci, 2019 A current mode design of fractional order universal filter. *Advances in Electrical and Computer Engineering* **19**: 71–78.
- Singh, N., U. Mehta, K. Kothari, and M. Cirrincione, 2020 Optimized fractional low and highpass filters of $(1+\alpha)$ order on FPGA. *Bulletin of the Polish Academy of Sciences. Technical Sciences* **68**.
- Sprott, J., 1997 Some simple chaotic jerk functions. *American Journal of Physics* **65**: 537–543.
- Sprott, J. C., 1994 Some simple chaotic flows. *Physical Review E* **50**: R647.
- Sprott, J. C., 2000a A new class of chaotic circuit. *Physics Letters A* **266**: 19–23.
- Sprott, J. C., 2000b Simple chaotic systems and circuits. *American Journal of Physics* **68**: 758–763.
- Stöckmann, H.-J., 1999 *Quantum Chaos: An Introduction*. Cambridge University Press.
- Tavazoei, M. S. and M. Haeri, 2007 A necessary condition for double scroll attractor existence in fractional-order systems. *Physics Letters A* **367**: 102–113.
- Tavazoei, M. S. and M. Haeri, 2008 Chaotic attractors in incommensurate fractional order systems. *Physica D: Nonlinear Phenomena* **237**: 2628–2637.
- Tlelo-Cuautle, E., A. D. Pano-Azucena, O. Guillén-Fernández, and A. Silva-Juárez, 2020 *Analog/digital implementation of fractional order chaotic circuits and applications*. Springer.
- Valsa, J., P. Dvorak, and M. Friedl, 2011 Network model of the CPE. *Radioengineering* **20**: 619–626.

How to cite this article: Korkmaz, N., and Sacu, I. E. An efficient design procedure to implement the fractional-order chaotic jerk systems with the programmable analog platform. *Chaos Theory and Applications*, 3(2), 59–66, 2021.

An Analysis of Power System Stability against Hyperchaotic Noises and Blackouts

Hakan Öztürk ^{α,*,1}

^αElectrical and Electronic Engineering, Faculty of Engineering and Natural Sciences, Istanbul Medeniyet University, Istanbul, Turkey, ^{*}Electrical and Electronics Engineering, Institute of Natural Sciences, Sakarya University, Sakarya, Turkey.

ABSTRACT This study investigates the power systems that involve various numbers of busbars. To prevent the disturbances and instabilities in the power systems, power system stabilizers and various control methods have been used. A hyperchaotic blackout has been created by using an existing hyperchaotic system. Hyperchaotic voltage collapse and hyperchaotic disturbance have been injected to the test systems. The situations of the various power systems are illustrated under proposed hyperchaotic blackout and noise. The stability analysis of the power system has been executed according to the dynamic features of hyperchaos.

KEYWORDS

Chaos theory
Hyperchaos
Power system stability
Power flow
Blackouts

INTRODUCTION

Power System Stabilizers (PSS) are used to damp low-frequency oscillations in the range of 0.2 Hz to 2.5 Hz. The automatic voltage regulator (AVR) improves the terminal voltage of the generator by controlling the amount of current supplied from the exciter to the generator field winding. Thus, the generator excitation system maintains generator voltage and controls the reactive power flow using an automatic voltage regulator. It is mainly used to dampen oscillations that occur during load changes in the power system. It keeps the generator terminal voltage constant, so that the voltage on the load side remains almost constant even if the load changes with time. Therefore, the stability of the AVR system would seriously affect the security of the power system. AVR helps to improve the steady-state stability of power systems, but transient stability has become a problem for power system operators. To improve system damping, the generator is equipped with a PSS, which provides an additional feedback stabilization signal in the excitation system (DELAVARI and BAYAT 2015; Demello and Concordia 1969; Sauer and Pai 1998).

In the literature, large number of studies about the hyperchaos that has been recently discovered exist. (Rossler 1979) first introduced the hyperchaotic systems and has enabled it to be used in many studies such as this study. Various analyses were executed about the hyperchaos in the papers such as (Matsumoto *et al.* 1986;

Wang and Wang 2008; Li and Chen 2004; Li *et al.* 2005; Fozin Fozin *et al.* 2019; Rössler and Letellier 2020; Vaidyanathan *et al.* 2020; Rech 2017) It is possible to reach hyperchaotic systems in many fields such as control theory (Fozin Fozin *et al.* 2019), synchronization (Sajjadi *et al.* 2020; Tian *et al.* 2019), secure communication applications (Yu *et al.* 2019; Xiu *et al.* 2021) and image encryption (Yuan *et al.* 2017; Liu *et al.* 2019; Zhu and Zhu 2020). The corresponding topic of this study is power system stability. The recent state of its literature can be summarized by mentioning the following studies that optimizing the parameters of power systems (Huang *et al.* 2017; Ahsan and Mufti 2020). The studies that improve the power system stability by proposing a novel whale optimization algorithm (Kumar *et al.* 2021; Sahu *et al.* 2018), energy reshaping (Dong *et al.* 2017), FACTS devices (Singh and Agnihotri 2018; Van Dai *et al.* 2017), UPFC Based on Neuro-Fuzzy Method (Jamal *et al.* 2017) and wide area fuzzy-2 logic based damping controller Sharma *et al.* (2017) exist. The most of analyses about the power system stability aim to enhance the stability of the test system by proposing novel control methods. However, relating analyses have been executed under ordinary faults that have short time and are linear.

The chaos in power systems is basically investigated in (Yu *et al.* 2003; Chiang *et al.* 1993) in the simple power systems. Amongst the studies that includes chaos with power systems, Chen *et al.* (2005) presented the bifurcation in a SMIB system. (Harb and Abdel-Jabbar 2003) controlled bifurcation in a small power system. Nangrani and Bhat (2018) proposed a fractional order controller, and Das *et al.* (2021) proposed a PID Sliding Mode Controller for chaotic power systems. Previous studies have not elaborated the analyze of power systems and have not comprised sufficient benchmark. This study aims to make a more detailed analysis on the topic, and present a superior hyperchaotic situation.

Manuscript received: 29 July 2021,
Revised: 7 September 2021,
Accepted: 10 September 2021.

¹ hakan.ozturk.eee@gmail.com, hakan.ozturk@medeniyet.edu.tr (Corresponding Author)

This study basically recounts the corresponding power system stabilizers in Section 2. The hyperchaotic system and how it is considered as a blackout are shown in Section 3. The hyperchaotic blackout is introduced in the test systems such as two-area model, Heffron-Philips model that involve infinite bus, single machine infinite bus system in Section 4. The detailed stability analysis has been made in section 5. Finally, the conclusions in the study have been presented in Section 6.

THE POWER SYSTEM STABILIZERS

The power system stabilizers have been used to add damping to electromechanical oscillations and optimize the system. They operate basically the production of electrical torque proportional to the speed change through the generator's excitation system. The PSS is one of the supplementary controllers, which is often applied as part of the excitation control system. Grid codes and regulatory agencies are increasingly specifying PSS controls for new generation and retrofit on existing units. In the excitation system, PSS applies a signal creating electrical torques that damp out power oscillations and it is the main function of the PSS. The transfer function of the PSS (Ekinici and Hekimoglu 2018) is simply given as Eq. 1.

$$V(s) = K_{PSS} \left(\frac{1 + sT_1}{1 + sT_2} \right) \Delta\omega(s) \quad (1)$$

The PSS response control, part of the integrated generator control system, provides an additional signal that can be added to the Automatic Voltage Regulator (AVR) input. By adding the stabilization signal, the PSS should generate an electrical torque component that counteracts the mechanical dynamics. The electrical torque component generated should be in phase with the generator rotor speed deviations to be able to damp the oscillations. The main structure of PSS has been shown as Figure. 1 and it has been used widely.

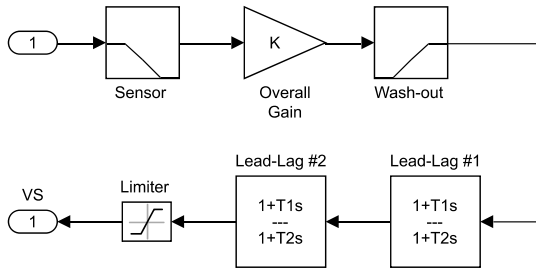


Figure 1 Block Diagram of PSS

The generic configuration of the PSS in a power system is depicted in Fig. 2. The PSS is not usually utilized as alone. In the power systems, various control models and devices have been accompanied the PSS. The AVR is the primary of these devices. Flexible alternating current transmission system (FACTS), static VAR compensator (SVC) and thyristor-switched reactor (TSR) are amongst the mentioned devices.

Additionally, numerous control methods such as decentralized modal control, fuzzy logic control, PID control and adaptive fuzzy sliding mode control have been developed. Hybrid methods are also proposed in terms of accordance and robustness. These methods are also improved with metaheuristic optimization algorithms. Hence, power system stability has been aimed to improve by means of the corresponding methods.

DESIGN OF THE POWER SYSTEM BASED ON HYPER-CHAOS

The generic control model of PSS and AVR is seen in Figure 2. In the control system, the reference is generally taken as 1 pu. The PSS has used the rotor speed deviation of the generator. Automatic voltage regulator (AVR) regulates the excitation voltage of the exciter.

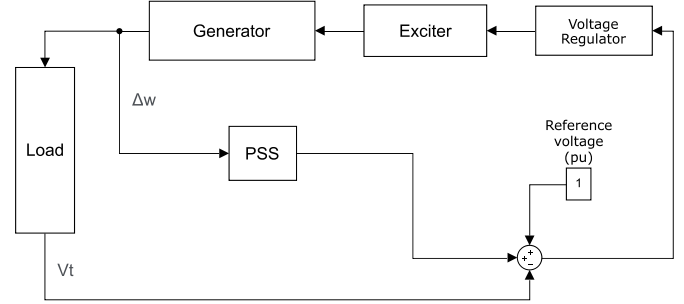


Figure 2 Conventional power system model

The generic equations of the power system models have been listed in Eq. 2 - 6. In Eq. 2, $\Delta w(t)$ represents the speed deviation, is loaded by hyperchaotic oscillator. In Eq. 6, reference voltage is consisted of a set of equations that given in Eq. 7 - 10.

$$w(t) = w_0 + \Delta w(t) \quad (2)$$

$$\Delta w(t) = \frac{1}{2H} \int_0^t (T_m - T_e) dt - K_d \Delta w(t) \quad (3)$$

$$\frac{d\delta_i}{dt} = w_i - w_{ref} \quad (4)$$

$$\frac{dw_i}{dt} = \frac{(-D_i(w_i - w_{ref}) + P_{mi} - P_{Gi})}{M_i} \quad (5)$$

$$\frac{dE_{fd}}{dt} = (-E_{fd} + K_a(V_{ref} + V_s - V)) / T_a \quad (6)$$

Where the $w(t)$ is the speed or frequency, H is inertia constant that is inversely proportional to noise, nomenclature T is the reciprocating torques, K_d is damping coefficient, δ is load angle, D is damping factor, P_{mi} is real power generated, M is angular torque, P_{Gi} is output electrical power of the generator, E_{fd} is field voltage, V_s is terminal voltage, K_a is gain of the excitation system, Eq. 2 - 6 are basic equations of power systems.

The PSS is implemented in power systems and is investigated under various faults and disturbances. Reference voltage indicates that the type of disturbance and fault. The reference voltage is replaced by an oscillator that is obtained from well-known Rossler attractor (Rossler 1979) as follows:

$$\dot{V}_{ref1} = -(V_{ref2} + V_{ref3}) \quad (7)$$

$$\dot{V}_{ref2} = V_{ref1} + \alpha V_{ref2} + V_{ref4} \quad (8)$$

$$\dot{V}_{ref3} = b + V_{ref1} V_{ref3} \quad (9)$$

$$\dot{V}_{ref4} = -c V_{ref3} + d V_{ref4} \quad (10)$$

Reference voltages are given to the test system where $\alpha = 0.25$, $b=3$, $c=-0.5$ and $d=0.05$. The initial conditions are set as $V_{ref1}(0) = -10$, $V_{ref2}(0) = -6$, $V_{ref3}(0) = 0$ and $V_{ref4}(0) = 10.1$. Each generator is supplied by hyperchaotic oscillator voltage instead of normal reference voltage.

As a signal of noise, $\Delta w(t)$ is similarly replaced by the equations of well-known Rossler attractor. Equation model of the power system is basically transformed into follows:

$$w_1(t) = w_0 - \int (\Delta w_2 + \Delta w_3) dt \quad (11)$$

$$w_2(t) = w_0 + \int (\Delta w_1 + \alpha \Delta w_2 + \Delta w_4) dt \quad (12)$$

$$w_3(t) = w_0 + \int (b + \Delta w_1 \Delta w_3) dt \quad (13)$$

$$w_4(t) = w_0 + \int (-c \Delta w_3 + d \Delta w_4) dt \quad (14)$$

$$\Delta w(t) = \frac{1}{2H} \int_0^t (T_m - T_e) dt + K_d \int (\Delta w_2 + \Delta w_3) dt \quad (15)$$

PROPOSED HYPERCHAOTIC BLACKOUT FOR THE CASES

Case 1 : 11 Buses and 4 machines system

This system consists of two largely symmetrical areas connected by two 230 kV lines twice 110 km long. Each has two identical rotary generators with a rated power of 20 kV/900 MVA. The parameters of the synchronous machines are all the same except for the inertia, which is $H=6.5s$ for the area 1 machines and $H=4s$ for the area 2 machines. The load flow in this case (with generator 2 as the slack machine) is such that all generators in the system produce about 700 MW each. The loads are assumed to be constant impedance load models throughout, with the loads for Area 1 and 2 being 976 MW and 1765 MW respectively. To improve the voltage profile, capacitors were added in each area, can be seen in Figure 3.

This system is also referred as Kundur's two-area system and its features can be summarized as follows:

- Two loads are comprised to the test system at bus 7 and 9;
- Both areas have been provided with the fundamental frequency 60 Hz;
- Two shunt capacitors are connected to bus 7 and 9;
- The system is consisted two similar areas connected by a transmission line.;

Each generators of the system (G1, G2, G3, G4) in Figure 3 have been connected with the 4-D hyperchaotic system (Sheikh and Starrett 2015). The other parameters are not changed and power system stabilizers are activated taking into account the cases.

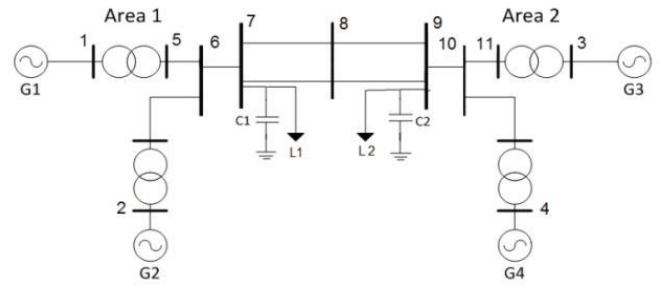


Figure 3 Four machines or two-area test system (Sheikh and Starrett 2015)

Case 2 : Infinite Bus Power System

Heffron-Phillips model of the synchronous generator is a fourth-order linear model with a third-order synchronous machine and a first-order AVR. This model is suitable for the analysis of small signals where a linear approximation is reasonable. Therefore, all input and output signals of this model have variations with a small range around the nominal value represented by nomenclature "Delta". The block diagram of the linear model is shown in Figure 4.

- Heffron-Phillips model is widely studied in small signal stability analysis, also for off-line design of power system stabilizers;
- The parameters are mostly processed using the parameters of synchronous generator and system variables at steady-state conditions;
- The model can be modified according to proposed control algorithm.

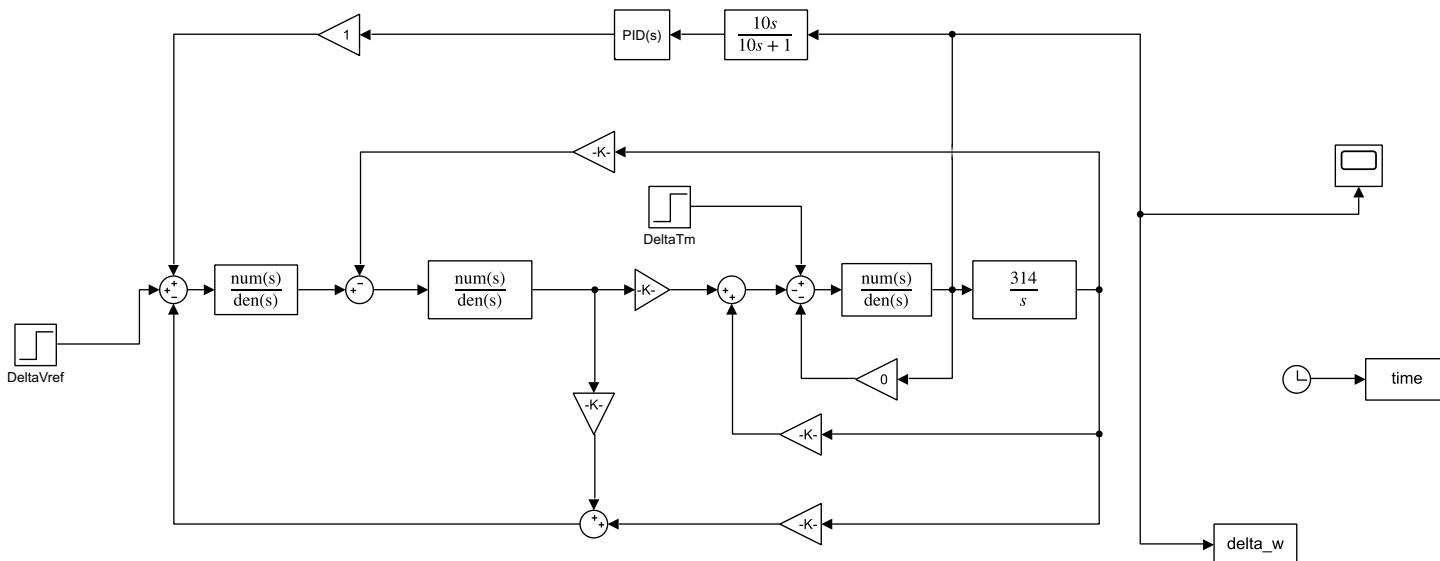


Figure 4 The Heffron-Phillips Model that involve infinite bus

Case 3 : SMIB system

Single machine-infinite bus system (SMIB) is a basic system that is consisted of a generator, a transformer, the transmission line, a source, high impedance and infinite bus as Fig. 5. In this study line reactance is taken as 100 ohm and 1000 VA synchronous machine is selected. The main features of the test systems are denoted in Table 1. The excitation voltage of the machine is connected with hyperchaotic oscillator. It is aimed to consider under single phase-hyperchaotic blackout.

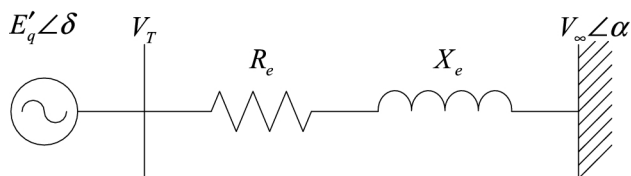


Figure 5 SMIB system model

STABILITY FINDINGS FOR THE CASES

Stability refers to a power system's tendency to create restorative forces that are equal to or larger than the disturbing forces in order to preserve equilibrium. Problems with power system stability are often classified into two categories: steady state and transient. The ability of the power system to reestablish synchronism after modest or slow shocks, such as a gradual power change, is referred to as steady-state stability. Dynamic stability is a subset of steady-state stability. With the addition of automatic control mechanisms, dynamic stability is concerned with tiny disruptions enduring for a long time. Transient stability is concerned with the impacts of large, sudden disruptions such as fault onset, line loss, and load application or removal.

Results for Case 1

The mentioned tests for the cases have been realized in Matlab Environment. The results of the test for two areas system have been depicted in Figs. 6-11. The corresponding results are obtained from the system that is injected with hyperchaotic voltage. Accordingly, the balance of the speed deviation is not overly disturbed as it can be seen in Fig. 6. In the generator voltages and load angle, the oscillations that instantaneously increase with some time intervals are occurred as Figs. 7-8. Once PSS restorer is activated, the case can be seen in Figs. 10-11. The power system stabilizers have increased the magnitude of violent voltage swells and had a negative impact. The power system stabilizers have caused to worsen small signal stability, too.

For voltage stability evaluation, PV curve is obtained as Fig. 12. In the first state, there is no points under the saddle point and the system is stable. In Fig. 13 tornado type curve obtained instead of nose curve as Power-Voltage characteristic has been shown. The power-voltage characteristic in hyperchaotic blackout has included large number of noses. It indicates that many critical eigen values are found in power system.

■ **Table 1 Standart values for the test systems**

Test Model	Speed Deviation	Voltage (V)	Frequency (Hz)	Power (VA)
Two-area system	0.0024 pu	20 kV	60 Hz	900 MVA
Infinite bus power system	0 rad/s	400 V	60 Hz	-
SMIB system	-0.0013 rad/s	220 V	60 Hz	1 kVA

■ **Table 2 Noise characteristics of power systems for the cases**

Test Type/Model	Speed deviation			
	Hyperchaotic Blackout		Damping Characteristic	
	Mean Value	Maximum Value	Mean Value	Maximum Value
Two-area system (G1)	0.0509 pu	0.1769 pu	0.02765 pu	0.1164 pu
Two-area system (G2)	0.0520 pu	0.1816 pu	0.02836 pu	0.1181 pu
Two-area system (G3)	0.3277 pu	0.4977 pu	0.2466 pu	0.4265 pu
Two-area system (G4)	0.3034 pu	0.4671 pu	0.2456 pu	0.4234 pu
Infinite bus system	0.0007 rad/s	0.2342 rad/s	0.0007 rad/s	0.169 rad/s
SMIB system	-0.7211 rad/s	512 rad/s	-0.6891 rad/s	128 rad/s

■ **Table 3 Frequency stability of two-area system**

Test Type/Model	Frequency (Hz)			
	Hyperchaotic Blackout		Damping Characteristic	
	Mean Value	Maximum Value	Mean Value	Maximum Value
Two-area system (G1)	60 Hz	60.75 Hz	60 Hz	60.72 Hz
Two-area system (G2)	60.06 Hz	61.29 Hz	60.04 Hz	61 Hz
Two-area system (G3)	61.28 Hz	80.54 Hz	62.10 Hz	82.65 Hz
Two-area system (G4)	61.88 Hz	83.65 Hz	62.07 Hz	81.75 Hz

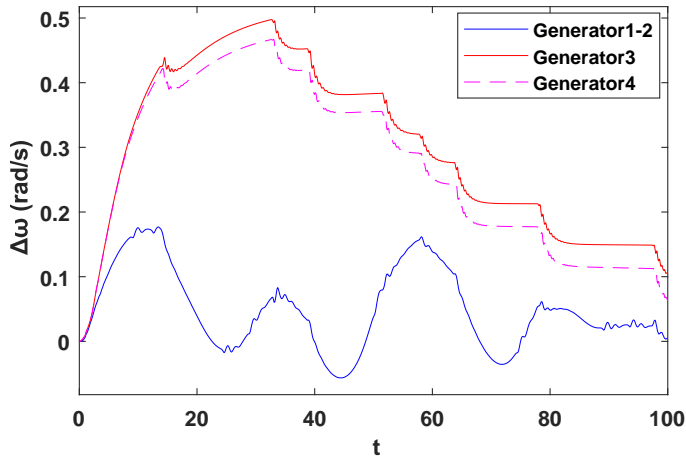


Figure 6 Speed deviation of generators against hyperchaotic noise

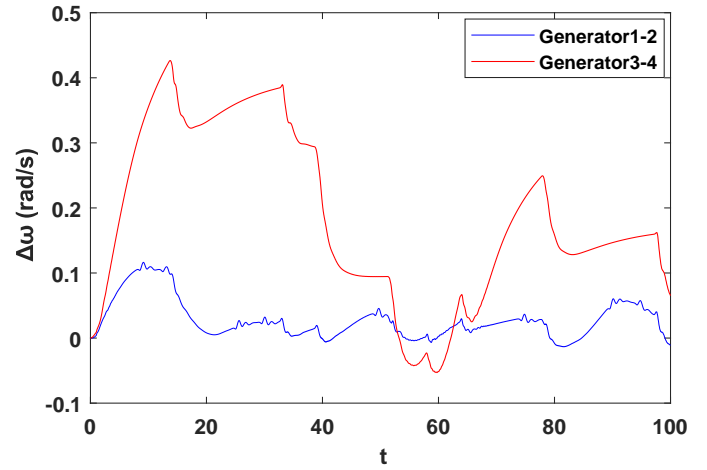


Figure 9 Speed deviation of generators against hyperchaotic noise when PSS is activated

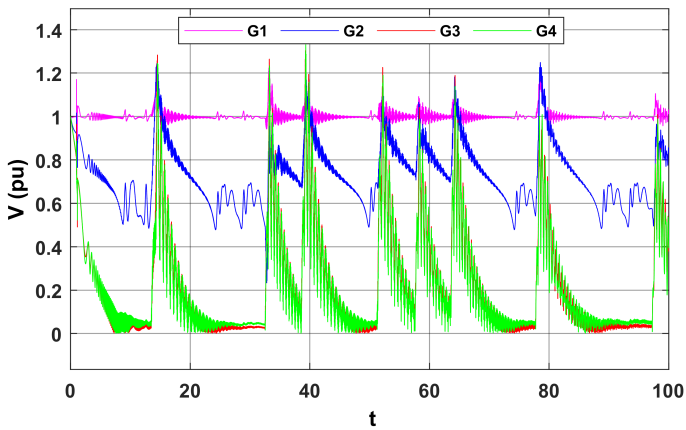


Figure 7 Generator voltages against hyperchaotic noise

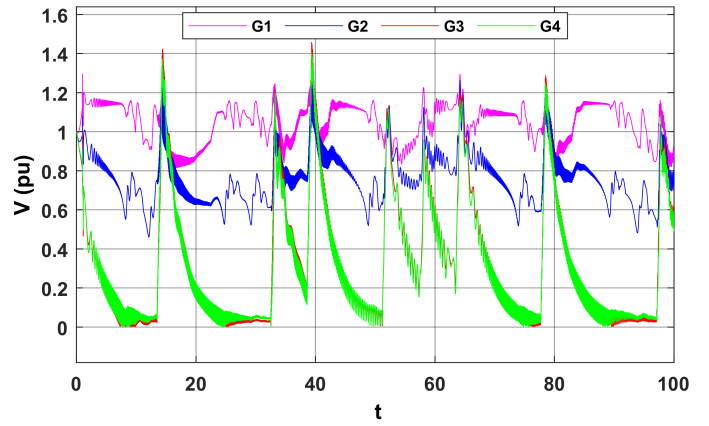


Figure 10 Generator voltages against hyperchaotic noise when PSS is activated

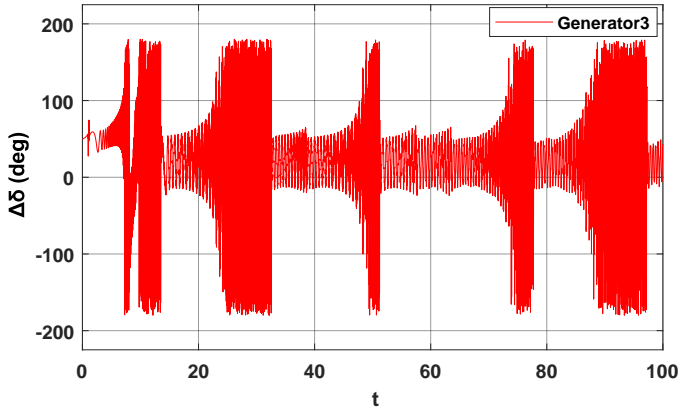


Figure 8 Load angle of generator 3 against hyperchaotic noise

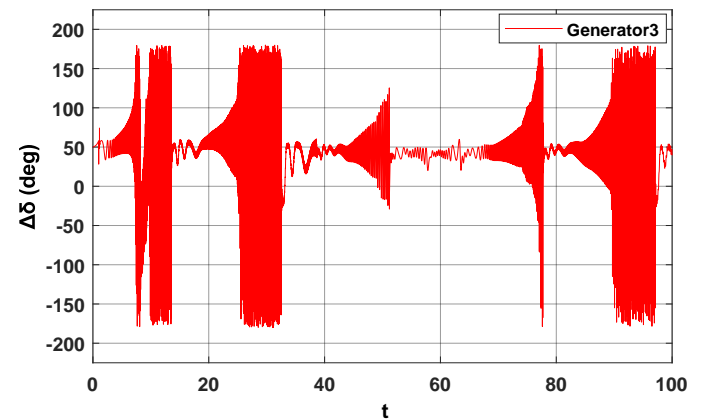


Figure 11 Load angle of generator 3 against hyperchaotic noise when PSS is activated

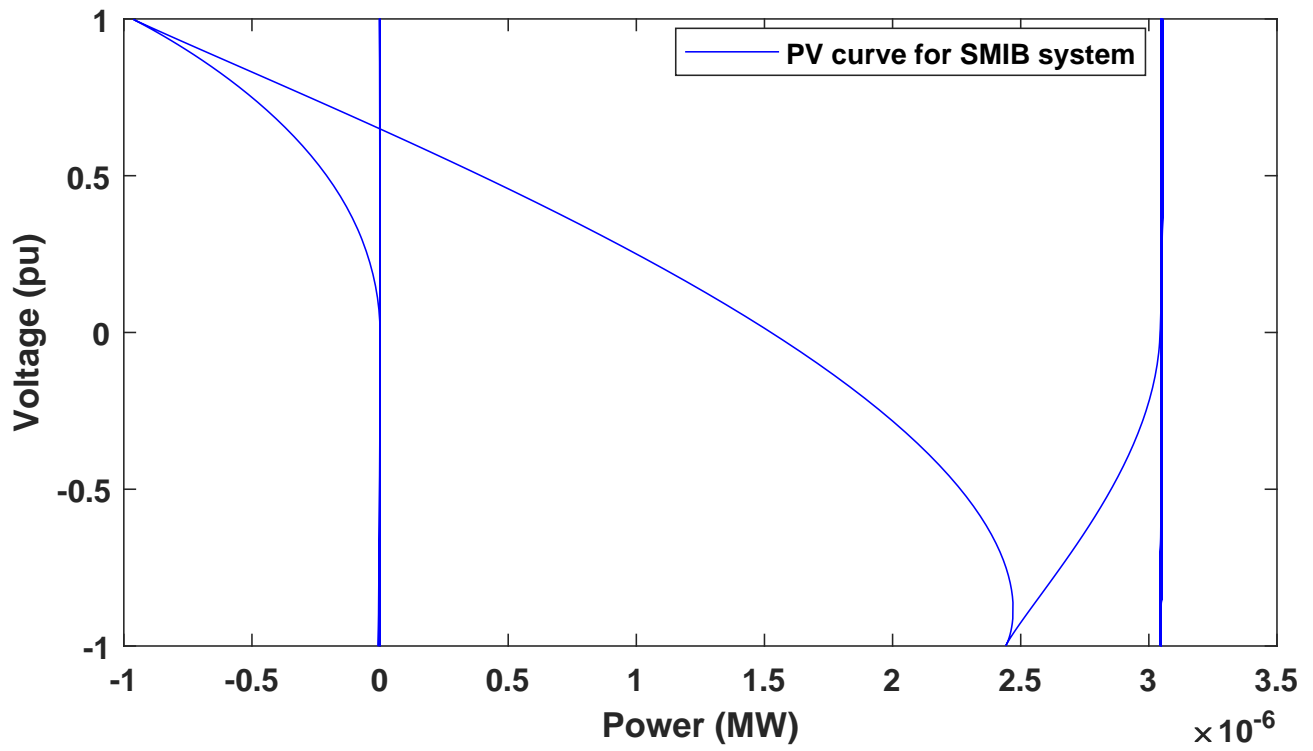


Figure 12 The standart P-V curve (Nose curve) for SMIB system

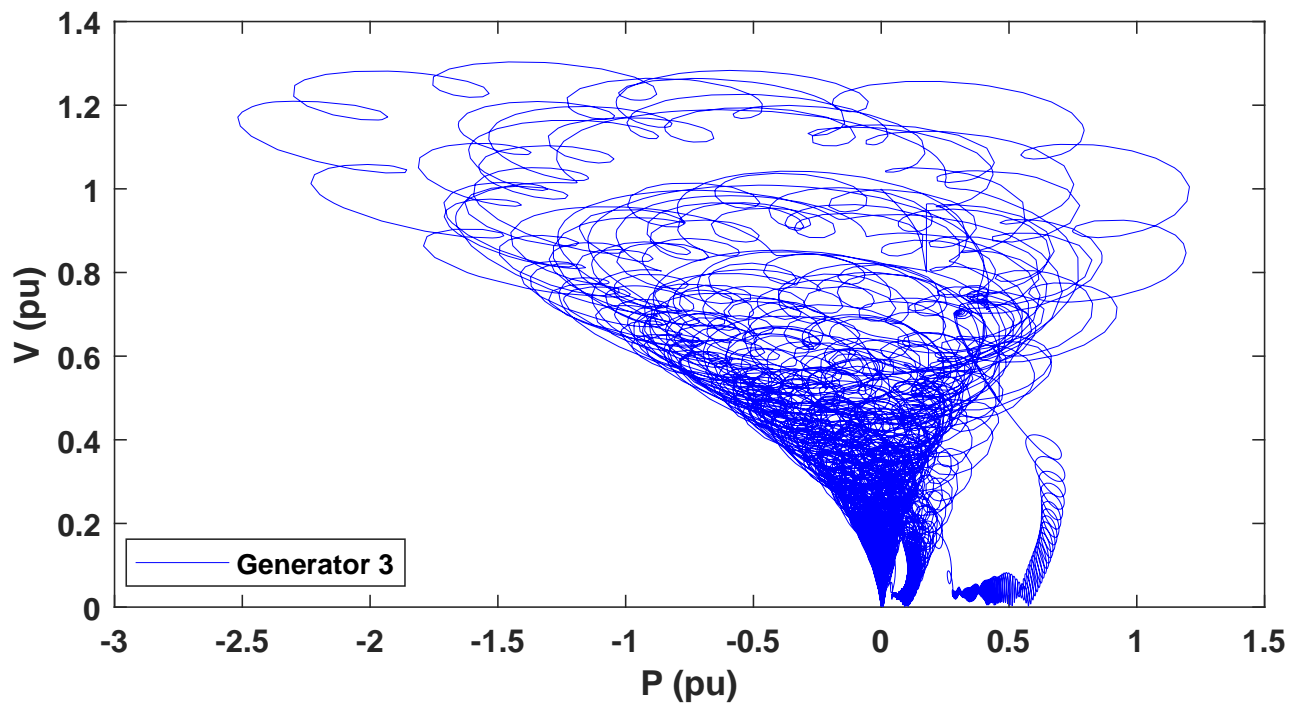


Figure 13 P-V curve during hyperchaotic blackout

According to the results in Table 2, the stability of generator 3 and generator 4 have been more reduced than that of generator 1 and generator 2. PSS could not be very effective for them. The frequency values for the cases have been given in Table 3. In two-area system, generator 1 and generator 2 have been bordered on stability. In generator 3 and generator 4, very high frequency instability occurred. The PSS has not been very advantageous for the devastating blackouts.

Results for Case 2

In the second case, infinite-bus model is used to analyze hyperchaotic blackout characteristics. The generators showed more oscillations than that of standart noises. Unlike standart noises in power systems, very small and ineque oscillations have been observed. The PID controlled PSS have filtered the small noises in the generators. It can be seen by the variety between the Fig. 14 and Fig. 15. However, high magnituded noises could not be prevented.

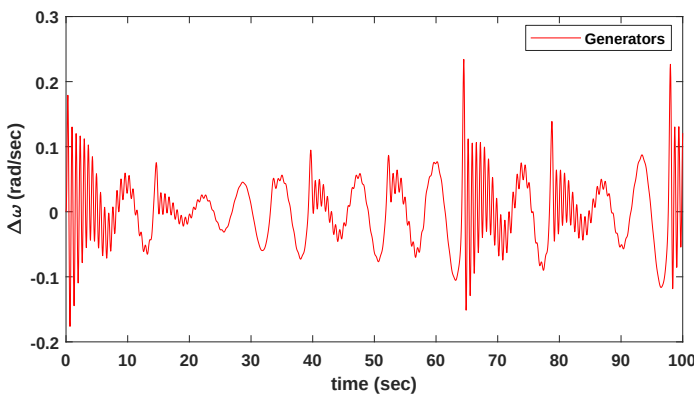


Figure 14 Speed deviation of generators against hyperchaotic noise in infinite bus power system

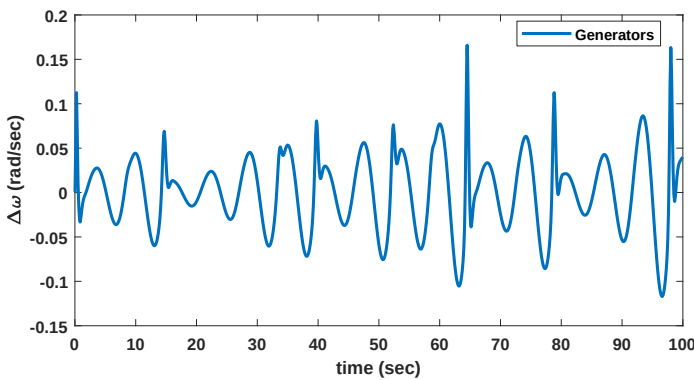


Figure 15 Speed deviation of generators against hyperchaotic noise with PID controlled PSS in infinite bus power system

Results for Case 3

The third case is realized with the single synchronous machine under load. The corresponding power curves have been investigated in depth. The assesment on the tests have been realized in terms of noise damping and power quality improvement.

The speed deviation curves according to the cases are given in Fig. 16. In line with various tests, it is found that hyperchaotic

blackouts have not caused to occur more oscillations in SMIB system. But it overly increased the peak value of the speed deviation as Table 2 and it reversed the direction of the oscillations in the speed deviations. The PSS rarely had a negative effect on counteracting the hyperchaotic blackout. The PSS sometimes increased the occurrence and magnitude of oscillations in speed deviation.

Electrical power in the SMIB system under hyperchaotic blackout is shown in Fig. 17. The PSS has been damped noises and improved power quality as it can be seen in Fig 18. However, the instabilities in power could not be filtered completely. In both cases, standard power of the power system has been run out in terms of steady state stability.

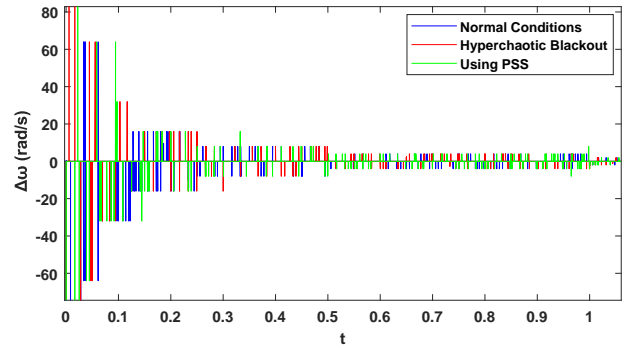


Figure 16 Speed deviation of the generator in a SMIB system that is excited by hyperchaotic system

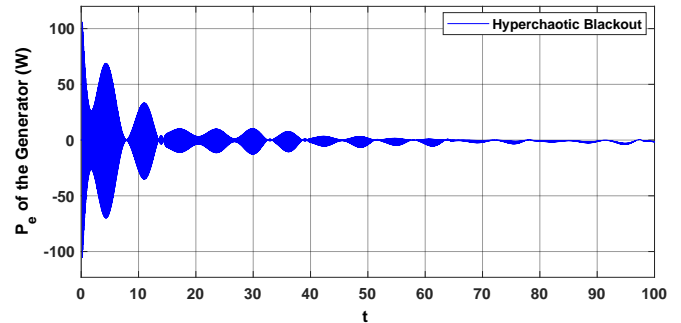


Figure 17 Electrical power in the generator under hyperchaotic blackout condition

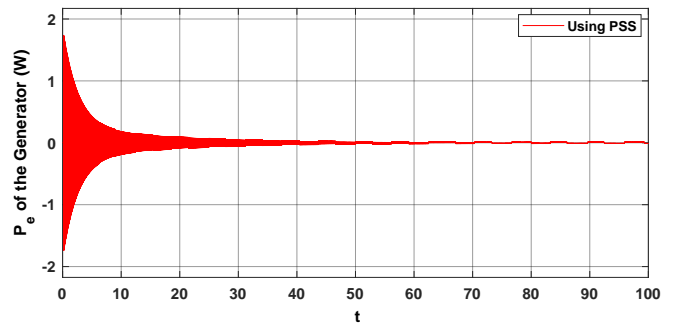


Figure 18 Damping characteristic of electrical power in the generator under hyperchaotic blackout condition

Summary Findings for Cases

As a result, the peak values of the well-known controllers against the proposed blackout is summarized in Table 4. PSS and AVR have slightly regulated the hyperchaotic noise in infinite bus. PID controller has damp out the oscillations better than that of them. PID controlled PSS shows the best damping rate amongst the mentioned controllers. This inference is made given that infinite bus system with hyperchaotic excitation.

In the SMIB system, the output voltages are shown in Fig. 19. The normal effective system voltage is a 220 V. Against the hyperchaotic noise, AVR has provided a great voltage stability. After about 0.2 seconds of oscillation, AVR has provided steady stability. PSS and PID has shown virtually same effects in terms of transient stability. Even though the PID has provided more damping than that of PSS in the long term. The PSS is seen to cause the system unstable in the very long term.

■ Table 4 Deviation values for the infinite bus system

	Peak Overshoot ($\Delta w(t)$)(rad/s)			
	Without Controller	AVR	PSS	PID controlled PSS
Normal	222e-06	219e-06	215e-06	155e-06
Hyperchaotic	0.2342	0.2393	0.177	0.169

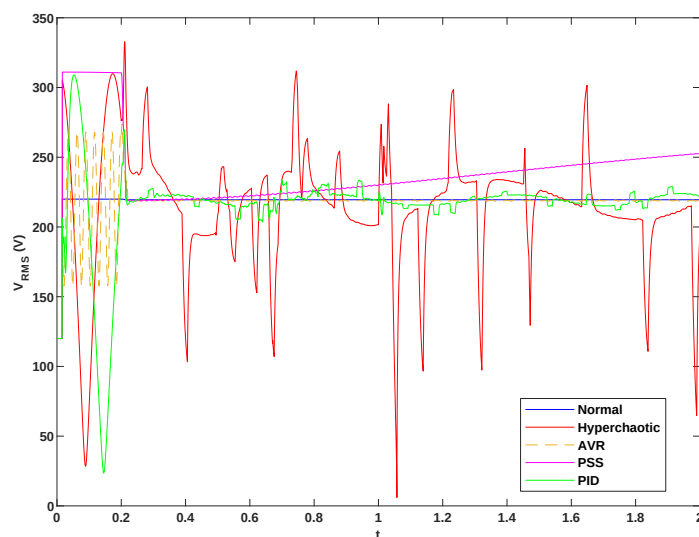


Figure 19 Effective value of the voltage in hyperchaotic noised SMIB system

RESULTS AND DISCUSSION

This study proposes a novel assesment in power system stability for the so-called hyperchaotic noise. Hyperchaotic noise is obtained from an existing system by implementing into the controllers. The test has been realized in the systems that have 11 buses, infinite buses and single machine. The stability analyses of the selected systems have been investigated according to the restorers such as PSS, PID contoller and AVR. That restorers are

investigated whether it maintains against hyperchaotic blackouts. The mentioned analyzes have been realized in cases of nonchaotic, hyperchaotic and hyperchaotic with controller. The effects of the hyperchaotic blackouts in various systems have been presented. As a primary apparatus, the AVR could not immensely prevent the devastating hyperchaotic noises. But, the AVR have showed a great performance in providing voltage stability. The PSS have counteracted the amidst of hyperchaotic blackout in the power systems. The hyperchaotic noise damping rate of the PSS has been close to of PID controller. However, the PID controlled PSS has provided steady stability and small signal stability.

Conflicts of interest

The author declares that there is no conflict of interest regarding the publication of this paper.

LITERATURE CITED

- Ahsan, H. and M. D. Mufti, 2020 Comprehensive power system stability improvement with rocof controlled smes. *Electric Power Components and Systems* **48**: 162–173.
- Chen, H.-K., T.-N. Lin, and J.-H. Chen, 2005 Dynamic analysis, controlling chaos and chaotification of a smib power system. *Chaos, Solitons & Fractals* **24**: 1307–1315.
- Chiang, H.-D., C.-W. Liu, P. P. Varaiya, F. F. Wu, and M. G. Lauby, 1993 Chaos in a simple power system. *IEEE Transactions on Power Systems* **8**: 1407–1417.
- Das, P., P. C. Gupta, and P. P. Singh, 2021 Bifurcation, chaos and pid sliding mode control of 3-bus power system. In *2020 3rd International Conference on Energy, Power and Environment: Towards Clean Energy Technologies*, pp. 1–6, IEEE.
- DELAVARĪ, H. and E. BAYAT, 2015 Comparison of different techniques for tuning of power system stabilizer. *Cumhuriyet Üniversitesi Fen-Edebiyat Fakültesi Fen Bilimleri Dergisi* **36**: 248–257.
- Demello, F. P. and C. Concordia, 1969 Concepts of synchronous machine stability as affected by excitation control. *IEEE Transactions on power apparatus and systems* **88**: 316–329.
- Dong, J., S. Li, S. Wu, T. He, B. Yang, *et al.*, 2017 Nonlinear observer-based robust passive control of doubly-fed induction generators for power system stability enhancement via energy reshaping. *Energies* **10**: 1082.
- Ekinci, S. and B. Hekimoglu, 2018 Parameter optimization of power system stabilizer via salp swarm algorithm. In *2018 5th international conference on electrical and electronic engineering (ICEEE)*, pp. 143–147, IEEE.
- Fonzin Fozin, T., P. Megavarna Ezhilarasu, Z. Njitacke Tabekoung, G. Leutcho, J. Kengne, *et al.*, 2019 On the dynamics of a simplified canonical chua's oscillator with smooth hyperbolic sine nonlinearity: hyperchaos, multistability and multistability control. *Chaos: An Interdisciplinary Journal of Nonlinear Science* **29**: 113105.
- Harb, A. M. and N. Abdel-Jabbar, 2003 Controlling hopf bifurcation and chaos in a small power system. *Chaos, Solitons & Fractals* **18**: 1055–1063.
- Huang, R., R. Diao, Y. Li, J. Sanchez-Gasca, Z. Huang, *et al.*, 2017 Calibrating parameters of power system stability models using advanced ensemble kalman filter. *IEEE Transactions on Power Systems* **33**: 2895–2905.
- Jamal, A., S. Suropto, and R. Syahputra, 2017 Power flow optimization using upfc based on neuro-fuzzy method for multi-machine power system stability. *International Journal of Applied Engineering Research (IJAER)* **12**: 898–907.

- Kumar, R., R. Singh, H. Ashfaq, S. K. Singh, and M. Badoni, 2021 Power system stability enhancement by damping and control of sub-synchronous torsional oscillations using whale optimization algorithm based type-2 wind turbines. *ISA transactions* **108**: 240–256.
- Li, C. and G. Chen, 2004 Chaos and hyperchaos in the fractional-order rössler equations. *Physica A: Statistical Mechanics and its Applications* **341**: 55–61.
- Li, Y., W. K. Tang, and G. Chen, 2005 Hyperchaos evolved from the generalized lorenz equation. *International Journal of Circuit Theory and Applications* **33**: 235–251.
- Liu, Z., C. Wu, J. Wang, and Y. Hu, 2019 A color image encryption using dynamic dna and 4-d memristive hyper-chaos. *IEEE Access* **7**: 78367–78378.
- Matsumoto, T., L. Chua, and K. Kobayashi, 1986 Hyper chaos: laboratory experiment and numerical confirmation. *IEEE Transactions on Circuits and Systems* **33**: 1143–1147.
- Nangrani, S. and S. Bhat, 2018 Fractional order controller for controlling power system dynamic behavior. *Asian Journal of Control* **20**: 403–414.
- Rech, P. C., 2017 Hyperchaos and quasiperiodicity from a four-dimensional system based on the lorenz system. *The European Physical Journal B* **90**: 1–7.
- Rössler, O., 1979 An equation for hyperchaos. *Physics Letters A* **71**: 155–157.
- Rössler, O. E. and C. Letellier, 2020 Hyperchaos. In *Chaos*, pp. 55–62, Springer.
- Sahu, P. R., P. K. Hota, and S. Panda, 2018 Power system stability enhancement by fractional order multi input sssc based controller employing whale optimization algorithm. *Journal of Electrical Systems and Information Technology* **5**: 326–336.
- Sajjadi, S. S., D. Baleanu, A. Jajarmi, and H. M. Pirouz, 2020 A new adaptive synchronization and hyperchaos control of a biological snap oscillator. *Chaos, Solitons & Fractals* **138**: 109919.
- Sauer, P. W. and M. A. Pai, 1998 *Power system dynamics and stability*, volume 101. Wiley Online Library.
- Sharma, A., L. Nagar, N. Patidar, M. Kolhe, S. Nandanwar, *et al.*, 2017 Minimizing uncertainties with improved power system stability using wide area fuzzy-2 logic based damping controller. In *2017 3rd International Conference on Computational Intelligence & Communication Technology (CICT)*, pp. 1–5, IEEE.
- Sheikh, A. F. and S. K. Starrett, 2015 Comparison of input signal choices for a fuzzy logic-based power system stabilizer. In *2015 North American Power Symposium (NAPS)*, pp. 1–6, IEEE.
- Singh, N. and P. Agnihotri, 2018 Power system stability improvement using facts devices. *International Journal of Advance Research and Development* **3**: 171–176.
- Tian, K., C. Bai, H.-P. Ren, and C. Grebogi, 2019 Hyperchaos synchronization using univariate impulse control. *Physical Review E* **100**: 052215.
- Vaidyanathan, S., C. Lien, W. Fuadi, M. Mamat, *et al.*, 2020 A new 4-d multi-stable hyperchaotic two-scroll system with no-equilibrium and its hyperchaos synchronization. In *Journal of Physics: Conference Series*, volume 1477, p. 022018, IOP Publishing.
- Van Dai, L., D. Duc Tung, T. Le Thang Dong, and C. Le Quyen, 2017 Improving power system stability with gramian matrix-based optimal setting of a single series facts device: feasibility study in vietnamese power system. *Complexity* **2017**.
- Wang, X. and M. Wang, 2008 A hyperchaos generated from lorenz system. *Physica A: Statistical Mechanics and its Applications* **387**: 3751–3758.
- Xiu, C., R. Zhou, S. Zhao, and G. Xu, 2021 Memristive hyperchaos secure communication based on sliding mode control. *Nonlinear Dynamics* **104**: 789–805.
- Yu, F., L. Liu, B. He, Y. Huang, C. Shi, *et al.*, 2019 Analysis and fpga realization of a novel 5d hyperchaotic four-wing memristive system, active control synchronization, and secure communication application. *Complexity* **2019**.
- Yu, Y., H. Jia, P. Li, and J. Su, 2003 Power system instability and chaos. *Electric power systems research* **65**: 187–195.
- Yuan, W., X. Yang, W. Guo, and W. Hu, 2017 A double-domain image encryption using hyper chaos. In *2017 19th International Conference on Transparent Optical Networks (ICTON)*, pp. 1–4, IEEE.
- Zhu, S. and C. Zhu, 2020 Secure image encryption algorithm based on hyperchaos and dynamic dna coding. *Entropy* **22**: 772.

How to cite this article: Ozturk, H. *An Analysis of Power System Stability against Hyperchaotic Noises and Blackouts*. *Chaos Theory and Applications*, 3(2), 67-76, 2021.

Vibrational Analysis of a Metallic Column Submitted to Mechanical Axial Load and Fire Exposure

A.N. Ndoukou ^{*}, J. Metsebo ^{α,1} and J.M Njankou [§]

^{*}Department of Architecture and Engineering Arts, Fine Arts Institute, P.O Box 31 Foumban, University of Dschang, Cameroon, ^αDepartment of Hydraulics and Water Management, National Advanced School of Engineering, University of Maroua, P.O Box 46 Maroua, Cameroon, [§]Department of Civil Engineering and Urban Planning of National Advanced School of Engineering, University of Yaounde I, P.O Box 8390 Yaounde, Cameroon.

ABSTRACT Vibrational behavior and structural failure of a metallic beam submitted to simultaneous action of axial load and fire exposure are investigated. Analyses are made at ambient conditions and for two types of fire, ISO 834 fire and parametric fire. Vibrational equation based on heat conduction equation and field equations are constructed and numerically solved to obtain the responses in terms of time histories, bending moment in fire and time to failure against axial load ratio. The heat flux is high enough to affect material properties of the structure and their variation with temperature is taking into account in the mathematical formulation. Results show that heat flux resulting from fire action transforms the buckling problem occurring at room temperature into a bending one. Non-reversible responses and sooner arising of failure are observed for ISO 834 fire even for axial load ratio not able to cause buckling at room temperature. Unlike the case of ISO fire, parametric fire improves reversible deflections within the exposure time and later occurring of failure.

KEYWORDS

Beam vibration
Axial load ratio
ISO 834 fire
Parametric fire
Structural failure
Constructional steel

INTRODUCTION

Structural behavior under temperature change has been of number of analytical, computational and experimental studies performed by several researchers (Aditya 2021; Al-Hamd 2020; Yaobing 2018; Kingsley 2018; Abbas 2016; Harshad 2016; Feng 2012; Nubissie 2011; Mourão 2007; Liu 2006; Ribeiro 2005; Buchanan 2001; Rotter 2000). Mechanical machines often operate under diverse temperature conditions (Nubissie 2011). In internal combustion engines, rocket systems, movement of satellites etc. the conditions are particularly temperature-sensitive. Thermal effects are frequently ignored in research and this may yield totally incorrect results. Literature shows that even moderate change in temperature leads to huge alteration of structural vibration properties (Yaobing 2018).

In civil and structural engineering but also in marine engineering, elevated temperatures are often caused by fire leading to material properties alteration. As a result the performance of these structures is affected due to unwanted dynamic responses and their integrity is sacrificed due to buckling. (Mourão 2007) analyzed the behavior of steel beams under uniform temperature

rising. The study covered beams under several load levels and presented the variation of deflection, critical temperature, bending moment, normal force and stresses with temperature. No type of fire is mentioned in this study and the method is straight computational with the aid of computer software ANSYS. (Sepuro 2001) did similar study with computer software SAFIR but considered some types of fire.

(Ndoukou 2011; Nubissie 2011; Avsec 2007) developed mathematical models where fundamental thermomechanical properties of state are functions of temperature. (Avsec 2007) validated the mathematical model by comparison with experimental data and obtained satisfactory agreement. (Yaobing 2018) used the extended Hamilton principle to model the vibration characteristics of Euler-Bernoulli beams under moderate thermal loads and mechanical excitations. (Feng 2012) applied the principle of minimum acceleration in dynamics of elastic plastic continua coupled with dynamic finite difference to numerically compute the responses of steel beams at elevated temperatures. In the same line with (Sepuro 2001; Ndoukou 2011; Feng 2012) considered a beam supporting transverse mechanical load and ISO 834 fire.

Manuscript received: 6 August 2021,

Revised: 5 October 2021,

Accepted: 27 October 2021.

¹jmetsebo@gmail.com (Corresponding Author)

The present study is devoted to the analysis of vibration characteristics as well as critical temperature at failure of a vertical metallic beam supporting simultaneous actions of axial load and fire, based on mathematical model and numerical simulation. Two types of fire are considered; ISO 834 fire which is the standard fire and parametric fire which is reported by the literature to be closer to the real fire situation. The structure and modeling are presented in Section II, while section III focuses on numerical simulation, results and discussion, with sub-section III.1 for ambient temperature, sub-section III.2 concentrates on ISO 834 fire and sub-section III.3 focuses on parametric fire. A conclusion is drawn in section IV.

STRUCTURE, MATHEMATICAL MODELING AND NUMERICAL SCHEME

The structure

Consider a beam-column submitted to axial load and fire exposure. This situation is common in civil and structural Engineering (buildings and bridges) but also in marine Engineering (offshore). The system consists of an elastic beam with mass m , density ρ , young modulus E , length l , inertial moment I and a rectangular cross section A . An axial load P is applied to the beam which simultaneously undergoes the effect of an external fire. Two types of fire should be studied; the ISO 834 fire and the parametric fire. Under the influence of fire, the beam temperature changes with time and reaches high values that affects its material properties which are called to vary with temperature as the beam vibrates. The coordinates system associated with the beam (figure 1) of width b and thickness h consists of a Cartesian frame with origin O , coinciding with the bottom edge midpoint of the beam. The x -axis is oriented toward the beam length such that $0 \leq x \leq l$ the y -axis is parallel to the beam width such that $-\frac{b}{2} \leq y \leq \frac{b}{2}$ and the z -axis parallel to the thickness with $-\frac{h}{2} \leq z \leq \frac{h}{2}$.

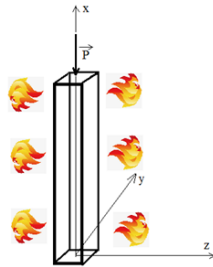


Figure 1 Sketch of the investigated system

Mathematical modeling

The following assumptions are made :

- The fire is uniformly distributed along the beam;
- Material degradation is not considered though material properties are temperature-dependent;
- The study is made under the limit of validation of Hooke law.

The system modeling the beam behavior in such a situation consists of the heat conduction equation coupled with the field equation written respectively as follows (Timoshenko 1951; Nayfeh 1979; Kant 1991; Huang 2002)

$$c_p(T) \frac{\partial T}{\partial t} = \lambda_T \left(\frac{\partial^2 T}{\partial x^2} + \frac{\partial^2 T}{\partial z^2} \right) - \alpha_T E(T) \frac{\partial \varepsilon}{\partial t} \quad (1)$$

$$\begin{aligned} \frac{m}{l} \frac{\partial^2 U}{\partial t^2} + c \frac{\partial U}{\partial t} + E(T) I \frac{\partial^4 U}{\partial x^4} + [E(T) A \alpha_T \Delta T + P] \frac{\partial^2 U}{\partial x^2} \\ = \frac{\partial^2 M_T}{\partial x^2} + \frac{E(T) A}{2I} \left(\int_0^l \left(\frac{\partial U}{\partial x} \right)^2 dx \right) \frac{\partial^2 U}{\partial x^2} \end{aligned} \quad (2)$$

Equation (1) must be completed with prescribed boundary and initial conditions on temperature. Into equation (2), the term $E(T) A \alpha_T \Delta T$ refers to the internal axial load developed in the member as a result of thermal expansion against ends restraints. Equation (2) has to be completed with given initial and boundary conditions on displacement. A beam with clamped-clamped ends has been considered in this study In equations (1) and (2), U is the transversal displacement of the beam, α_T is the thermal conductivity, $T(x, t)$ is the temperature field, $\varepsilon(x, t)$ the total strain, $c_p(T)$ the specific heat, λ_T the coefficient of thermal expansion, $\Delta T = T - T_0$ the temperature difference, T_0 the room temperature and M_T the thermal moment given by the following expression :

$$M_T = E(T) b \alpha_T \int_{-h/2}^{h/2} (T(x, z, t) - T_0) z dz \quad (3)$$

In Eqs. (1)-(2), since the temperature varies in a range that affects material properties, one has to take into account the variation with temperature of material properties (see appendix). One is concerned for the purpose of this study with constructional steel. According to the above assumption, the mass $m(T)$ of the beam is taken to be constant. It is also assumed that the heat flow that acts on the beam is much slower than the mechanical stress-strain variations. Therefore, the temperature distribution can be considered independent of the deformation and can thus be defined by a given function which represents the quasi-steady state of the heat transfer equation (1). This allows the reduction of the conductivity equation. The temperature field is assumed to be uniform along the beam and the thermal moment intervening in equation (2) thus vanishes. The design fire is modeled by an international standard time-temperature law defined for ISO 834 from (Eurocode 3 2003) by:

$$T(t) = T_0 + 345 \ln(8t + 1) \quad (4)$$

The parametric fire will be modeled later. Thereafter, the system of equations (1)-(2) is reduced to the following dimensionless equation.

$$\begin{aligned} \frac{\partial^2 U}{\partial t^2} + \mu g(t) \frac{\partial U}{\partial t} + g(t) k_e(t) \frac{\partial^4 U}{\partial x^4} + g(t) [\alpha + \gamma \alpha_T \Delta T k_e(t)] \frac{\partial^2 U}{\partial x^2} \\ = \varepsilon \beta g(t) \left(\int_0^1 \left(\frac{\partial U}{\partial x} \right)^2 dx \right) \frac{\partial^2 U}{\partial x^2} \end{aligned} \quad (5)$$

Where, function $g(t)$ and $k_e(t)$ are given in Eq. (17)-(19) (see appendix).

$$\alpha = \frac{PL^2}{E_0 I}; \quad \beta = \frac{AL^2}{I} \quad (6)$$

α is the axial load ratio and ε the nonlinearity coefficient. The critical Euler load is classically given by :

$$P_{cr} = \pi^2 \frac{EI}{L^2} \quad (7)$$

Therefore, setting $\alpha_{cr} = \frac{P_{cr}L^2}{EI}$, one obtains $\alpha_{cr} = \pi^2$.

It should be pointed out that P_{cr} is influenced by temperature change and can be written at any temperature as follows :

$$P_{cr}(T) = P_{20}k_e(T) \quad (8)$$

Where $k_e(T)$ is given in Eq. (A.2). The variation of P_{cr} with temperature is plotted in fig. 2. It is a decreasing function of temperature.

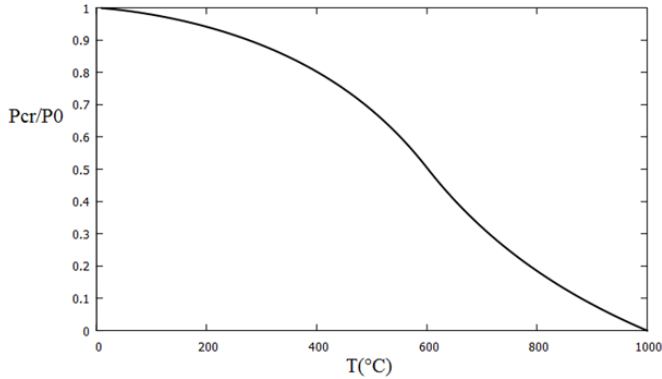


Figure 2 Variation with temperature of critical load ratio

NUMERICAL SIMULATION, RESULTS AND DISCUSSIONS

Nonlinear integral partial differential equation (5) is numerically computed for constructional steel with the following parameters values.

$$\begin{aligned} E &= 2.1 \times 10^{11} \text{ Pa}; & I &= 5.2 \times 10^{-7} \text{ m}^2; & \rho &= 7800 \text{ kg.m}^{-3}; \\ A &= 2.5 \times 10^{-3} \text{ m}^2; & L &= 0.5 \text{ m}; & \alpha_T &= 14 \times 10^{-6} \text{ }^\circ\text{C}^{-1} \end{aligned} \quad (9)$$

Initial and boundary conditions associated with equation (5) are set as follows. For the concern of boundary conditions, a beam clamped at both ends is considered as this is one of the frequently found situations for structural components in engineering.

$$U(0,t) = \frac{\partial U(0,t)}{\partial x} = 0; \quad U(1,t) = \frac{\partial U(1,t)}{\partial x} = 0 \quad (10a)$$

$$U(x,0) = \frac{\partial U(x,0)}{\partial t} = 0 \quad (10b)$$

Zero initial conditions on deflection and velocity have been considered and associated with a small transverse load $q = 5 \text{ N/m}$ for the sake of nontrivial solutions.

A full discretization using centered finite differences within space of PDE (5) associated with Runge Kutta 4 on time, has been used for the purpose of numerical method. The axial load ratio α is varied as the temperature increases in the beam and the previous equation is numerically solved in the sake of vibrational behavior of the structure.

Behaviour at ambient conditions

Fig. 3 presents the deflection versus position within the mid-line of the beam at ambient conditions. It can be observed that the mid-span position admits maximum deflection amplitude. The effect of temperature on this result will be presented in the next sections.

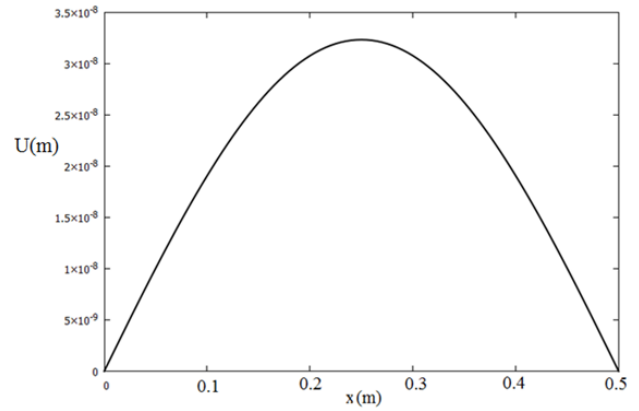


Figure 3 Deflection versus position on the beam mid-line at ambient temperature for $\alpha = 0.5$

Figures 4(a)-4(c) present the time histories of the beam mid-span at ambient temperature for different values of axial load ratio, namely $\alpha = 0.25$ (fig.4(a)), $\alpha = 0.5$ (fig. 4(b)) and $\alpha = 0.75$ (fig.4(c)). It can be seen that the deflection has constant amplitude within the time and there is no notably change in amplitude nor in frequency for these different values of axial load ratios. The effect of fire on these responses are investigated in the next sections. Figures 4(d) and 5(a) present the time history and bending moment at beam mid-span for higher value of axial load ratio, $\alpha = 9.0$. It is found that amplitude and frequency of oscillations had increased compared to the previous cases corresponding to smaller values of α (figs. 4(a)-4(c)). Meanwhile, the oscillations remain regular within the time. However as from the critical value of axial load ($\alpha = 10.0$), oscillations lose their regular behaviour and the beam responds with increasing amplitude within the time. This can be seen in figures 5(b) and 5(c) presenting mid-span time history and bending moment at room temperature for critical value of axial load ratio, $\alpha = 10 \approx \alpha_{cr}$. It can be seen in these figures that the responses explode due to the buckling of the structure at critical axial load ratio.

This inspires to plot the time to failure of the beam as a function of axial load ratio at room temperature (see fig. 5(d)). To obtain this figure, a failure criterion is defined (see eq.(11)) comparing the resistant moment of the beam and the bending moment resulting from the applied loads.

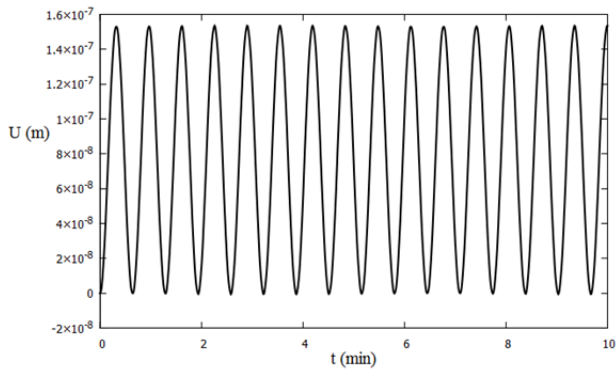
$$M(t) \geq \eta M_{cr} \quad (11)$$

where

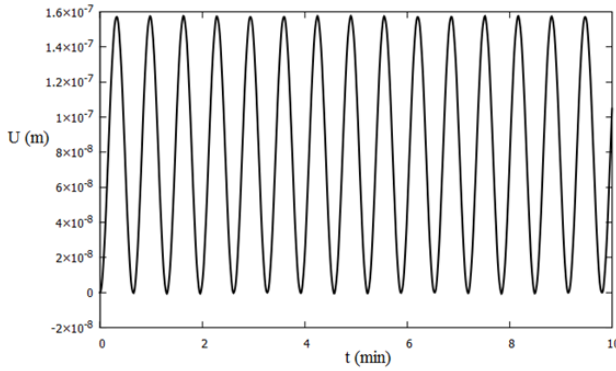
$$M_{cr} = \sigma_0 \times A \quad (12)$$

σ_0 is the temperature free yield stress and η is a safety factor.

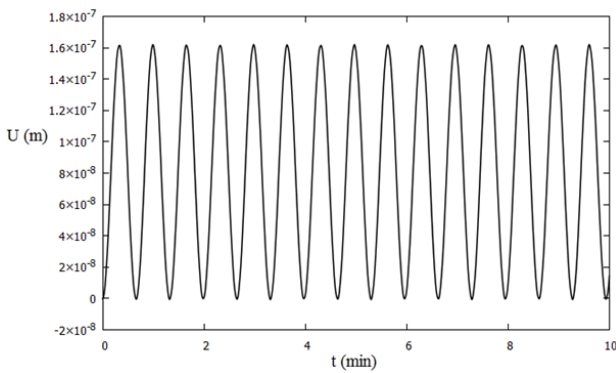
It is observed that the time to failure is a decreasing function of the axial load ratio. The beam undergoes rapid collapse for α greater than the critical value $\alpha_{cr} \approx 10.0$, and the higher the value of α , the sooner the failure. Eqs. (11)-(12) show that the time to failure grows with the cross section of the beam.



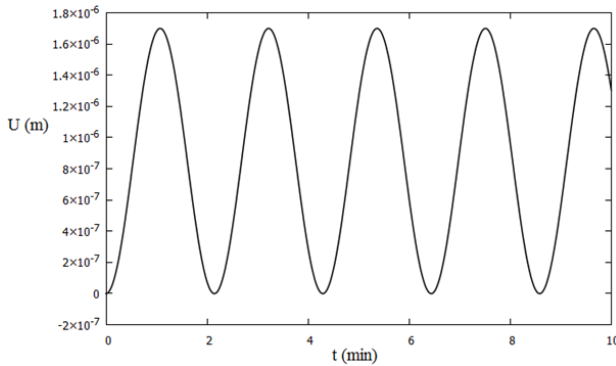
(a) Time history at room temperature for $\alpha = 0.25$



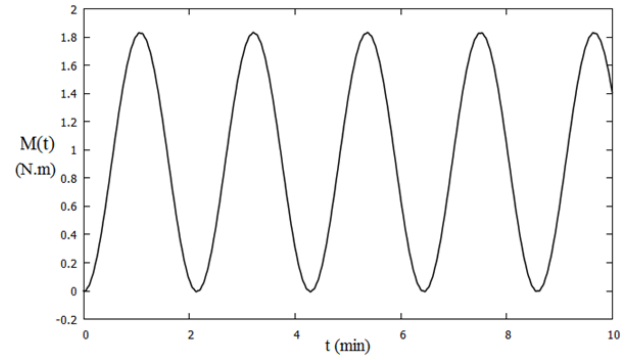
(b) Time history at room temperature for $\alpha = 0.5$



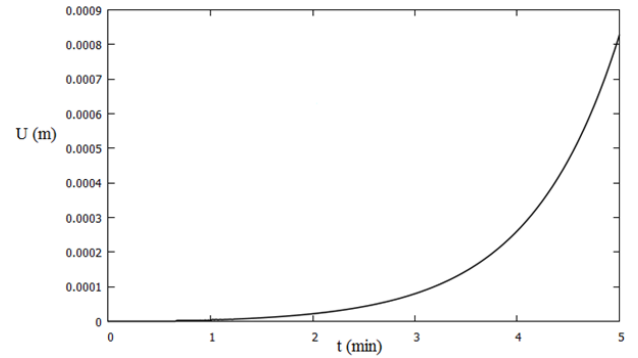
(c) Time history at room temperature for $\alpha = 0.75$



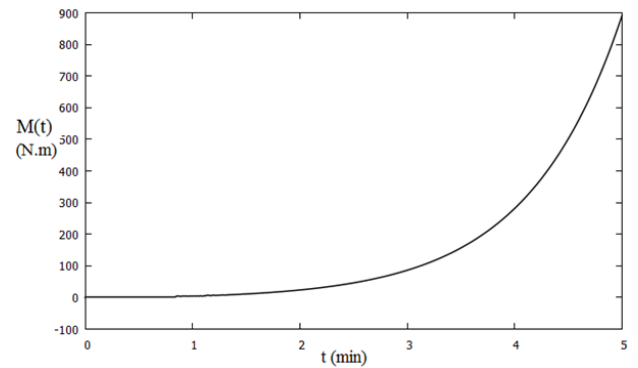
(d) Time history at room temperature for $\alpha = 9.0$



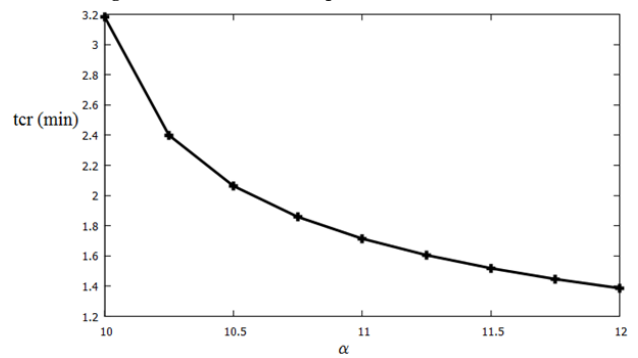
(a) Bending moment at room temperature for $\alpha = 9.0$



(b) Time history at room temperature for $\alpha = 10.0$



(c) Bending moment at room temperature for $\alpha = 10.0$



(d) Time to failure against axial load ratio at ambient temperature

Figure 4 Time history at room temperature for different values of α

Figure 5 Time history and Bending moment at room temperature for different values of α

Observing fig. 5(d), an approximated analytical expression given tc as a function of axial load ratio α can be suggested as follows.

$$tc = \frac{2.0}{\alpha - 9.5} \quad (13)$$

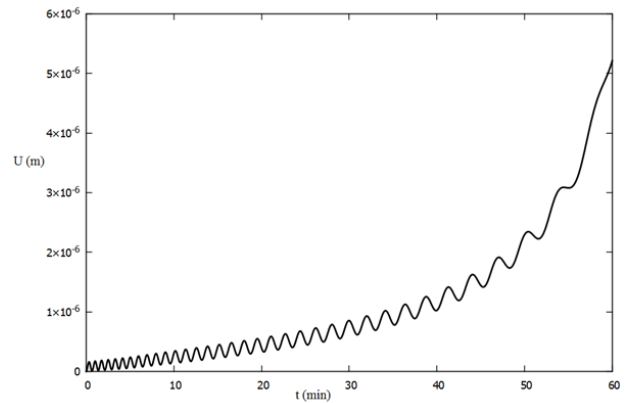
Such an expression is useful in practice as it allows designers to set some predictions from simple calculation. Eq. (13) gives a graph quite similar to that of fig. 5(d) for α belonging to the interval [10 – 12].

Behaviour in presence of ISO fire 834

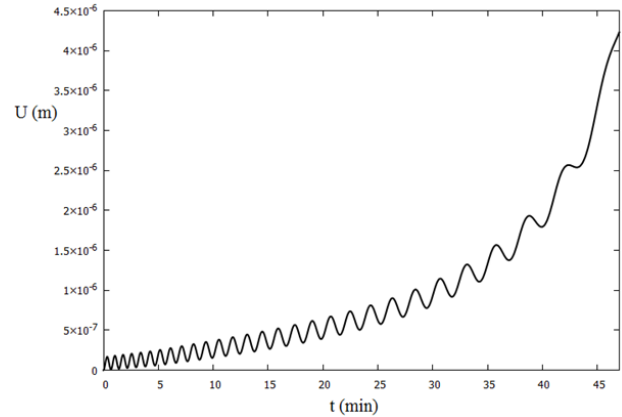
Vibrational responses: In presence of an ISO 834 fire modeled by the time-temperature law (Eq.4), the following results are obtained. Figures 6 present mid-span time histories in presence of ISO 834 fire and mechanical load with axial load ratios $\alpha = 0.25$ (Fig. 6(a)), $\alpha = 0.5$ (Fig. 6(b)) and $\alpha = 0.75$ (Fig. 6(c)) respectively. Figures 7 present the bending moment in fire for same conditions and parameters. It can be observed in opposition to the situation at ambient temperature previously presented in figures 4(a)-4(c) where amplitudes of oscillations were small and constant that in presence of fire, oscillations amplitudes keep increasing during the fire action. Moreover, a shift within the time towards positive values of the centers of oscillations is observed. This agrees with results obtained from computational software ANSYS and SAFIR (Seputro 2001; Mourão 2007).

It is also important to note that after some duration of fire exposure, oscillations lose their reversible character and amplitudes keep increasing with a faster speed. Figures 5-7 show that oscillation amplitudes increase with axial load ratio in presence of fire faster than in ambient conditions. In presence of fire, oscillations lose their reversible character sooner for greater values of α . As an example, this happens after 50 minutes exposure to fire for $\alpha = 0.25$, 40 minutes for $\alpha = 0.5$ and 35 minutes for $\alpha = 0.75$, see Figures 7.

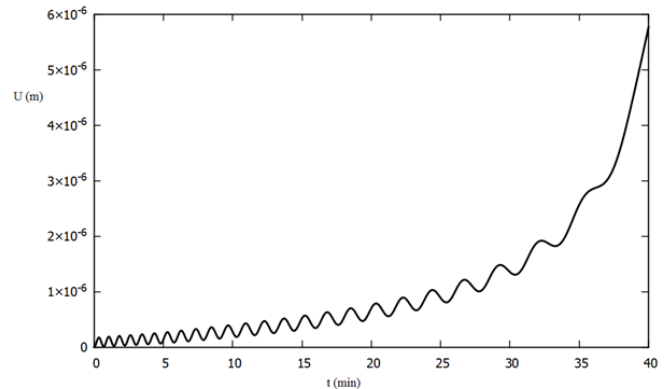
Figure 8 presents the mid-span time history in presence of fire for different positions along the beam. It is seen that the maximum deflection amplitudes are observed for the beam mid-span as was the case in figure 3 for ambient conditions. Figure 9 presents the beam deformation versus position on the beam mid-line in presence of fire for axial load ratio $\alpha = 0.5$, at different temperature $T = 100^\circ\text{C}$ (Fig. 9b) and $T = 300^\circ\text{C}$ (Fig. 9c). These responses are compared with those obtained at ambient conditions (Fig. 9a) in order to exhibit the influence of warming on the responses. It is observed that the deflection amplitude grows with temperature and is at 100°C three times the one at ambient conditions while at 300°C it worth about nine times the amplitude at room temperature.



(a) Time history in presence of fire for $\alpha = 0.25$

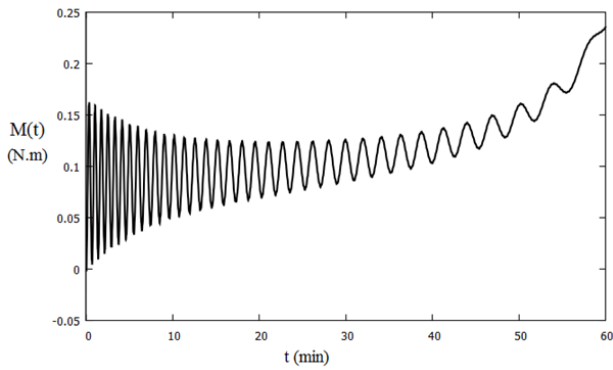


(b) Time history in presence of fire for $\alpha = 0.5$

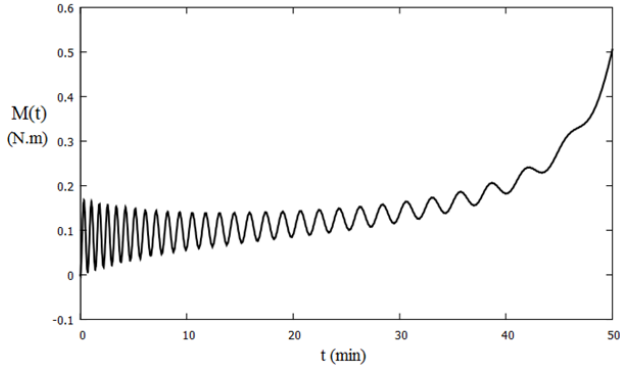


(c) Time history in presence of fire for $\alpha = 0.75$

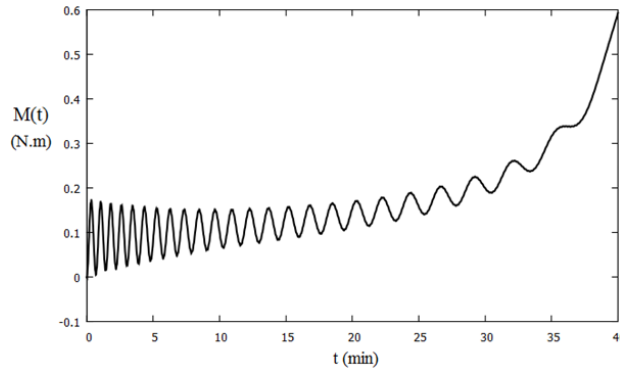
Figure 6 Time history in presence of fire for different values of α



(a) Bending moment in fire for $\alpha = 0.25$



(b) Bending moment in fire for $\alpha = 0.5$



(c) Bending moment in fire for $\alpha = 0.75$

Figure 7 Bending moment in fire for different values of α

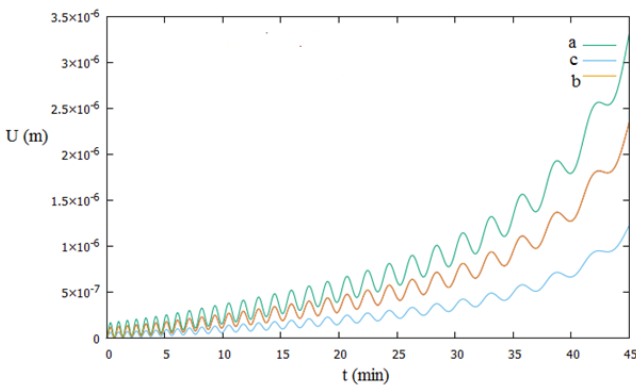


Figure 8 Time histories at different positions along the beam (a) mid-span, (b) height, (c) quarter.

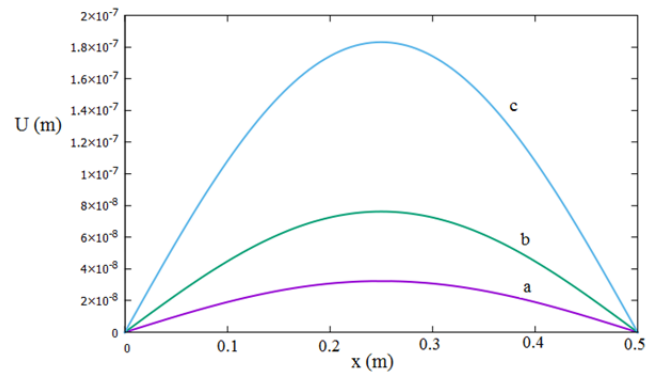


Figure 9 Deflection versus mid-line position of the beam at different temperatures. $\alpha = 0.5$ (a) $T = 20^\circ\text{C}$, (b) $T = 100^\circ\text{C}$, (c) $T = 300^\circ\text{C}$ (at $t=30$ min)

Structural failure under ISO 834 fire: The above observation inspires to think of structural failure after some time spent by the structure under simultaneous actions of fire exposure and mechanical applied and internal axial loads. What is referred to as structural failure here is not necessarily the collapse of the structure but the fact of reaching a limit state of usage defined by the needed design. As one is dealing with civil and structural engineering components such as buildings or bridges, it is advantageous to define this limit so as to avoid structural damage which could be a risk for people or goods using the structure but also for firefighting personal. This is the reason why the elastic limit is considered as the limit state of usage in this study and as such a safety factor η ($0 \leq \eta \leq 1$) is introduced into the failure criterion under fire. Hence conditions set in eqs (11)-(12) are used with actually the resistance moment in fire being a function of time as it is influenced by temperature (Seputro 2001; Ndoukouo 2011; Nubissie 2011). The bending moment in fire results of all mechanical and thermal action on the structure. Eq.(12) becomes :

$$M_{cr}(t) = \sigma_{cr}(t) \times A = \sigma_0 k_y(t) A \quad (14)$$

$k_y(t)$ is the reduction factor of the yield strength defined as a sequential relation of temperature and thus of time (see eqs. A-7-A-8 (A.7)-(A.8)). σ_0 is the temperature free yield stress. Condition (11) associated with eq.(14) enables to obtain Fig. 10 presenting the time to failure of the structure in fire as a function of axial load ratio. It is observed that the time to failure decreases as the axial load ratio increases. This time indicates the maximum duration the fire fighting personal disposes in order to proceed with the rescue of people and goods present in the structure without enormous risk of damaging the mechanical integrity of the carrying structure. Figure 11 presents the critical deflection reached with corresponding time to failure of the fire-exposed structure. These deflections are increasing function of the critical time.

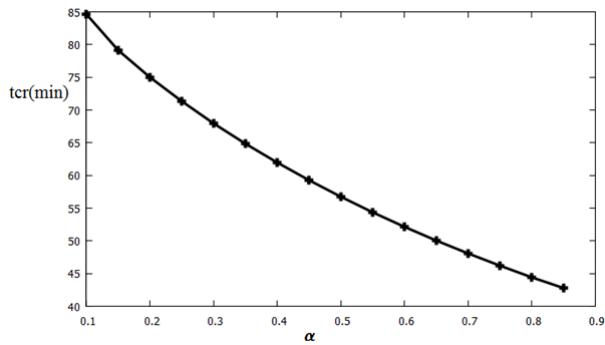


Figure 10 Failure time as a function of axial load ratio under ISO 834 fire

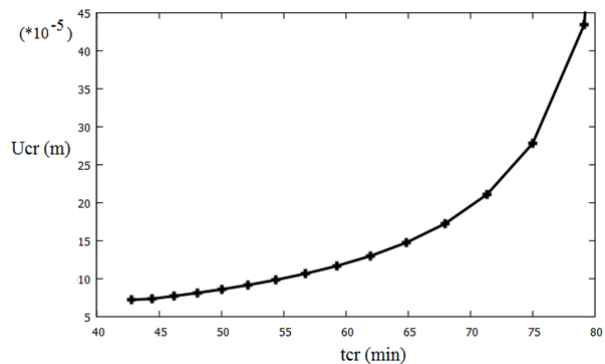


Figure 11 Critical deflection in fire versus time to failure for ISO 834 fire

Behaviour in presence of parametric fire

Vibrational responses: For the sake of comparison of results obtained from ISO 834 fire, we consider a more realistic model in this section, namely, the parametric fire. It is made of a burning phase where fire grows following the standard ISO curve and a cooling phase following a linear heating rate. For the considered parametric fire, the growing period lasts for the first twenty minutes and the cooling phase follows a decay rate of 625°C per hour according to Eurocode reference decay rate (ECI, 1994). The corresponding time-temperature law can be written as follows :

$$T(t) = \begin{cases} T_0 + 345 \ln(8t + 1) & : t \leq 20\text{min} \\ -10.416(t - 20) + 781 & : t \geq 20\text{min} \end{cases} \quad (15)$$

Applying this type of fire to the investigated system, the following results are obtained.

Figures 12 and 13 present the mid-span time history and bending moment in fire for parametric fire with mechanical axial load ratio equal to 0.5. Figure 14 presents the mid-span time history in fire for axial load ratios $\alpha = 1.0$. Figures 15 and 16 present the mid-span time history and bending moment in fire for $\alpha = 2.0$. Unlike the previously studied case of ISO 834 fire, it is observed that the deflection does not increase abruptly with fire exposure time.

There is an increase of deflection during the burning phase followed by a decrease during the cooling phase. This agrees with results obtained with the aid of computational software SAFIR (Sepuro 2001). Moreover, due to the cooling, the rapid increase

of deflection with sooner arise of irreversible deformation as was the case with ISO 834 fire is not observed for parametric fire. It is possible for structure under this type of fire to undergo elastic deformation for axial load ratios greater than the values that induce irreversible responses under ISO 834 fire. This will obviously impacts structural failure under parametric fire differently from what obtained with ISO 834. This can be understood since parametric fire burns up to a given duration (20 minutes for the considered case) and starts decaying afterwards whereas this is not the case for ISO fire.

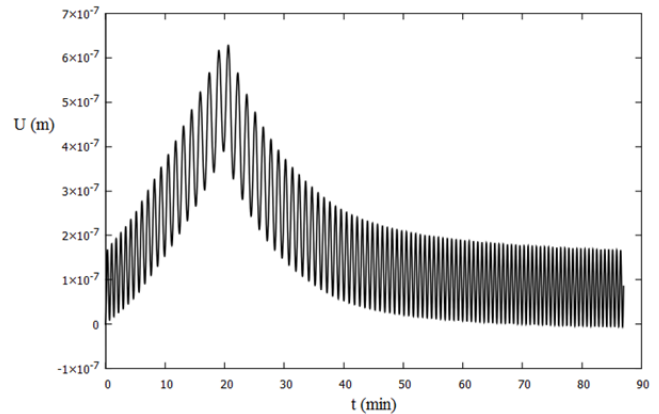


Figure 12 Time history at beam mid-span for parametric fire $\alpha = 0.5$

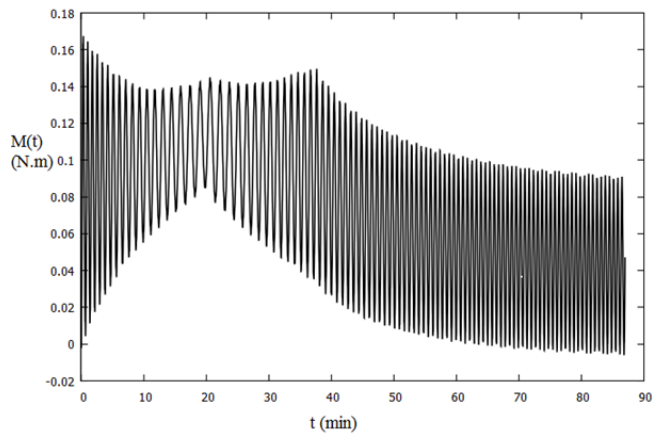


Figure 13 Bending moment in fire at beam mid-span for parametric fire. $\alpha = 0.5$

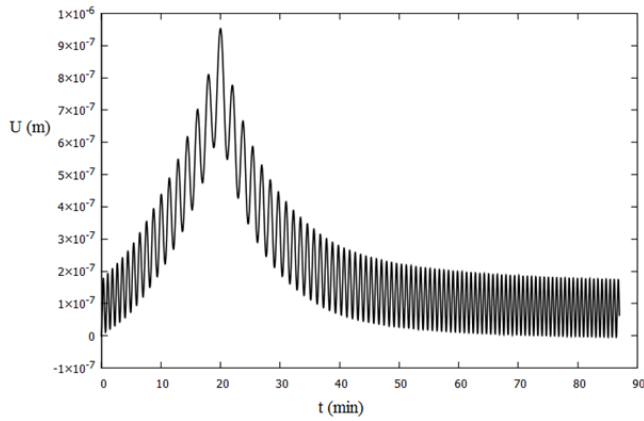


Figure 14 Time history at beam mid-span for parametric fire. $\alpha = 1.0$

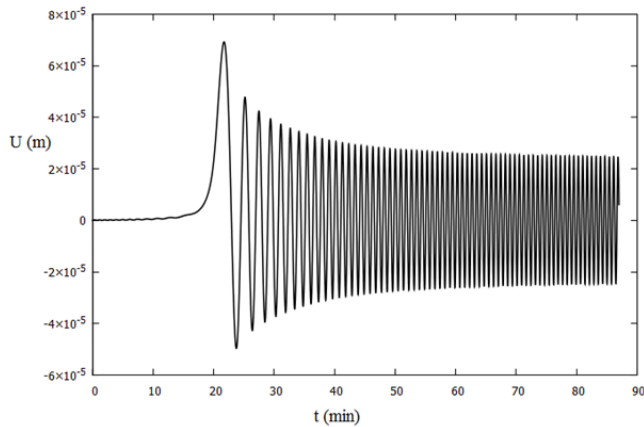


Figure 15 Time history at beam mid-span for parametric fire. $\alpha = 2.0$

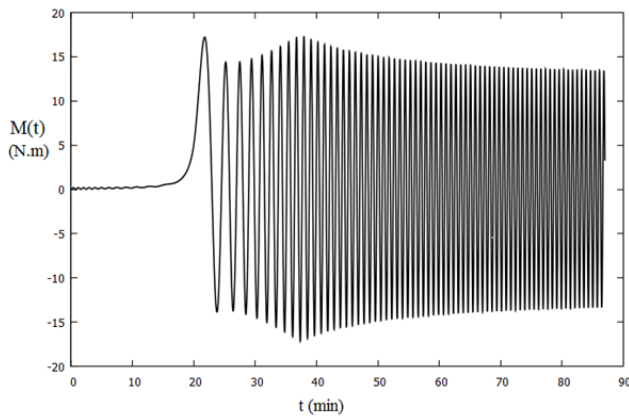


Figure 16 Bending moment in fire at beam mid-span for parametric fire. $\alpha = 2.0$

Structural failure under parametric fire: Vibrational analysis made in previous section for parametric fire exposed beam has given results with some important differences as regard to those obtained under Iso fire. This section investigates the structural failure of the beam under simultaneous action of mechanical axial load and parametric fire. Taking into account the time-temperature law modeling the parametric fire (eq.13) and the failure conditions (eq.11) and (eq.12) the following results are obtained. Figure 17 presents the time to failure of the beam as a function of axial load ratio while figure 18 presents the variation of the reached maximum deflection with the corresponding time to failure. It is seen that the time to failure is a decreasing function of the axial load ratio. It can be noted that there is no failure by vibration for axial load ratio less than $\alpha = 2.0$ whereas one had obtained failure by vibration with axial load ratio less than $\alpha = 1.0$ in presence of ISO fire (see fig. 10). This can be explained by energy and momentum redistribution associated with internal axial load in the beam due to cooling phase of the parametric fire.

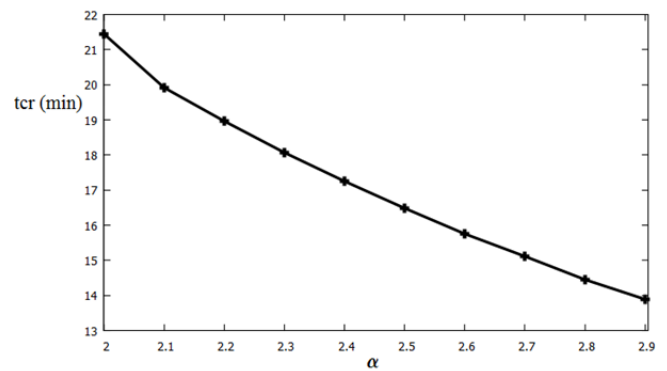


Figure 17 Failure time as a function of axial load ratio under parametric fire

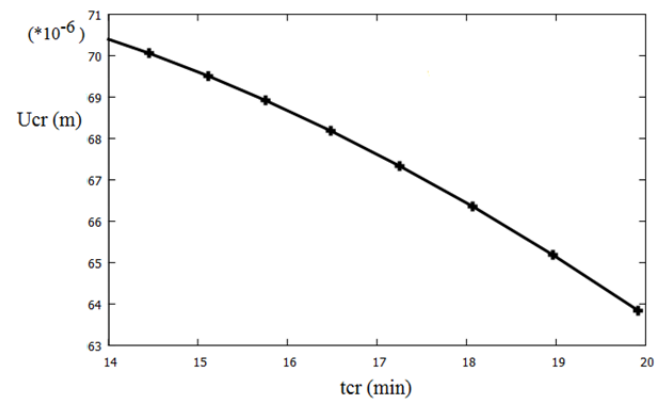


Figure 18 Critical deflection in fire versus time to failure for parametric fire

CONCLUSION

Vibrational behavior as well as structural failure of a metallic clamped column, supporting mechanical axial load and simultaneous action of fire exposure have been investigated. Two types of fire have been considered, namely standard ISO fire 834 and parametric fire. A model based on the heat conduction equation and field equations with inclusion of temperature-dependence of physical parameters of the structure as well as internal axial load due to thermal expansion has been considered. For the purpose of numerical simulation of the obtained PDEs, real numerical data from constructional steel have been chosen. Results have been presented in terms of vibrational analysis and structural failure in fire. For vibrational analysis concern, beam deformation against position for several temperatures, time histories as well as bending moment in fire have been presented for the two types of fire. As per the structural failure concern, structural failure conditions have been set and results presented in terms of time to failure as a function of axial load ratio and maximum deflection reached against critical time for ISO 834 fire and for parametric fire.

As far as the vibrational analysis is concerned it has been obtained that for ISO fire the deflection amplitude grows with time and the axial load ratio. Higher values of axial load ratio generate higher deflection amplitude with rapid increase within the time and sooner arrival of irreversible responses. The axial load ratio could not exceed some critical value for this type of fire without sooner apparition of irreversible responses. Meanwhile in presence of parametric fire, deflection amplitudes increase during the burning period and decrease during the cooling phase. However this type of fire shows an improvement of reversible deflection within the time. Moreover the responses do not diverge for axial load ratio greater than those giving irreversible responses under ISO fire, although the deflection and bending moment present higher values for greater values of axial load ratio.

As per the structural failure concern, the time to failure has been obtained as a decreasing function of the axial load ratio for each type of fire. Under ISO 834 fire the time to failure has been obtained for axial load ratio values less than 1.0, with sooner irreversible responses for greater values of axial load ratios. Meanwhile under parametric fire there was no failure by vibration for axial load ratio less than $\alpha = 2$ unlike the case of ISO fire 834.

APPENDIX

Variation laws with temperature of some material properties of the structure (Seputro 2001; Eurocode 2003; Ndoukouo 2011; Feng 2012). The modulus of elasticity can be written at any temperature as:

$$E = E(T) = E_0 k_e(T) \quad (\text{A-1})$$

In Eq. A-1, $k_e(T)$ denotes the reduction factor of the Young modulus and can be obtained as a function of temperature for the given material the structure is made with. E_0 represents the value of the Young modulus at ambient temperature T_0 . In the case of constructional steel for example $k_e(T)$ can be given as follows :

$$k_e(T) = \begin{cases} 1.0 + \frac{T}{2000 \ln \frac{1}{1100}} : & 20^\circ \text{C} \leq T \leq 600^\circ \text{C} \\ 690 \times \frac{1 - \frac{T}{1000}}{T - 53.5} : & 600^\circ \text{C} \leq T \leq 1000^\circ \text{C} \end{cases} \quad (\text{A-2})$$

For the concern of variation with temperature of the effective length of the beam, the thermal elongation can be written as a function of thermal expansion :

$$l(T) = L(1 + \varepsilon_{th}) = L(1 + \alpha_T \Delta T) = Lg(T) \quad (\text{A-3})$$

$l(T)$ represents the effective length of the beam at current temperature and L the length at room temperature. Function $g(T)$ is given by :

$$g(T) = \begin{cases} 1 + 1.2 \times 10^{-5}T + 0.4 \times 10^{-8}T^2 - 2.416 : & 20^\circ \text{C} \leq T \leq 750^\circ \text{C} \\ 1 + 1.1 \times 10^{-2}T : & 750^\circ \text{C} \leq T \leq 860^\circ \text{C} \\ 2 \times 10^{-5}T - 6.2 \times 10^{-3} : & 860^\circ \text{C} \leq T \leq 1200^\circ \text{C} \end{cases} \quad (\text{A-4})$$

The variation with temperature of the specific heat is given as follows :

$$c_p(T) = \begin{cases} 425 + 7.73T - 1.69 \times 10^{-3}T^2 + 2.22 \times 10^{-6}T^3 : & 20^\circ \text{C} \leq T \leq 600^\circ \text{C} \\ 666 + \frac{13002}{738-T} : & 600^\circ \text{C} \leq T \leq 735^\circ \text{C} \\ 545 + \frac{17820}{T-731} : & 735^\circ \text{C} \leq T \leq 900^\circ \text{C} \\ 650 : & 900^\circ \text{C} \leq T \leq 1200^\circ \text{C} \end{cases} \quad (\text{A-5})$$

Meanwhile the temperature-dependent thermal conductivity is given as :

$$\lambda_T = \begin{cases} 54 - 3.33 \times 10^{-2}T : & 20^\circ \text{C} \leq T \leq 800^\circ \text{C} \\ 27.3 : & 800^\circ \text{C} \leq T \leq 1200^\circ \text{C} \end{cases} \quad (\text{A-6})$$

The yield strength of the material at given temperature $\sigma(T)$, is related to the value of room temperature by the following relation :

$$\sigma(T) = \sigma_0 k_y(T) \quad (\text{A-7})$$

The reduction factor $k_y(T)$ varies with temperature as follows :

$$k_y(T) = \begin{cases} 1.0 : & 20^\circ \text{C} \leq T \leq 215^\circ \text{C} \\ (905 - T) / 690 : & 215^\circ \text{C} \leq T \leq 905^\circ \text{C} \end{cases} \quad (\text{A-8})$$

Conflicts of interest

The authors declare that there is no conflict of interest regarding the publication of this paper.

Availability of data and material

Not applicable.

LITERATURE CITED

- Abbas, Y. A. S. A. R. M. I., H. Al-Salloum, 2016 Post-heating response of concrete-filled circular steel columns. *KSCE Journal of Civil Engineering* **21**: 1367–1378.
- Aditya, A.-K., K., 2021 Post-fire exposure behaviour of circular concrete-filled steel tube column under axial loading. *Int. Journal of Steel Structures* **21**: 52–56.
- Al-Hamd, G. M. M. S. C. L., R., 2020 Influence of loading ratio on flat slab connections at elevated temperature : A numerical study. *Frontiers of Structural and Civil Engineering* **14**: 664–674.
- Avsec, O. M., J., 2007 Thermal vibrational analysis for simply supported beam and clamped beam. *Journal of Sound and Vibration* **308**: 514–525.
- Buchanan, . A., 2001 *Structural Design for Fire Safety*. Wiley.
- Eurocode, 2003 *Design of Steel Structures-Structural Fire Design*. European Committee for Standardization.
- Feng, Y. L., X., 2012 Criteria of limiting temperature and parametric analysis of the large deflection behavior for fully restrained steel beam. *Sci. China Technology* **55**: 264–275.
- Harshad, K. S., D., 2016 Behavior of steel structure under the effect of fire loading. *Journal of Engineering Research and Applications* **6**: 42–46.
- Huang, K. G., H., 2002 Buckling and initial postbuckling behavior of sandwich beams including transverse shear. *AIAA journal* **57**: 2331–2335.
- Kant, P. H., T., 1991 Buckling load of sandwich columns with a higher order theory. *Journal of Reinforced Composites* **10**: 102–109.
- Kingsley, C. G. J. B. S. J. U. S. . A. A., U., 2018 Design of continuous concrete filled steel tubular column in fire. *Thin-Walled Structures* **131**: 192–204.
- Liu, K. G., L., 2006 Thermal buckling of heat-exposed axially restrained composite column. *Composites part A* **37**: 972–980.
- Mourão, S. V., H., 2007 On the behaviour of single-span steel beams under uniform heating. *J Braz Soc Mech Sci Eng* **29**: 115–122.
- Nayfeh, M. D., A., 1979 *Nonlinear Oscillations*. New York (N.Y.) : Wiley.
- Ndoukouo, N. A. W. P., A., 2011 On the dynamics of fire-exposed steel beam under mechanical load. *Journal of Constructional Steel Research* **67**: 1864–1871.
- Nubissie, N. A. . W. P., A., 2011 Dynamical behavior of a wooden beam under mechanical loading and fire. *Materials and Design* **32**: 1331–1336.
- Ribeiro, M. E., P., 2005 The effect of temperature on the large amplitude vibrations of curved beams. *Journal of Sound and Vibration*. **285**: 1093–1107.
- Rotter, A., J.; Usmani, 2000 Fundamental principles of structural behaviour under thermal effects. In *Proceedings First International Workshop on the Performance of Structures in Fire*, Copenhagen.
- Seputro, J., 2001 *Effect of Support Conditions on Steel Beams Exposed to Fire*. phdthesis, School of Engineering, University of Canterbury: New Zealand.
- Timoshenko, J., S.; Gere, 1951 *Theory of elastic stability*.

Yaobing, C. H., Z., 2018 Temperature effects on nonlinear vibration behaviors of euler-bernoulli beams with different boundary conditions. *Shock and Vibration* **6**: 1–11.

How to cite this article: Ndoukouo, A. N., Metsebo, J., and Njankouo, J. M. Vibrational analysis of a metallic column submitted to mechanical axial load and fire exposure. *Chaos Theory and Applications*, 3(2), 77-86, 2021.

Discussions on the Special and General Theory of Relativity

Zeki Caliskan *.1

*Independent Researcher, 500.yil Avenue, Istanbul, 34180, Turkey.

ABSTRACT In this study, the Michelson–Morley experiment and the result of this experiment (the speed of light appears to be the same in all directions) were explored. Although Lorentz gave a mathematical explanation (Lorentz transformations) for this, he did not explain the decreasing momentum with the internal motion of systems. In relation to this decreasing momentum, Einstein solved the problem mathematically by proposing that the mass of the systems increases with the movement of systems (moving mass). We will study this process in a chronological order below. Our primary purpose in this study is to open a platform for discussion by asking questions about the changes in moving systems, as suggested by Lorentz and Einstein (length contraction and mass increase of the object), and to propose a different relativity model by presenting our suggestions and opinions in relation to these discussions.

KEYWORDS

Michelson–Morley experiment
Special and general relativity
Lorentz transformations
Moving mass

INTRODUCTION

We will define our interpretation of the narratives on special and general relativity theory and the (Einstein 1905) Michelson–Morley experiment in chronological order (Michelson and Morley 1881, 1887). It can be stated that the term “relativity” is most often used after the Michelson–Morley experiment in physics. The Michelson–Morley experiment concluded that the speed of light appears to be the same in all directions. Lorentz interpreted the result using a mathematical model and proposed that the length of systems contract in the direction of motion and time also contracts similar to length contraction (Lorentz 1937).

This mathematical model is known as the “Lorentz transformations.” Although Lorentz solved the problem here mathematically, he did not explain the decrease in momentum with the internal motion of a moving system. Einstein solved this problem mathematically by proposing that the mass of the system increases with its motion (general relativity). Einstein proposed that objects in motion have more mass than when at rest. This gain in mass is known as “moving mass” (Lorentz 1937).

Here, we introduce a discussion platform with questions about these propositions of Lorentz and Einstein, and then through these discussions, we define the relativity model using a different mathematical model (Dervisoglu 2019).

The principle of relativity, which forms the basis of the special relativity model, and the invariance of the speed of light forms the basis of our

proposed relativity model (Einstein 1923; Einstein *et al.* 2014). However, based on these assumptions, results obtained from the principle of relativity will be different. In the proposed relativity model, we propose that the mass (m), length (x, y, z), internal velocity (v), momentum (p), and energy (E) of the moving systems will decrease at an equal rate. That is, when an object or a system (atom) is in motion, it will have reduced mass, length, and internal velocity than those at rest.

Herein, we will examine a case where we will suggest an unchanging time irrespective of the system’s acceleration and a changing time on exposure to acceleration or gravity (Dervisoglu 2019).

THE THEORY OF RELATIVITY THAT BEGAN WITH THE MICHELSON–MORLEY EXPERIMENT

Michelson–Morley Experiment and Special Relativity Model

This section examines the special and general relativity model, which started with the Michelson–Morley experiment, in chronological order, through our interpretation of classical thought experiments. Since the Michelson–Morley experiment is a familiar topic, we will examine it here without going into in detail.

Michelson–Morley Experiment: Michelson and Morley conducted an experiment to prove the existence of ether experimentally. However, they did not observe the expected shift even after conducting several experiments over one year (1880–1881). Although this experiment concluded that ether does not exist, these two scientists still believed in the existence of ether (Gautreau and W 1999).

This experiment concluded that the speed of light is the same in all directions. However, this observation did not agree with Maxwell’s

Manuscript received: 13 May 2021,

Revised: 13 September 2021,

Accepted: 5 October 2021.

¹derviszeki53@hotmail.com (Corresponding Author)

equations (Maxwell 1873). In Maxwell's equations, when Galileo transformations (Lorentz 1937; Relativity 2021b) are used for moving from one inertial system to another, the speed of light changes (1):

$$x' = x - vt, \quad y' = y, \quad z' = z, \quad t' = t \quad (1)$$

Since Michelson and Morley did not doubt the Earth's rotation around the Sun, the problem here seemed to lie in the Galileo transformations (Gautreau and W 1999). Meanwhile, in 1887, Lorentz thought that the result of the Michelson–Morley experiment did not prove the ether's absence but substantiate its existence. To verify it, he made a proposition that this invariance in the speed of light causes the length of the system to contract in the direction of motion and that there is time dilation and length contraction (Lorentz 1937; Michelson and Morley 1881).

Lorentz addressed the problem of time dilation mathematically similarly to the length contraction (Fig. 1) and proposed that the obtained mathematical expression is compatible with Maxwell's equations, i.e., (Maxwell 1873) the speed of light does not change in inertial moving systems. According to this mathematical model, the schematic of the Michelson–Morley experiment is shown in Fig. 1 (Gautreau and W 1999; Einstein 1935).

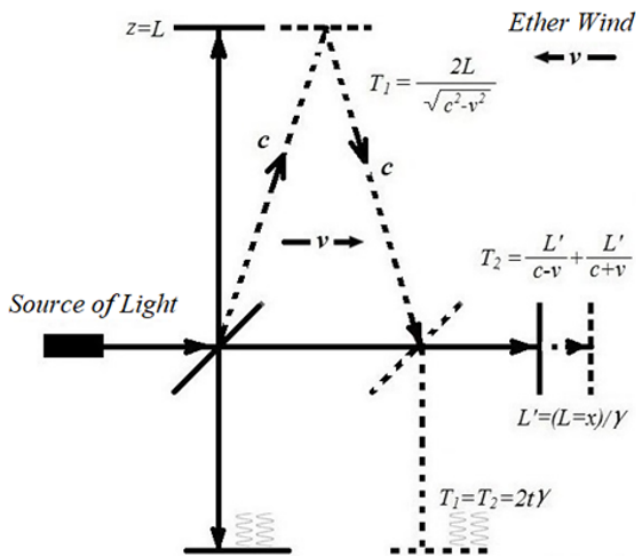


Figure 1 Schematic of the Michelson–Morley experiment. Visual and mathematical description of the speed of light appears the same in all directions based on Lorentz's proposition.

Transformation equations from a stationary system K to another moving system K' (Fig. 2): Basically, the transformation equations from equations (2) to (5) are “Lorentz transformations” (Lorentz 1937, 1895).

$$\gamma = \sqrt{1 - v^2/c^2} \quad (2)$$

$$x' = \gamma(x - vt), y' = y \quad (3)$$

$$t' = \gamma\left(t - \frac{vx}{c^2}\right) \quad (4)$$

Here, it will be seen that the measured speed of light does not change regardless of the unaccelerated speed of the system K (Lorentz 1937, 1895) (5).

$$x'^2 + y'^2 + z'^2 = c^2 t'^2 \quad (5)$$

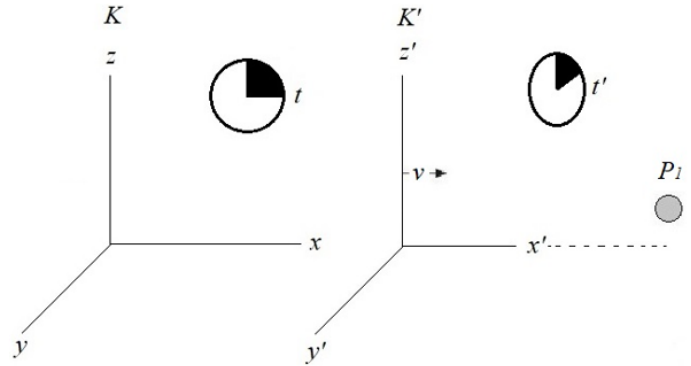


Figure 2 Inertial system K and noninertial system K' moving with velocity v in x' -direction.

However, Lorentz could not provide a physical explanation for the decreasing momentum, which is proportional to the length contraction in moving systems. Further expanding upon the Lorentz transformations, Einstein published a paper in 1905 regarding the “principle of relativity” and “the speed of light being invariant” under the theory of special relativity (Einstein 1935; Cahill 2004b).

In summary, special relativity states that the speed of light is constant. Therefore, the mass, length, energy, and time, which we think are constant in systems traveling at a constant speed, vary but transform into invariance within the invariance of the speed of light. In other words, the laws of physics are the same for all observers moving at constant speed, but their consequences in time will be different. Einstein knew, like Lorentz, that the most important problem facing special relativity was the changing momentum, which needs to be explained (Cahill 2004b,a).

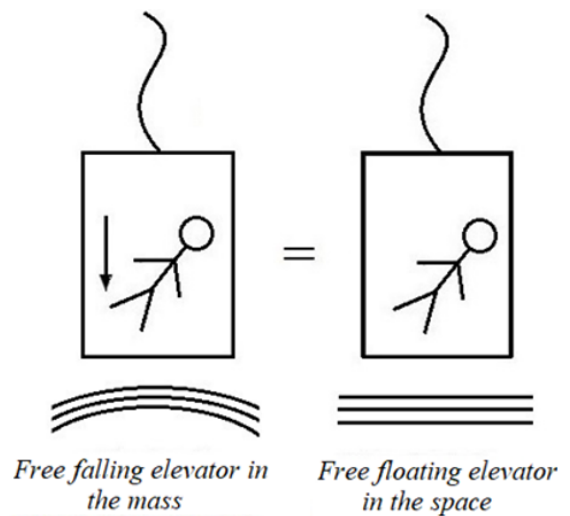


Figure 3 An observer in a free-falling elevator in a gravitational field (left) and a free-floating elevator in a space environment (right). Irrespective of the environment, the results are the same.

General Relativity Model

The “geometric model of gravity” or “general theory of relativity” describes the mass in modern physics in its most simple and plain definition. We are familiar with Einstein’s imaginary elevator experiment, which reflects the idea underlying the general theory of relativity.

If we look at Einstein’s conclusion from this experiment without going into detail, he showed that an observer in a free-falling elevator in a gravitational field or a free-floating elevator in a space environment would give the same result (Fig. 3).

In other words, experiments carried out by an observer in an elevator suspended in a gravitational field or an elevator moving with a constant acceleration in space will give the same result (Fig. 4) (Wheeler and Ohanian 1991; Norton 1985; Wald 2006).

However, with his experiments inside the elevator, the observer could differentiate due to his/her approach to the center of mass, even if it is very small. By analyzing this difference, the observer can differentiate between the gravitational field and the accelerating elevator. Nevertheless, this is not what the thought experiment wants to describe.

Einstein thought that there is a more general physical law that encompasses all these and proposed the equality of gravity and acceleration locally as the “equivalence principle” (Wheeler and Ohanian 1991; Norton 1985; Miller 1981). Based on this principle, he suggested that gravity does not exist, instead, objects bend the space in their sphere (Fig. 5) and the objects travel along the bent path giving the illusion of gravity.

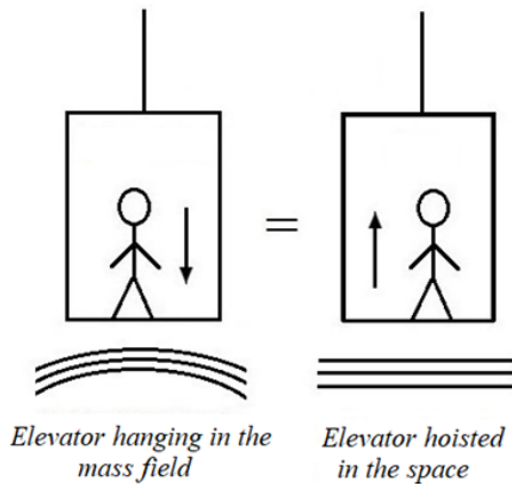


Figure 4 An observer in an elevator suspended in a gravitational field (left) and an elevator moving with a constant acceleration in space (right).

Einstein defined this bending of mass on ether, space, or fabric. Einstein suggested that this mass would increase due to the motion of the objects, i.e., the moving objects would have more mass. This mass, which increases due to motion, is known as the “moving mass” (Einstein 1917). Let us examine the mechanism underlying moving mass.

Moving Mass

Einstein relates the physical effect that causes the slowdown of velocity (momentum) of the moving systems to the increase in mass ($m\gamma$) because of the motion of the system. Thus, he suggested that when a system (body/particle) moves, it has more mass than rest. However, it does not mean that this increase in mass is accompanied by an increase in the amount of particles or the physical dimensions of the particle.

Let us try to understand this proposed increase in mass over a thought experiment. For instance, assume an accelerating system (a , as shown

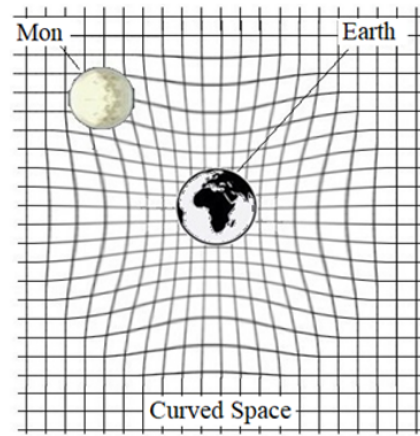


Figure 5 Mass bending space (curved space).

in Fig. 6) with zero friction around a shaft. When this system starts to move (a' , as shown in Fig. 6), it is suggested that the centripetal force of the moving weight in the system (deviation coefficient) will increase in proportion to the mass of the system ($m\gamma$). This increase will decrease the velocity to allow the moving weight to maintain its momentum in a straight-line.

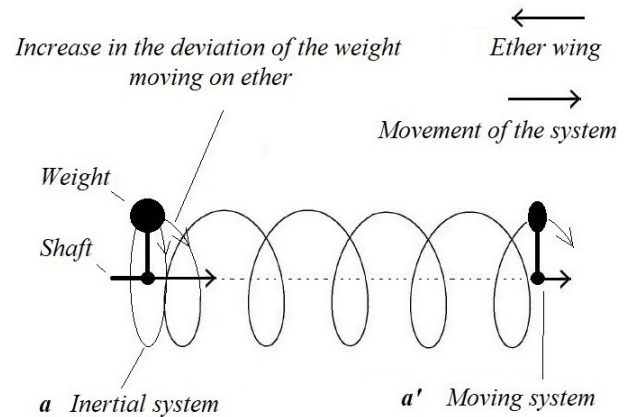


Figure 6 A visual illustration of the moving mass suggested by the general relativity.

General relativity suggests that not only will the mass of moving systems increase but that for the systems entering or leaving the gravitational field, the mass will change just like the moving mass above (Relativity 2021a).

DISCUSSIONS ON SPECIAL AND GENERAL RELATIVITY MODELS

Question 1: The relationship between the contraction of an object along the direction of motion and its volume and area: Why should the force exerted on an object change proportionally to the volume of the object and not its area? So, what is the changing area here? Is this change (force–volume) not in contradiction to the definition of quantum mechanics? Interestingly, when the v of the object approaches c , it changes from three dimensions to two dimensions (Fig. 9) (Dervisoglu 2019).

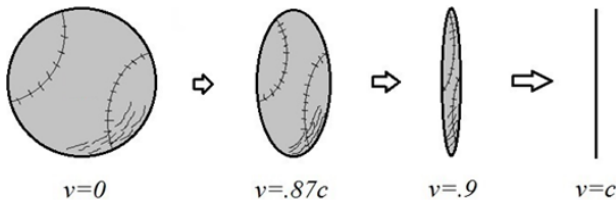


Figure 7 Tensile depiction of what goes with the movement of the ball, not the surface area due to its movement.

Question 2: What could be the physical effect that shrinks (shortens) the moving system (body) to only the direction of motion? Let us assume that we are teleporting an object into space. According to the definition of mass in general relativity, (Lorentz 1937) for the teleported object to create a mass in space, it has to bend the space fabric (Fig. 5) outward. Since the object cannot bend space (speed of gravitational effect) to be different from the speed of light propagating in the same direction, (6–7) the following questions come to mind:

$$F' = c' = \sqrt{1 - v^2/c^2} \quad (6)$$

Vertical to the direction of travel

$$F'' = c'' = 1 - v^2/c^2 \quad (7)$$

Parallel to the direction of travel

Why should the force acting on the object (namely the object's acceleration) cause the electrons moving around the nucleus to shrink only in the direction of movement? While the accuracy of the equations (6–7) we suggested above is very clear, what could be the physical effects that force the atoms of the object to contract only in the direction of motion?

Question 3: Even if there is a strong suggestion (Fig. 6) that the centripetal force of the (Wald 2006) weight $\gamma (F_{mk})$ will increase with an increase in the deviation or deflection coefficient of the moving weight in space arising from the movement of the system, why should the linear momentum; thus, the mass ($m\gamma$) of the system increases in proportion to such increase? With this expected mass increase, it is suggested that the density of the space (captive area) will increase by stacking the space (a in Fig. 10) that objects bend space in proportion to their mass in front of the object (a' in Fig. 10). This mass increase can only be realized from the “Wave” model. Then this proposed mass will not be the “geometric model of gravity”.

Question 4: Starting again from the proposition that the object will bend the space proportional to its mass in front of it, how is it possible that the speed of light traveling through the curved space in front of the object and the speed of light traveling in uncontracted space outside the object have the same speed in the same direction? Is the light having a velocity independent of its source relative to the space fabric, or space? Therefore, for the speed of light in the inner space of the object to be at the same speed as that in the outer space in the same direction, should not the texture in the outer space of the object and the texture in the inner space of the object preserve the same property (Dervisoglu 2019)?

Question 5: At the zero point of the length of an object accelerating to the speed of light, the general relativity model

$$0 = x\sqrt{1 - (c^2/c^2)} \quad (8)$$

-suggests that the mass of the object

$$\infty = m \frac{1}{\sqrt{1 - (c^2/c^2)}} \quad (9)$$

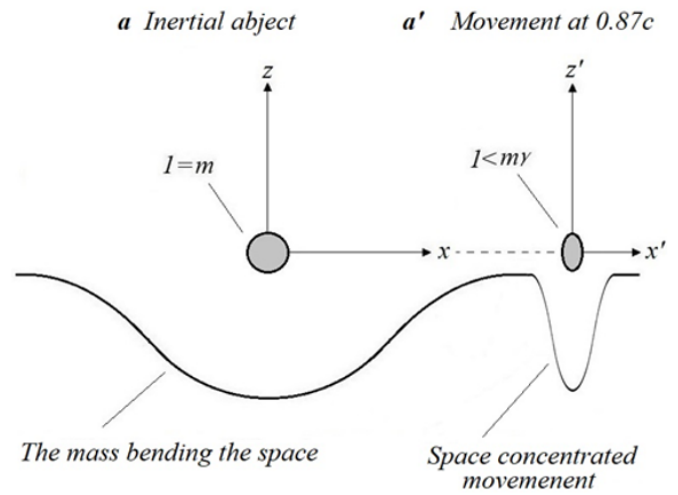


Figure 8 Representative drawing shows the increase in mass of the object proportional to the contraction of space in the object's direction of motion.

will also be infinite. Thus, how can the mass of an object whose length is at the zero point (8), i.e., an object that disappears physically, be infinite (Equation (9))? Although I do not agree with the proposition that the mass will increase due to motion, it is clear that the problem here is not in the Lorentz's length contraction in the direction of the motion of the system or the Einstein's mass increase explanation, (Einstein 1916) but in the laws of physics (Dervisoglu 2019) itself. We will examine this proposition below.

Question 6: Does the gravitational force between objects change due to motion? For example, we can define the gravitational force between the Sun and a system passing close to the Sun having a low velocity (v) as $F = (Mm)/R^2$ (Newton 1686) (A in Fig. 9). If the system had passed near the Sun in the same way as the speed of light ($0.87c$) (A' in Fig. 9), it would be very wrong to suggest that the gravitational pull applied by the system would decrease (A' in Fig. 9) since **the displacement speed** of the bending (mass) would not exceed the communication speed of the light moving in the system, while the system was carrying the curved space, i.e., its mass (Fig. 9-A and formula 6 and 7).

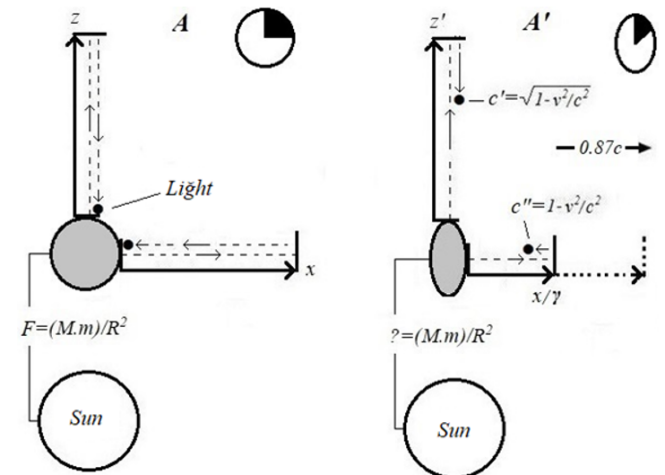


Figure 9 Representative thought experiment showing the relationship between force and motion.

A DIFFERENT INTERPRETATION OF THE MICHELSON-MORLEY EXPERIMENT

Above in Section 2 we first examined the special and general relativity model in summary with well-known classical definitions, and then in Section 3 we drew attention to the controversial issues by asking questions to the special and general relativity model. Section 4 describes a new theory of relativity by proposing a different mathematical model to the Michelson–Morley experiment result.

The Ultimate Unreachable Velocity of The Universe “ $c + v_g$ ”

According to the general relativity model, how does an object traveling at the speed of light have an infinite mass (Equation (9)) when its length is at the zero (Equation (8)) point. In fact, it is clear that this anomaly can neither be found in Lorentz’s length contraction nor in Einstein’s mass increase, but in the laws of physics.

Einstein’s view that the ultimate speed of the universe is the speed of light and that objects and particles cannot move at speeds higher than this speed, and that the speed of light is a law is a very valid opinion. The problem here is that the universe has no ultimate **unattainable** speed.

Ultimate Unattainable Velocity of the Universe: We strongly suggest that the entire constituting space is covered with ether (captive space). In addition, we suggest that this ether will collapse on its surface with a velocity proportional to the masses of the objects and that this collapse (mass) will be inversely proportional to the velocity of the object. Thus, here it becomes “mass is a different form of motion”. *Of course, the mechanism in the mass definition we propose is a subject of separate discussion.*

For example, when we stand still on its surface, we are **physically** traveling on the surface at a speed (Equation (10)) proportional to the mass of the Earth. For example, at this moment, ether wind blows over me at speed proportional to the mass of the Earth, and its direction is toward the center of the Earth. In addition, we do not mind saying ether wind here, this velocity is at a very low rate, as seen in the Equation (10) below:

$$v_g = \frac{2g}{c^2} = 0.000000000000002 \text{ m/s} \quad (10)$$

Here, g is the acceleration due to gravity (9.8 m/s), and v_g is the rate of collapse of the ether to the surface proportional to the mass of the Earth.

If this speed of ether was to be measured, the ether would sink or travel to the Earth’s surface at only 6 m in approximately 100 million years. Therefore, it would not be wrong to say that the mass of the moving celestial bodies only changes the resistance of this space (ether). This suggested speed (Equation (10)) will be different for objects larger or smaller than Earth.

Therefore, our reference mass in this suggested ether wind speed is not the Earth, but the mass of the place (body) where the event takes place. This speed is given by the following equation (Dervisoglu 2019):

$$v_g = \frac{2Gm}{c^2} \quad (11)$$

Here, v_g is the rate of collapse of the ether to the surface proportional to the mass of the object, G is the gravitational constant, c is the final velocity of the universe, and m is the mass of the object.

This velocity (v_g) we suggested above becomes a **physical** velocity originating from the mass. The sum of v_g and the speed of light (c), given in Equation (12), gives us the final speed of the ether:

$$c + v_g \quad (12)$$

We define it as “the ultimate unattainable speed of the universe”. **Visually**, nothing can reach this speed that we have defined. Thus, with

the speed that we have proposed, we are proposing a new physical law in the definition of events.

Basic Assumptions of Our Suggested Relativity Model

The “*principle of relativity*” and “*invariance of the speed of light*,” which form the basis of the general relativity model, also form the basis of our proposed theory of relativity. However, from these assumptions, the definition and the results of the principle of relativity would be different. The basic assumptions of the theory of relativity, which is our proposition, are as follows:

The Principle of Relativity Einstein proposes that the laws of physics will be the same for all observation frames that move steadily without acceleration and which do not rotate around their own axis, but the results will be different (Relativity 2021b).

The difference between Einstein’s proposition and our proposed principle of relativity is that the proposed relativity model tells us that **no matter what the unaccelerated steady motion of a system is**, the laws of physics and **temporal** results will be the same in all observation frames, i.e., the time of the system **will not change**. However, it suggests that the time of systems subjected to **acceleration** or **gravitation will change** (Dervisoglu 2019).

Invariance of The Speed of Light Einstein proposes that the speed of light will be the same for every observer, regardless of the non-accelerated motions of the observers. This principle also holds in our proposed theory of relativity.

The Proposed Relativity Model

Let us define the proposed relativity model on a system: For example, the light thrown from a stationary system in the (x, y, z) directions at “ $t = 0$ ” time will spread in the following way (Fig. 12).

$$0 = r - ct_{\delta z}, \quad (13)$$

$$0 = x^2 + y^2 + z^2 - c^2 t_{\delta z}^2. \quad (14)$$

In addition, we know that when we do this experiment again, it will give the same result. It is strongly suggested here that the particles move (float) within the ether.

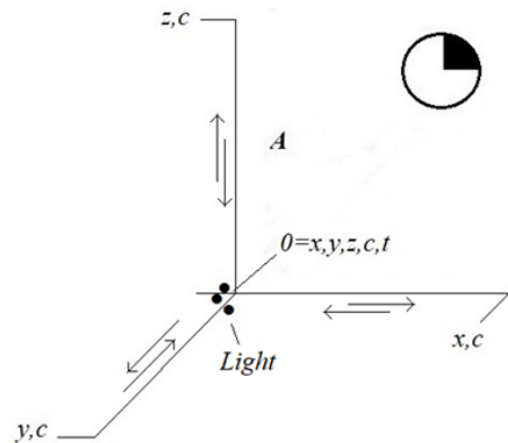


Figure 10 Inert system.

We are suggesting that when this system moves in the “x” direction with half the speed of light (0.5c), the mass of the system (m), the lengths (x, y, z) and the communication speed of light at those lengths (c) or the speed of the rotating clock wheel will decrease equally (Fig. 13). That is, when the system moves, it has less mass, length, and internal movement velocity than at rest:

$$x' = m' = c' = 1 - v^2 / (c + v_g)^2 \quad (15)$$

$$y' = m' = c' = \sqrt{1 - v^2 / (c + v_g)^2} \quad (16)$$

$$z' = m' = c' = \sqrt{1 - v^2 / (c + v_g)^2} \quad (17)$$

Although the internal movement speed of the system (c or the speed of the clock wheel and the speed of the clock) decreases here, the system is moving with the internal rotational speed. The time of the system preserves itself toward invariance within an equal change in lengths, i.e., it does not change:

$$0 = x' - c' = y' - c' = z' - c' \quad (18)$$

$$1 = t'_{0z} = \frac{x'}{c'} = \frac{y'}{c'} = \frac{z'}{c'} \quad (19)$$

Therefore, regardless of the unaccelerated speed of the system, its time (amount of movement) does not change. When we look at the propagation of light with the changes, estimated from equations (15, 16, 18, and 19), we propose in mobile systems; it will spread following the Equation (20):

$$0 = x'^2 + y'^2 + z'^2 - c'^2 t'^2_{0z} \quad (20)$$

For Equation (20) to be a result of Equation (14), Equation (21) must be satisfied:

$$x^2 + y^2 + z^2 - c^2 t^2_{0z} = x'^2 + y'^2 + z'^2 - c'^2 t'^2_{0z} \quad (21)$$

If we look at the force balance in the ratio of mass to length within these changes, we propose in the system: gravity also preserves itself toward invariance within the equal variation of the lengths (x', y', z'):

$$1 = F = \frac{m'^2}{x'^2} = \frac{m'^2}{y'^2} = \frac{m'^2}{z'^2} \quad (22)$$

In the mathematical model suggested above, we can naturally fall into the perception that the movement (time) in the system traveling at the speed of light will stop. However, as per the conversion equations we suggested above (15–16-17), there is movement everywhere that there is a mass, and time flow everywhere there is a movement, since the mass of the system traveling at the speed of light is not at the zero point.

For example, when the speed “v” of the system in Fig. 13 is “c,” the observer measures “v_g” speed of light as the “c” speed. In other words, even if the system is close to the zero point, it carries all the physical values that will show that it is there. These transformation or change equations (15–16-17) that we propose in moving systems become the mathematical theory of relativity.

Note: The effect that causes this change in mobile systems is the resistance of the object to the change in velocity (Dervisoglu 2019). However, the content of this resistance is not the subject of this article.

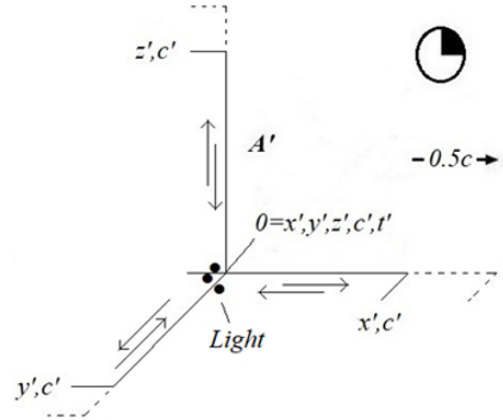


Figure 11 When the system travels at 0.5c speed of light.

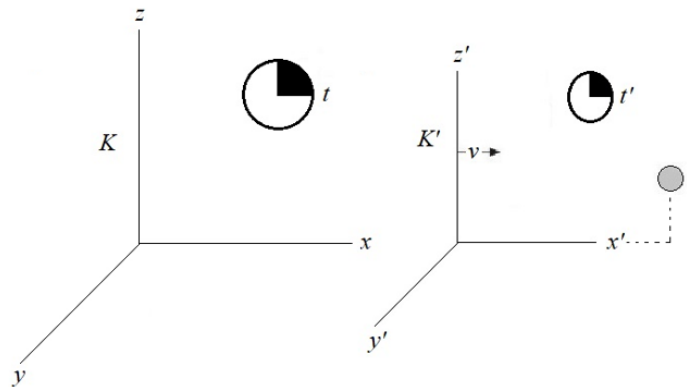


Figure 12 When switching from one inert system to another mobile system.

Conversion Formulas

When moving from an inert K system to another mobile K' system, we propose transition formulas in which time (1=substance) does not change within the invariance of the laws of physics, instead of the Lorentz transformation formulas (2-3-4-5-6) (23-24-25).

$$x' = \frac{x - vt}{1 - v^2/(c + v_g)^2} \quad (23)$$

$$y' = z' = \frac{y = z}{\sqrt{1 - v^2/(c + v_g)^2}} \quad (24)$$

$$t' = t - \frac{vx}{c^2} \quad (25)$$

The transformation formulas we suggested above can be valid for measuring the distance of K from the point P when moving from the stationary system K to the mobile system K. The stationary system is not valid for the speed of light traveling from K to P (Dervisoglu 2019).

Mathematical Description of the Michelson–Morley Experiment

In the framework of the proposed mathematical model, the Michelson–Morley experiment visual and mathematical test results are presented in Fig. 13. It can be seen that the proposed mathematical model is compatible with Maxwell's equations (Maxwell 1873) (the speed of light appears to be the same in all directions in unaccelerated motion systems).

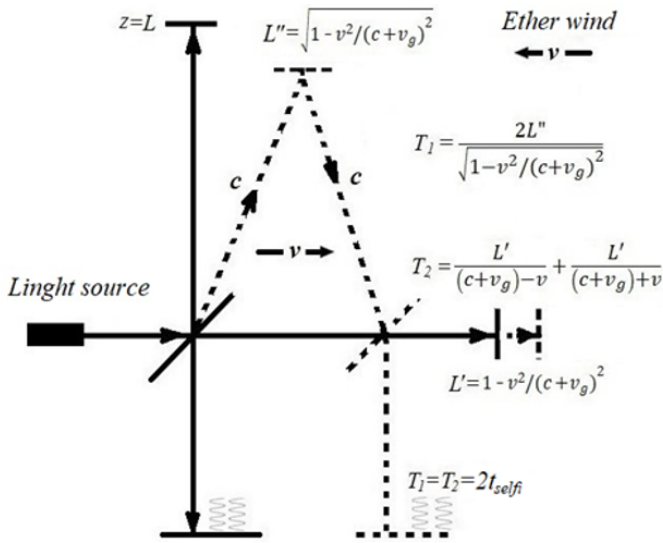


Figure 13 The equation we propose in the Michelson-Morley experiment.

Fixed Multiplier (\mathcal{D})

We define the closed (non-directional) form of the proposed mathematical model on moving systems as the constant multiplier (\mathcal{D}):

$$\mathcal{D} = \frac{(1 - \frac{v^2}{(c+v_g)^2}) + (\sqrt{1 - \frac{v^2}{(c+v_g)^2}}) + (\sqrt{1 - \frac{v^2}{(c+v_g)^2}})}{3} \quad (26)$$

$L' = \mathcal{D}L$: (x, y, z) lengths of the system,

$m' = \mathcal{D}m$: Mass of the system,

$c' = \mathcal{D}c$: Speed of the inner system communicating at a speed of light,

$v' = \mathcal{D}v$: Internal speed of the system,

$E' = \mathcal{D}E$: Internal energy of the system.

For Equation (26) to be a result of Equation (20), Equation (27) must be true.

$$x'^2 + y'^2 + z'^2 - c'^2 t_{\delta z}^2 = \mathcal{D}L^2 - \mathcal{D}c^2 t_{\delta z}^2 \quad (27)$$

Notice that there is no time (t) in the transformations suggested in Equation (27). The lack of time, as we said above, is that the time of the system ($1 = t_{core}$) will not change (universal) regardless of the unaccelerated speed of the system. However, we are suggesting a **changing** time in systems entering or existing in a gravitation field or in systems **accelerating** in the framework of equality of gravity and acceleration. Nevertheless, the definition of this universal and relative time that we propose is not the subject of this article (Dervisoglu 2019).

CONCLUSIONS AND RECOMMENDATIONS

In this study, we proposed a **relativity model**. The proposed mathematical model is a summary of the theory of relativity in our book “The Great Formation” universe model. We can briefly explain our book as following: Although “the Great Formation” is a different universe model, we are proposing a new gravity model under the name “general model of gravity.” The gravity that we propose is described in the quantum-scale mechanism within the standard model. The “general model of gravity” also introduces a different theory of relativity that we have summarized above.

Here we propose the ultimate unattainable speed “ $c + v_g$ ” of the universe, which we suggested in the description of events above, as a new physical law. Although this speed ($v_g = 2.10^{-16} = 0.000000000000002m/s$), which we suggest as a plus (+) to the speed of light, seems like a very small speed, we can describe all events in the universe with this velocity. Thus, with this ($c + v_g$) speed, we propose a different dimension and a different meaning to the definition of events. Some of these are as follows:

- The further away we observe in space, the more we observe the spectrum of light shifting toward red. This observed redshift is a measure of the amount of matter in that observed radius.
- The farther away the electron (photon) reaches from us, the more it is absorbed, i.e., it loses energy (momentum).
- The universe keeps its entropy in balance by cooling the radiated energy. That is, the entropy of the universe does not change.
- In the inverse proportion that we propose between mass and motion, mass becomes a different form of motion.
- Regardless of the steady motion of a system without **acceleration**, its time will preserve itself toward invariance within the invariance of the laws of physics, i.e., it **will not change**.
- The time of systems entering or exiting a gravitational field or systems accelerating within the framework of the gravitational acceleration equation **will change**.
- In the framework of the final velocity “ $c + v_g$ ” (law) of the universe that we proposed, the result of an event “ x ” may be “ $0 < x$ ” close to zero or “ $\infty > x$ ” close to infinity, but it cannot be zero “ $0 = x$ ” or infinity “ $\infty = x$ ”.
- The mass (m) of the moving systems, the (x, y, z) lengths and the communication speed of light (c) will decrease equally and when the speed “ v ” of the object is “ c ,” this decrease will be close to the zero point, but it will not be at the zero point. The fact that it is not at the zero point is a result of the final velocity “ $c + v_g$ ” (law) of the universe we proposed.

We have many propositions that we cannot list here yet. In addition, the content of our propositions here has much broader explanations and equations but it is the subject of our book “The Great Formation” universe model, the 3rd edition of which has not been published yet.

Conflicts of interest

The author declares that there is no conflict of interest regarding the publication of this paper.

Availability of data and material

Not applicable.

LITERATURE CITED

- Cahill, R. T., 2004a Absolute motion and gravitational effects. *Apeiron* **11**: 53–111.
- Cahill, R. T., 2004b Quantum foam, gravity and gravitational waves. *Relativity, Gravitation, Cosmology* pp. 168–226.
- Dervisoglu, Z. C., 2019 *Great formation universe model*. Gece Kitap, second edition, (3rd Edition Has Not Been Yet published).
- Einstein, A., 1905 Zur elektrodynamik bewegter körper. *Annalen Der Physik* **4**.
- Einstein, A., 1916 *Relativity: The Special and the General Theory*. Berlin.
- Einstein, A., 1917 *Über die spezielle und die allgemeine relativitäts theorie*, volume 6. Braunschweig: F. Vieweg and Sohn, 15th edition.
- Einstein, A., 1923 *Relativity: the special and the general theory*. Princeton University Press.
- Einstein, A., 1935 Elementary derivation of the equivalence of mass and energy. *Bulletin of the American mathematical society* **41**: 223–230.
- Einstein, A., E. P. Adams, E. G. Straus, and S. Bargmann, 2014 *The meaning of relativity*. Princeton University Press.
- Gautreau, R. and S. W., 1999 *Modern physics*. McGraw Hill, second edition.
- Lorentz, H. A., 1895 *Versuch einer theorie der electrischen und optischen erscheinungen in bewegten körpern*. Leiden: E. J. Brill.
- Lorentz, H. A., 1937 Electromagnetic phenomena in a system moving with any velocity smaller than that of light. In *Collected Papers*, pp. 172–197, Springer.
- Maxwell, J. C., 1873 *A treatise on electricity and magnetism*, volume 1. Clarendon press.
- Michelson, A. A. and E. W. Morley, 1881 Art. xxi.–the relative motion of the earth and the luminiferous ether. *American Journal of Science (1880-1910)* **22**: 120.
- Michelson, A. A. and E. W. Morley, 1887 On the relative motion of the earth and of the luminiferous ether. *Sidereal Messenger* **6**: 306–310.
- Miller, A., 1981 *Albert einstein's special theory of relativity*. Reading, MA: Addison Wesley.
- Newton, I., 1686 *Philosophiae Naturalis Principia Mathematica (Principia)*.
- Norton, J., 1985 What was einstein's principle of equivalence? *Studies in history and philosophy of science Part A* **16**: 203–246.
- Relativity, G., 2021a https://sites.pitt.edu/~jdnorton/teaching/HPS_0410/chapters/general_relativity/index.html. (Accessed on 10/21/2021).
- Relativity, T. S. T. O., 2021b <https://www.britannica.com/topic/philosophy-of-physics/The-special-theory-of-relativity>. (Accessed on 10/21/2021).
- Wald, R. M., 2006 Resource letter tmgr-1: teaching the mathematics of general relativity. *American Journal of Physics* **74**: 471–477.
- Wheeler, J. A. W. and H. C. Ohanian, 1991 A journey into gravity and spacetime. *American Journal of Physics* **59**.

How to cite this article: Caliskan, Z. Discussions on the Special and General Theory of Relativity. *Chaos Theory and Applications*, 3(2), 87-94, 2021.